

# MECHANOREGULATION OF CYTOTOXIC T LYMPHOCYTE KILLING

A Dissertation

Presented to the Faculty of the Weill Cornell  
Graduate School of Medical Sciences  
in Partial Fulfillment of the Requirements for the Degree of  
Doctor of Philosophy

by

Mitchell S. Wang

May 2022

© 2022 Mitchell S. Wang

ALL RIGHTS RESERVED

# MECHANOREGULATION OF CYTOTOXIC T LYMPHOCYTE KILLING

Mitchell S. Wang, Ph.D.

Cornell University 2022

Immune cell-cell communication is canonically presented as an interlinked network of biochemical pathways through which immune cells process information. However, this characterization fails to consider the physical methods that immune cells employ in order to interact with their local environment and enhance their cellular function. The conversion of mechanical stimuli into biochemical responses is called mechanotransduction. Cytotoxic T lymphocytes (CTLs) are an ideal system for studying these techniques because they are both physically active and immunologically communicative. Additionally, they are biomedically important, playing crucial roles in homeostatic and therapeutically induced immune responses against both foreign pathogens and cancer, thus making them therapeutically urgent and interesting to study.

CTLs exert physical force against target cells, thereby straining target cell membrane and mechano-potentiating the pore-forming activity of perforin and overall effector response. However, it remained unclear what structures T cells formed in order to exert physical force, and what proteins or signaling molecules could be involved in this phenomenon. We found that T cells utilized actin-rich protrusions at the cell-cell interface against the target cell to distort the target cell membrane. The formation of protrusions were dependent on the actin nucleation promoting factor Wiskott-Aldrich Syndrome protein (WASP), and were necessary for physical distortions in the target cell membrane that amplified T cell cytotoxicity. These results mechanistically clarified how T cells

exert physical force against their targets to amplify the pore-forming effects of perforin oligomerization in the target cell surface. However, it remained to be seen how T cells could coordinate these two arms of cytotoxic signaling for optimized cytotoxicity.

Given that higher levels of T cell mechanical force exertion were correlated with higher levels of killing, we were curious to know if T cells used mechanical cues at the synapse to determine where to secrete their lytic granules into the intracellular space, thereby optimizing the release of the cytotoxic payload. Such a phenomenon could also reconcile how T cells avoid killing healthy bystander cells in a crowded cellular environment, by requiring physical engagement from antigen-presenting cells as a signal of cellular adjacency and safety. We found that T cells specifically degranulated near the engaged integrin receptor LFA-1 (lymphocyte function-associated antigen 1) that formed upon the detection of antigen. Fascinatingly, this relationship was dependent on the mechano-transductive behavior of LFA-1, as ablation of its force-generating capacity via talin inhibited LFA-1 force exertion and degranulation completely. The ability to convert mechanical stimuli into a degranulation signal was also broadly generalizable to other integrins. These results, in their totality, identify how T cells are able to secrete lytic granules near areas of force exertion, and clarify how T cells are able to clear diseased cells with minimal bystander killing.

Our studies describe the sophisticated mechanisms used by the T cell to mechanically optimize its cytotoxicity. We identified WASP-driven actin-rich protrusions as a major driver of force exertion against the target cell membrane to prime it for perforin insertion and pore formation. Additionally, we identified a new mechanical role for the integrin LFA-1 (and broadly, all other integrins) in establishing sites of cell-cell proximity and therefore permissive lytic granule

release in order to safely and efficiently deposit the cytotoxic payload against the target cell. Altogether, these studies further clarify the mechanical pathways that CTLs utilize to engage with and interpret their immune environment, ultimately resulting in efficient clearance of infected and tumor cells.

## BIOGRAPHICAL SKETCH

Mitchell was born in 1993 in Palo Alto, California and came of age in the suburbs of Philadelphia, Pennsylvania. After his high school education, he attended New York University, where he studied for his Bachelor of Arts degree as a double major in both biology and economics. During his time at NYU, he studied Alzheimer's disease in the laboratory of Dr. Yueming Li at Memorial Sloan Kettering Cancer Center. Upon graduating in 2015 and with an interest in the biomedical sciences, he entered the Pharmacology program at Weill Cornell Graduate School of Medical Sciences and joined the laboratory of Dr. Morgan Huse at Memorial Sloan Kettering Cancer Center for his thesis work, where he has since studied the principles of mechanical force exertion in T cells and their contribution to cellular cytotoxicity.

Mitchell's best memories away from the lab during graduate school were spent in the warmth of Jacob Riis beach, in the colorful company of his friends he met in New York City, and behind the lens of his digital and film cameras.

*for Mama, Baba, and Nick*

## ACKNOWLEDGEMENTS

Graduate school simply cannot be done alone, and far be it from me to write this many words without mentioning the people who have helped make this dream come true. I must first thank my thesis advisor Dr. Morgan Huse for inviting an untrained, greenhorn scientist into his lab to work on visually and viscerally exciting science, where together we asked and answered groundbreaking questions about T cell biology and killing with creative and nearly artistic experiments. I must thank him for mentoring me throughout this doctoral process; training, developing, and eventually welcoming me to join the community of scientists. Thank you Morgan.

I would also like to thank my thesis committee members Drs. John Blenis, Morgan Huse, Philipp Niethammer, David Scheinberg, and Andrea Schietinger, for their scientific direction and suggestions - for a young scientist, the time of an experienced scientist is worth its weight in gold.

Thank you to the collaborating labs and brilliant scientists who have made this scientific work possible and without whom these ideas would simply remain ideas. Thank you to the Dr. Lance Kam laboratory at Columbia University, in particular: Dr. Susie Jin, Dr. Parthiv Chaudhuri, Dr. Joanne Lee, Dr. Chirag Sachar, and Xin Wang, who have helped open this world of T cell mechanobiology to me. The Dr. Khalid Salaita lab at Emory University as well, particularly Yuesong Hu, who made our manuscript way more exciting and awed our audiences. Thank you!

Of course, my dear labmates, past and present. This work is as much yours as it is mine - we did it! Thank you to Ben Whitlock, who showed many of us that graduate school was usually only as stressful of an experience as you let it be. To Fella, for allowing the younger me assist you on your protrusions paper. To

Minggang, for always being around in the lab at 2 A.M. to show the bleary-eyed me where the bacteria spreaders are. To Diana, for reinforcing my belief that scientists can dress well and look stylish every day! To Alex, for your reassuring and free-flowing attitude to whatever today's strange topic of conversation is. To Maria, for your boundless ebullience and colorful patterned dresses. To Ben Winer, for your unflappable attitude towards science, humor, and your career - best of luck! To Lizzy, for your lively cheerfulness and always complimenting my appearance each day. To Ty, and his postdoc expertise (lol) - I hope you enjoy living in New Jersey so much. To Miguel, for all of your advice over the years: philosophical, scientific, musical, and personal. And of course to my lab sibling Elisa, who knows that my gratitude for her cannot be fully expressed in words.

My friends in graduate school - thank you for sharing the wealth that is your lives with me. My cup runneth over! Living in New York City is magical, but only because the people make it so. Thank you to Mark, in helping me grow in every way, possible and impossible. Thank you to Thomas, Rosa, Alan, Bobby, and George for the countless hot pot nights and for providing safe haven during the most uncertain periods of the Pandemic. Special shoutout to Bobby for showing me the beauty of LaTeX and serving as a private IT service. Thank you to Louise, Kathleen, and Mariano - my memories of our times together (and to come) are lost somewhere in a blur of fantastic wine and cheese and the Reopening.

Last but not least, I must thank my family: my mom and my dad and my younger brother Nick and my extended family members around the globe in Germany and China, for always picking me up whenever I might fall. Happiness does not always come easy, but the support of my family always has, and I know always will!

## TABLE OF CONTENTS

Biographical Sketch . . . . .	iii
Dedication . . . . .	iv
Acknowledgements . . . . .	v
Table of Contents . . . . .	vii
List of Tables . . . . .	x
List of Figures . . . . .	xi
List of Abbreviations . . . . .	xiii
<b>1 INTRODUCTION AND BACKGROUND</b>	<b>2</b>
1.1 The immune system and T cells . . . . .	2
1.2 T cell development . . . . .	4
1.3 TCR activation and downstream signaling . . . . .	7
1.4 The immunological synapse and the T cell cytoskeleton . . . . .	9
1.5 T cell degranulation and target cell death . . . . .	11
1.6 T cell mechanical force exertion . . . . .	14
1.7 Thesis Aims . . . . .	18
<b>2 INTERFACIAL ACTIN PROTRUSIONS MECHANICALLY ENHANCE KILLING BY CYTOTOXIC T CELLS</b>	<b>20</b>
2.1 Background . . . . .	20
2.1.1 Force exertion through the actin cytoskeleton . . . . .	22
2.1.2 Modifying target cell sensitivity to perforin . . . . .	22
2.2 Results . . . . .	23
2.2.1 CTLs form actin-rich protrusions on stimulatory micropillars	23
2.2.2 Granule fusion occurs at the base of synaptic protrusions .	28
2.2.3 WASP and WAVE2 control distinct subsets of protrusions	32
2.2.4 WASP and WAVE2 depletion induce distinct functional phenotypes . . . . .	34
2.2.5 WASP controls target cell deformation at the IS . . . . .	39
2.3 Discussion . . . . .	44
2.4 Materials and Methods . . . . .	48
2.4.1 Study design . . . . .	48
2.4.2 Micropillar preparation . . . . .	49
2.4.3 Live imaging on micropillars . . . . .	50
2.4.4 Lattice light-sheet imaging . . . . .	50
2.4.5 Image analysis . . . . .	51
2.4.6 Killing assay, granule fusion assays, and conjugate formation	52
2.4.7 Statistical analysis . . . . .	53
2.4.8 Constructs . . . . .	54
2.4.9 Cells and small molecule inhibitors . . . . .	55
2.4.10 Retroviral transduction . . . . .	55
2.4.11 Fixed imaging . . . . .	56

2.4.12	<i>Ca<sup>2+</sup></i> imaging . . . . .	56
2.4.13	Adhesion assay . . . . .	56
2.4.14	Immunoblot . . . . .	57
<b>3</b>	<b>MECHANICALLY ACTIVE INTEGRINS DIRECT CYTOTOXIC SECRETION AT THE IMMUNE SYNAPSE</b>	<b>58</b>
3.1	Background . . . . .	58
3.1.1	Canonical centrosome-based model of degranulation . . . . .	59
3.1.2	Force-directed localization of synaptic granule fusion . . . . .	60
3.1.3	Actin cytoskeletal direction of synaptic integrin localization . . . . .	60
3.1.4	Integrin biology and mechanotransduction . . . . .	60
3.2	Results . . . . .	62
3.2.1	LFA-1 is required for synaptic force exertion, degranulation, and cytotoxicity . . . . .	62
3.2.2	Degranulation occurs in IS domains containing ligand-bound TCR and ligand-bound LFA-1 . . . . .	67
3.2.3	LFA-1 pulling forces define degranulation domains . . . . .	76
3.2.4	Talin is required for LFA-1 mediated force exertion, degranulation, and cytotoxicity . . . . .	78
3.2.5	Talin, but not LFA-1, is required for CTL-mediated killing of B16F10 cells . . . . .	81
3.3	Discussion . . . . .	84
3.4	Materials and Methods . . . . .	88
3.4.1	Constructs . . . . .	88
3.4.2	Proteins . . . . .	88
3.4.3	Cells . . . . .	89
3.4.4	Traction force microscopy . . . . .	89
3.4.5	Antibody blockade and pharmacolog. activation/inhibition . . . . .	90
3.4.6	Retroviral transduction . . . . .	90
3.4.7	Functional assays . . . . .	91
3.4.8	CTL activation with stimulatory beads . . . . .	92
3.4.9	Micropatterning experiments . . . . .	92
3.4.10	<i>Ca<sup>2+</sup></i> imaging . . . . .	94
3.4.11	DNA hairpins . . . . .	94
3.4.12	MTP surface preparation and imaging . . . . .	95
3.4.13	Imaging analysis . . . . .	96
3.4.14	Proliferation Assay . . . . .	97
3.4.15	Immunoblot . . . . .	98
<b>4</b>	<b>DISCUSSION</b>	<b>99</b>
4.1	On the interfacing of mechanical and biochemical signaling planes . . . . .	100
4.2	On CTL force dynamics . . . . .	100
4.3	On the mechanical licensing of cellular activities . . . . .	102
4.4	On mechanical signaling of T cell subsets and engineered T cells . . . . .	103

4.5 On the limitations of <i>in vitro</i> -based investigations . . . . .	103
<b>Bibliography</b>	<b>104</b>

## **LIST OF TABLES**

## LIST OF FIGURES

1.1	Cell types of the innate vs. the adaptive immune system . . . . .	3
1.2	Positive and negative selection . . . . .	6
1.3	The T cell receptor and its signaling partners . . . . .	8
1.4	The immunological synapse . . . . .	10
1.5	Lytic granule secretion and perforin pore formation . . . . .	13
1.6	Canonical model of actin clearance as a necessary condition for lytic granule secretion . . . . .	14
1.7	T cells exert mechanical force against target cells . . . . .	15
1.8	Mechanosensitive receptors of the immune synapse . . . . .	17
2.1	Using PDMS micropillars as 3D environment to observe and measure CTL cytoskeletal structures. . . . .	23
2.2	Characterizing the architecture of protrusions using micropillars.	25
2.3	F-actin accumulates at the leading edges of synaptic protrusions.	26
2.4	Granules polarize towards the center of the immune synapse. . .	27
2.5	Centralization factor analysis. . . . .	28
2.6	PTEN depletion enhances F-actin accumulation in protrusions. .	29
2.7	Granule fusion occurs at the base of synaptic protrusions. . . . .	31
2.8	WASP and WAVE2 segregate at the synapse. . . . .	33
2.9	WASP and WAVE2 control distinct subsets of protrusions. . . . .	35
2.10	WASP and WAVE2 depletion induces spatially different patterns of force exertion. . . . .	37
2.11	WASP and WAVE2 depletion induce distinct functional phenotypes.	38
2.12	WASP and WAVE2 depletion induce distinct functional phenotypes.	40
2.13	WASP controls target cell deformation at the IS. . . . .	42
2.14	CTLs physically manipulate the target cell surface. . . . .	43
2.15	Target volume analysis. . . . .	44
2.16	Cytolytic mechanopotentiation by WASP-dependent synaptic protrusions. . . . .	45
3.1	Degranulation is spatiotemporally correlated with force exertion at the IS. . . . .	61
3.2	LFA-1 is required for synaptic force exertion. . . . .	63
3.3	Model of antibody blocking of LFA-1 and small molecule-mediated T cell activation. . . . .	64
3.4	Measuring degranulation via flow cytometry. . . . .	65
3.5	LFA-1 is required for synaptic force exertion, degranulation, and cytotoxicity. . . . .	66
3.6	LFA block prevents release of granzyme B. . . . .	67
3.7	LFA-1 blockade disrupts CTL degranulation. . . . .	68
3.8	LFA-1 blockade alters only some indices of T cell activation. . .	69
3.9	Degranulation occurs in IS domains containing both ligand-bound TCR and ligand-bound LFA-1. . . . .	70

3.10	CTL stimulation with spatially segregated ligands on beads. . . . .	71
3.11	CTL stimulation with spatially segregated ligands via micropatterning. . . . .	72
3.12	Degranulation occurs in IS domains containing both ligand-bound TCR and ligand-bound LFA-1. . . . .	74
3.13	Local TCR signaling induces adjacent integrin activation. . . . .	75
3.14	LFA-1 pulling forces define degranulation domains. . . . .	77
3.15	Talin is required for LFA-1 mediated force exertion, degranulation, and cytotoxicity. . . . .	78
3.16	Talin is required for LFA-1 mediated force exertion. . . . .	79
3.17	Talin is required for LFA-1 mediated degranulation, and cytotoxicity. . . . .	80
3.18	Talin depletion inhibits degranulation but not early TCR signaling.	82
3.19	B16F10 cells do not express ICAM-1. . . . .	83
3.20	Talin, but not LFA-1, is required for CTL-mediated killing of B16F10 cells. . . . .	85
3.21	Mechanical licensing of degranulation by integrin adhesions. . . . .	87

## LIST OF ABBREVIATIONS

ADAP	Adhesion- and degran.-promoting adaptor protein
Akt	Protein Kinase B
APC	Allophycocyanin
APC	Antigen presenting cell
Arp2/3	Actin related protein-2/-3 complex
Bak	BCL2 antagonist/killer 1
Bax	BCL2 associated X
BID	BH3 interacting-domain death agonist
$Ca^{2+}$	Calcium ion
CAR	Chimeric antigen receptor
CD3 $\zeta$	Cluster of differentiation 3 zeta-chain
CD11a	Cluster of differentiation 11a
CD28	Cluster of differentiation 28
CD45	Cluster of differentiation 45
CD69	Cluster of differentiation 69
CD107a	Cluster of differentiation 107a, see Lamp-1
Cdc42	Cell division control protein 42 homolog
CLP	Common lymphoid progenitor cells
CRAC	Calcium release-activated channel
CRISPR	Clustered regularly interspaced short palindromic repeats
cSMAC	Central supramolecular activation cluster
CTL	Cytotoxic T lymphocyte
DAG	Diacylglycerol
DMSO	Dimethylsulfoxide
dSMAC	Distal supramolecular activation cluster
Endoplasmic reticulum	ER
ERK	Mitogen-activated protein kinase
F-actin	Filamentous actin
FITC	Fluorescein isothiocyanate
G-actin	Globular actin
GEF	Guanine nucleotide exchange factor
GFP	Green fluorescent protein
gRNA	Guide RNA for CRISPR
GTPase	Guanosine triphosphatase
Gzmb	Granzyme B
H2Kb-OVA	OVA presented by the class I MHC protein
HSC	Hemaetopoietic stem cells
ICAM-1	Intercellular adhesion molecule 1
IFN $\gamma$	Interferon gamma
I $\kappa$ B	Inhibitor of kappa B

IL-2	Interleukin-2
ILP	Invadosome-like protrusion
<i>IP</i> <sub>3</sub>	inositol 1,4,5-trisphosphate
InsP3R	Inositol trisphosphate receptor
iRFP670	Infrared fluorescent protein 670
IS	Immunological synapse
ITAM	Immunoreceptor tyrosine-based activation motif
Lamp1	Lysosomal-associated membrane protein 1
LAT	Linker for activation of T cells
Lck	Lymphocyte-specific protein tyrosine kinase
LDH	Lactate dehydrogenase
LFA-1	Lymphocyte function-associated antigen 1
LG	Lytic granules
MAPK	Mitogen-activated protein kinase
MHC	Major Histocompatibility Complex
MTOC	Microtubule organizing center
MTP	Membrane tension probe
Nck	Non-catalytic region of tyrosine kinase protein
NF $\kappa$ B	Nuclear factor kappa-light-chain-enhancer of activated B cells
NK	Natural killer
NPF	Nucleation promoting factor
NT	Non-targeting
OT-1	TCR specific for the OVA peptide
OVA	Ovalbumin 257-264 peptide (sequence: SIINFEKL)
PAMP	Pathogen-associated molecular pattern
PDMS	Polydimethylsiloxane
PFA	Paraformaldehyde
pHluorin	pH-sensitive GFP
PI3K	Phosphoinositide 3-kinase
<i>PIP</i> <sub>2</sub>	Phosphatidylinositol-4,5-bisphosphate
<i>PIP</i> <sub>3</sub>	Phosphatidylinositol-3,4,5-trisphosphate
PKC $\theta$	Protein kinase C theta
PLC $\gamma$	Phospholipase gamma
PMA	Phorbol 12-myristate 13-acetate
PMAi	Phorbol 12-myristate 13-acetate and ionomycin
pMHC	Peptide-MHC, see MHC
pN	Piconewton
pSMAC	Peripheral supramolecular activation cluster
RAG	Recombination-activating gene
Ras	Rat sarcoma virus protein
RFP	Red fluorescent protein
SA	Streptavidin
STIM1	Stromal interaction molecule 1

TCR	T cell receptor
Vav1	Vav Guanine Nucleotide Exchange Factor 1
WASP	Wiskott-Aldrich syndrome protein
WAVE2	WASP-verprolin homolog 2
WT	Wild-type
YFP	Yellow fluorescent protein

# CHAPTER 1

## INTRODUCTION AND BACKGROUND

### 1.1 The immune system and T cells

The majority of organisms have an immune system, defined as a biological network of processes that defend the host organism against foreign pathogens and disease, that is vital for maintaining homeostasis. For mammalian immune systems, this network is broadly broken into two major arms: the innate immune system and the adaptive immune system. The innate immune system responds initially to pathogens but is limited in the molecular scope of the threats it responds to, as it uses pathogen-associated molecular patterns (PAMPs) to trigger its activity, which are generally conserved. Therefore the innate immune system responds faster but generically to pathogens - which, while useful to the host for clearing the majority of infectious agents, means the innate immune system can be overwhelmed by pathogens that may have evolved to evade innate immune system processes. It is this circumstance that creates the need for an adaptive immune system.

The adaptive immune system responds much more slowly than the innate immune system, using this time to harvest and collect antigen and begin upramping of its antigen-specific molecular processes. The adaptive immune system is composed of two major types of cells (called lymphocytes): B cells and T cells. B cells (named for originating from the bone marrow) produce antibodies that specifically bind to antigens and identify their bound partners as foreign entities meant for destruction. T cells on the other hand (named for originating in the thymus) directly manage the cytotoxic activity of the adaptive immune system.

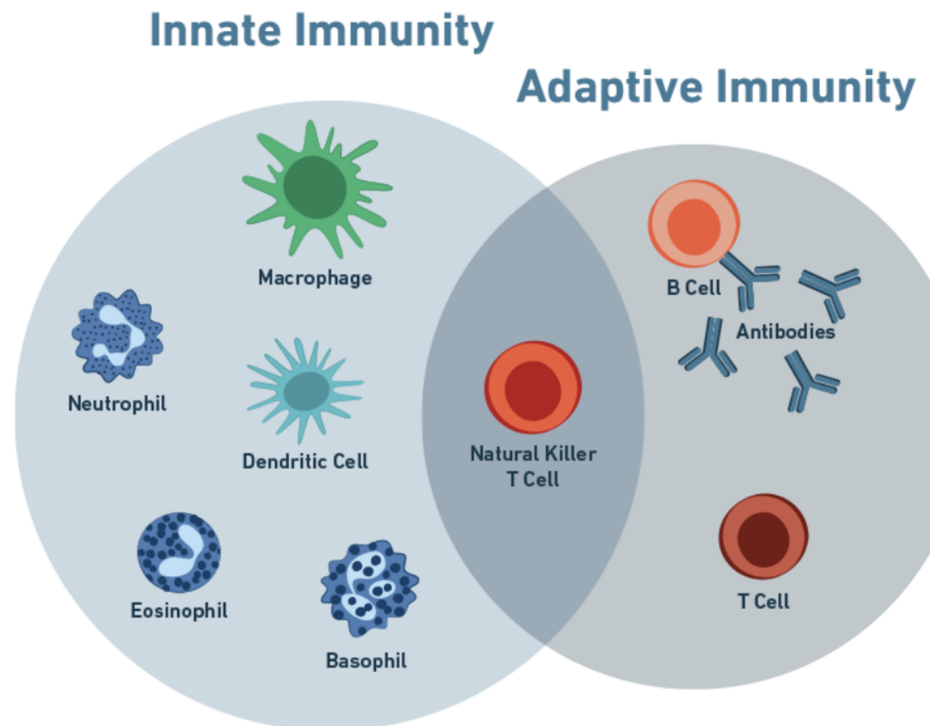


**Figure 1.1:** Cell types of the innate vs. the adaptive immune system

A schematic Venn diagram of the immune system. The typical conception of the vertebrate immune system is typically two-armed, broken into a faster-but-general responding innate immune system (left), and a slower-but-more-specific adaptive immune system (right), of which T cells are a part of. Almost all cell types that modern immunology research is concerned with falls somewhere within these two circles or their overlap - some immunology research is interested in characterizing certain effector or support immune cell types that fall in between innate and adaptive immunity (or can transfer their skills and interface between the two, calling into question the ontics of "innate" and "adaptive" immune systems) [1]. This figure is adapted from [2].

T cells are composed of two main functional subtypes: CD8+ killer T cells (the primary focus of this thesis and heretofore referred to as any of the following: cytotoxic T lymphocytes (CTLs), cytotoxic T cells, CD8+ T cells) and CD4+ helper T cells.

## 1.2 T cell development

T cells as a whole are defined by their expression of the T cell receptor (TCR), the receptor responsible for recognizing foreign antigenic peptide presented by the target cell via its Class I or Class II Major Histocompatibility Complex (MHC, or pMHC). The TCR is multi-subunit receptor that is composed of varying combinations of  $\alpha$ -,  $\beta$ -,  $\gamma$ -,  $\delta$ -,  $\epsilon$ -, and  $\zeta$ -chains, whose specific combination defines the unique sub-identity of the T cell, although the vast majority of T cells (95%+) express the  $\alpha$  and  $\beta$  chains and are thus called  $\alpha\beta$  T cells. There are a number of additional co-receptors that bind (either directly or indirectly) to the TCR. The most relevant to  $\alpha\beta$  T cells are the CD8 or CD4 co-receptors, mentioned above. These co-receptors transduce differing signals within the specific T cell and additionally define the specificity of the  $\alpha\beta$  T cell to the two different classes of MHC: CD8+ T cells bind to MHC Class I, while CD4+ T cells bind to MHC Class II.

The ability of T cells to properly recognize and engage only with foreign antigen while ignoring self-peptides is tightly regulated and begins at a very early stage in immune system development. T cells derive from hematopoietic stem cells (HSCs) that originate in the bone marrow. HSCs then ultimately differentiate into common lymphoid progenitor cells (CLPs), which migrate to the thymus to ultimately differentiate into natural killer (NK), B, or T cells.

The process of differentiating into T cells is primarily motivated by the need to create a functional TCR that does not react to self-antigen but does react to foreign antigen. As TCRs are made up of alpha and beta chains that are evolved to react to a wide range of possible antigens that an organism may encounter in

its lifespan, T cell differentiation has been characterized in a stepwise manner that first begins with TCR-beta chain selection. T cells at this stage express an invariant pre-alpha chain called pre-T $\alpha$  that the varying beta chains (generated by VDJ recombination of the TCR-beta locus) attempt to form a stable binding partner with. Once an appropriate TCR-beta chain is identified as capable of stable binding to pre-T, the same process begins on the TCR- $\alpha$  chain against the now mature TCR- $\beta$  chain, generating a stable (but not necessarily functional) TCR.

Once a stable TCR heterodimer has been formed, the T cells must undergo a process of selection in order to build a functional repertoire of TCRs, called positive and negative selection. Positive selection involves presenting the T cells with self-antigen presented on MHC with the selection criteria of being able to bind with this complex. T cells that cannot bind either MHC Class I or Class II via their TCR will die (called "death by neglect" - this removes cells with TCRs that are unable to bind self-MHC which is functionally useless to the organism, or may be able to bind non-self MHCs, which is also functionally useless), while those T cells that can will survive. Those T cells that are able to bind to an MHC complex presenting self-antigen receive a survival signal. Therefore, the body positively filters/selects for T cells with TCRs that can recognize MHC molecules leaving those that cannot recognize MHCs to die off [3].

After obtaining T cells that are capable of binding to MHC molecules, the next step is to select for T cells that do not auto-react to self-antigen, called negative selection. This ensures that T cells are tolerant of self-antigen and prevents auto-immunity conditions in the organism. In this stage of selection, T cells that bind to MHC presenting self-antigen and activate receive an apoptotic signal

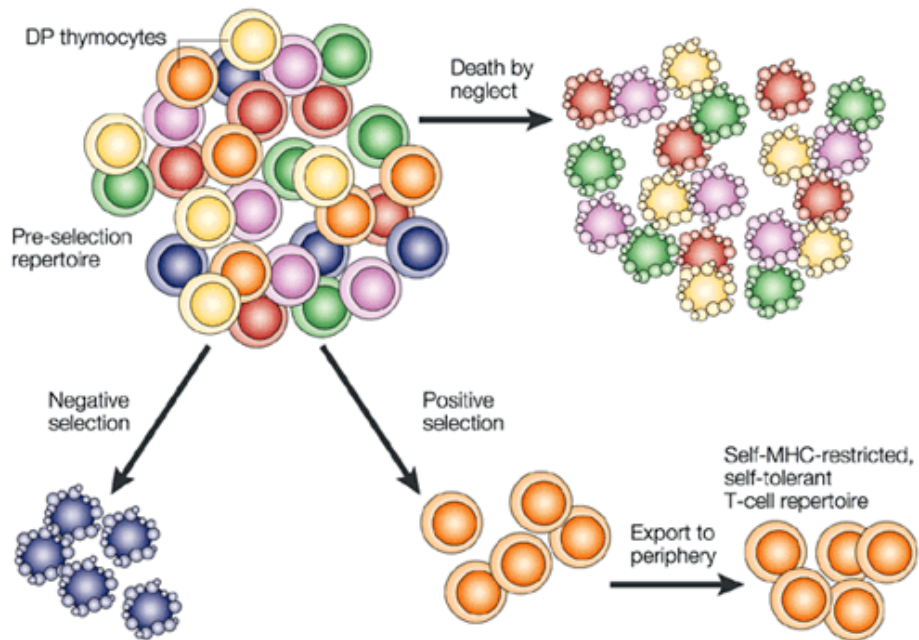


**Figure 1.2:** Positive and negative selection

Thymocytes that are double positive (DP) for CD4+ and CD8+ begin with an unselected repertoire of TCRs. The process of positive selection ensures that DP thymocytes that do not bind MHC Class I or II die ("death by neglect"), while those that do bind MHC will receive a signal to survive. Negative selection filters out TCRs that are too reactive to self-antigen, which would be intolerable for a functioning immune system. These selection processes results in the generation of T cells that are self-MHC restricted, self-antigen tolerant T cells that are ready to fight potential infection. This figure is adapted from [3].

that leads to cell death. Negative selection therefore prunes the T cell population for T cells that can not only bind to MHC but do not react to self-antigen. The vast majority of thymocytes (98%+) fail to pass positive and negative selection. Following positive and negative selection, the resulting T cell set can therefore bind to any antigen (presumably belonging to any foreign pathogen) so long that the antigen is distinct from the body's self-antigens. After these stages of T cell development, these T cells (called naïve T cells) then exit the thymus and begin to circulate in the host, where they will spend their time surveying the host for disease and foreign antigens.

### 1.3 TCR activation and downstream signaling

If a CD8+ T cell engages an infected cell presenting foreign peptide, the T cell will initiate a cascade of antigenic-specific intracellular signaling events. Upon ligation of the TCR to the pMHC complex, the CD3 proteins (CD3 $\epsilon\gamma$  and CD3 $\epsilon\delta$  heterodimers and a CD3 $\zeta$  homodimer) bearing ITAM (immunoreceptor tyrosine-based activation motif) also bind to the TCR. The ITAMs on the CD3 $\zeta$  get phosphorylated, so that cytosolic signaling proteins can bind to phosphorylated ITAMs and propagate the signal from the triggered TCR further downstream into the T cell. CD3 $\zeta$  contains three ITAMs, while CD3 $\delta$ , CD3  $\gamma$ , and CD3 $\epsilon$  all only contain one ITAM. The CD3 chains are needed as the cytosolic tail of the TCR is extremely short and structurally do not support significant adaptor features for signal amplification molecules. This modularity also allows for an increased range of TCR signaling for fine-tuning key features of the T cell effector response (e.g. killing, proliferation, signaling, cytokine secretion) in response to a number of diverse inputs such as antigen strength, lifetime of interaction, and number of bound-TCRs at the IS.

The phosphorylated CD3 ITAMs recruit the protein tyrosine kinase ZAP70 that binds to the phosphorylated tyrosine motifs via its SH2 domain. This brings ZAP70 closer to CD8-bound Lck, which further phosphorylates ZAP70, activating ZAP70. Upon Lck-mediated phosphorylation of ZAP70, ZAP70 itself phosphorylates and activates the transmembrane protein called linker for activation of T cells (LAT). LAT acts as a scaffold, providing binding sites for a number of signaling molecules (via its own phosphorylated sites) that link these signaling molecules, including the lymphocyte cytosolic protein 2 (SLP76) which

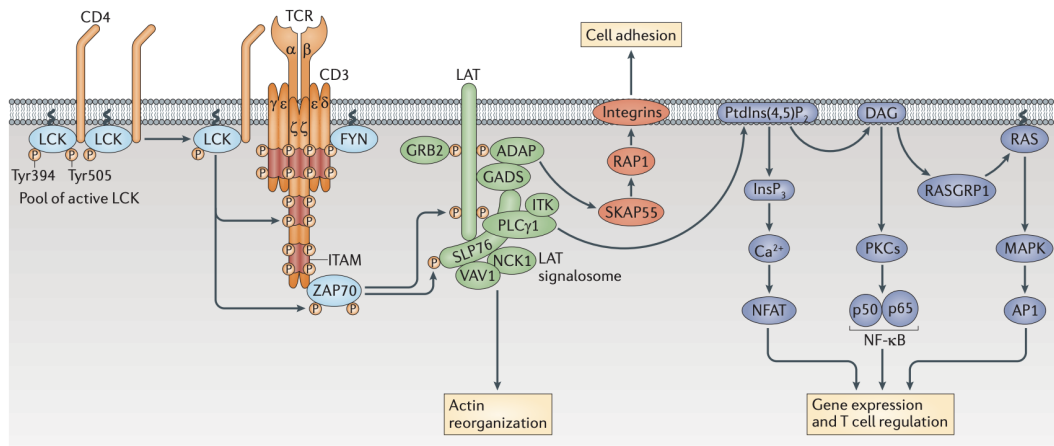


**Figure 1.3:** The T cell receptor and its signaling partners

An overview of TCR signalling. Signaling through the TCR commences upon recognition of cognate pMHC on the target surface. The assembly of the CD3 $\gamma$ ,  $\delta$ , and  $\zeta$ -chains recruits Lck, which phosphorylates the ITAMs of the CD3 $\gamma$ ,  $\delta$ , and  $\zeta$  chains, recruiting ZAP70. Activated ZAP70 primes the LAT signalosome to coordinate critical signaling molecules such as PLC $\gamma$ , GRB2, SLP76, ADAP, ITK, Nck1, and VAV1. The LAT signalosome is a node for three major signaling pathways: the  $Ca^{2+}$ , the MAPK, and the NF- $\kappa$ B pathway, which initiate critical signaling pathways for the expansion, differentiation, and activation of T cells. These signals also modify integrin signaling, which strongly influences cytoskeletal dynamics and therefore adhesive and migratory behavior. The figure is adapted from [4].

provides even further additional binding sites on the LAT signaling complex, SOS, GRB2, ITK, Vav, Nck1, and FYB (or ADAP), in space and time.

One of the most crucial signaling molecules that binds to LAT is the protein phospholipase  $C\gamma 1$  (PLC $\gamma$ ), which generates key lipid secondary messenger molecules. Phosphatidylinositol 4,5-bisphosphate ( $PIP_2$ ) is an input to PLC $\gamma$  function. Once phosphorylated and activated by Itk, PLC $\gamma$ 's enzymatic activity (using  $PIP_2$  as a substrate) generates two products: diacylglycerol (DAG) and the soluble inositol 1,4,5-trisphosphate ( $IP_3$ ). Diacylglycerol accumulates in the IS, which prompts recruitment of the microtubule motor protein dynein and drives polarization of the microtubule-organizing center (MTOC) [5] and the

recruitment of lytic granules to the immune synapse (further discussed in the T cell degranulation and target cell death introduction section [6].  $IP_3$  is soluble and diffuses throughout the cytosol, eventually binding to its receptor inositol trisphosphate receptor (InsP3R), located on the endoplasmic reticulum (ER). The binding of  $IP_3$  to InsP3R triggers release of calcium ( $Ca^{2+}$ ) ions into the cytosol, initiating calcium-dependent transcription programming. These include the NFAT, NF- $\kappa$ B, and AP1 signaling pathways, all of which assist in fully activating the T cell. Another notable lipid secondary messenger is phosphatidylinositol (3,4,5)-trisphosphate ( $PIP_3$ ).  $PIP_2$  is phosphorylated by the phosphoinositide 3-kinase (PI-3K) to give  $PIP_3$ , which further activates downstream signaling proteins, most notably Akt, which is highly involved in T cell metabolism.

When calcium depletion is detected in the cytosol by the STIM1 protein, calcium release-activated channels such as Orai1 are activated to replenish cytosolic calcium. This calcium flux is a required step for lymphocyte degranulation [7].

The generation of spatial gradients and patterns of lipid secondary messenger molecules at the plasma membrane is highly consequential, resulting in the formation of a necessary killing and major signaling structure called the immune synapse.

## 1.4 The immunological synapse and the T cell cytoskeleton

The immunological synapse (also called the immune synapse) is the highly organized, structurally stereotyped interface that T cells form against an APC. It is classically characterized as a concentric, annular structure that bears a "bulls-eye" center surrounded by a ring of filamentous actin (see Figure 1.4, left). The

immune synapse is a major T cell signaling and killing megastructure, and robust formation of the immune synapse is essential for the T cell to achieve its maximal cytotoxic efficacy, in particular when concerned with lytic granule secretion [8].

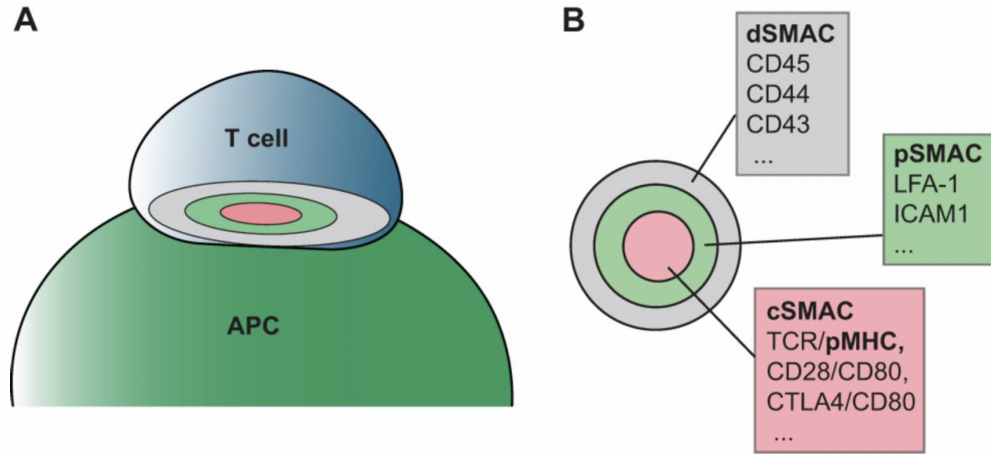


**Figure 1.4:** The immunological synapse

**A:** A schematic of the canonical model of the immune synapse. The T cell (blue, above) is in contact with the APC (green, below). The IS is shown as a series of interfacial concentric rings. **B:** The IS is classically divided into three regions, extending from the center outwards: the cSMAC, the pSMAC, and the dSMAC. The proper formation of the IS results in functionally distinct and biochemically patterned regions. This figure is adapted from [9].

Upon TCR activation, the actin cytoskeleton rapidly polymerizes and organizes itself to achieve an annular arrangement, forming the IS. Existing work in the field highlights the necessity of  $PIP_3$  accumulation at the synapse for step-wise formation of actin structures [10].  $PIP_3$  recruits the guanine exchange factor Dock2, which locally activates the Rho family GTPase Rac. This activated Rac then signals to the Wiskott-Aldrich syndrome protein family member 2 (WAVE2), generating lamellipodial growth [10, 11]. Lipid gradients also control Cdc42, another Rho family GTPase. Together,  $PIP_2$  and Cdc42 (activated by Vav1 [12]) activate the Wiskott-Aldrich syndrome protein (WASP), generating filopodia [13].

WASP and WAVE2 are actin nucleation promoting factors that activate nucleation factors such as Arp2/3, which themselves resist the inhibition of spontaneous actin polymerization (by proteins such as profilin) by acting as actin nucleation seeds [14]. Actin nucleation (-promoting) factors are essential for proper cytoskeletal remodeling, and the role of WASP and WAVE2 on immune synapse dynamics is the subject of 2, where their function proves to be critical for cytotoxicity.

From a macromolecular perspective, the IS is segregated into three supramolecular activation clusters (SMACs), called the central, distal, and peripheral supramolecular activation clusters (cSMAC, pSMAC, and dSMAC)

Broadly, disrupted synapse formation (ranging widely from organization in space, organization in time, and presence/absence of certain molecular players) can dramatically affect T cell cytotoxicity. This highlights the functional importance of the immune synapse.

## 1.5 T cell degranulation and target cell death

The killing mechanism of CTLs is fundamental to robust anticancer and antiviral responses. CTLs achieve their cytotoxic effects by managing a two-pronged approach 1. specifically destroying only infected or oncogenic target cells (recognized via ligation between the TCR and its specific pMHC interaction) and 2. preserving the integrity of the surrounding healthy bystander tissue. Spatially, these aims are realized through the precise signaling mechanisms of the immune synapse.

The T cell has evolved countless mechanisms in order to balance this dual mandate. The most prevalent mechanism of T cell-mediated killing of target cells involves the secretion of the hydrophobic protein perforin and granzyme proteases through the immune synapse, called degranulation [15, 16]. When released, perforin oligomerizes in a calcium dependent manner [17] and forms pores on the target cell surface, (around 16nm in diameter) [18], inducing significant membrane damage. The target cell responds to this traumatic event at the plasma membrane using a mechanism that permits granzymes entry to the cytoplasm, where they cleave apoptotic substrates that induce apoptosis [19]. Because all cell types are capable of being killed and cleared in this way (that is to say, both infected and healthy cells), specialized mechanisms have evolved over time in immune cells to ensure that the effects of perforin and granzyme are constrained to the target cell alone.

Cytotoxic T lymphocytes store their perforin and granzymes in specialized secretory lysosomes called lytic granules (0.5 to 2  $\mu\text{m}$ ) [20], whose acidic pH environment quenches the lytic and apoptotic activity of both proteins [21, 19]. Following mere minutes of target cell recognition, the lytic granules are trafficked along microtubules to the immunological synapse (IS). At this site, they fuse with the plasma membrane, releasing their contents into the intercellular space.

At the same time, F-actin and the associated actin nucleation promoting factors (NPFs) at the IS undergo significant spatiotemporal remodeling. This results in a highly complex landscape of highly dynamic actin sheets and protrusions [8]. Canonically, actin clearance from the center of the immune synapse (cSMAC) is required for fusion of lytic granules to the center of the synapse [8].

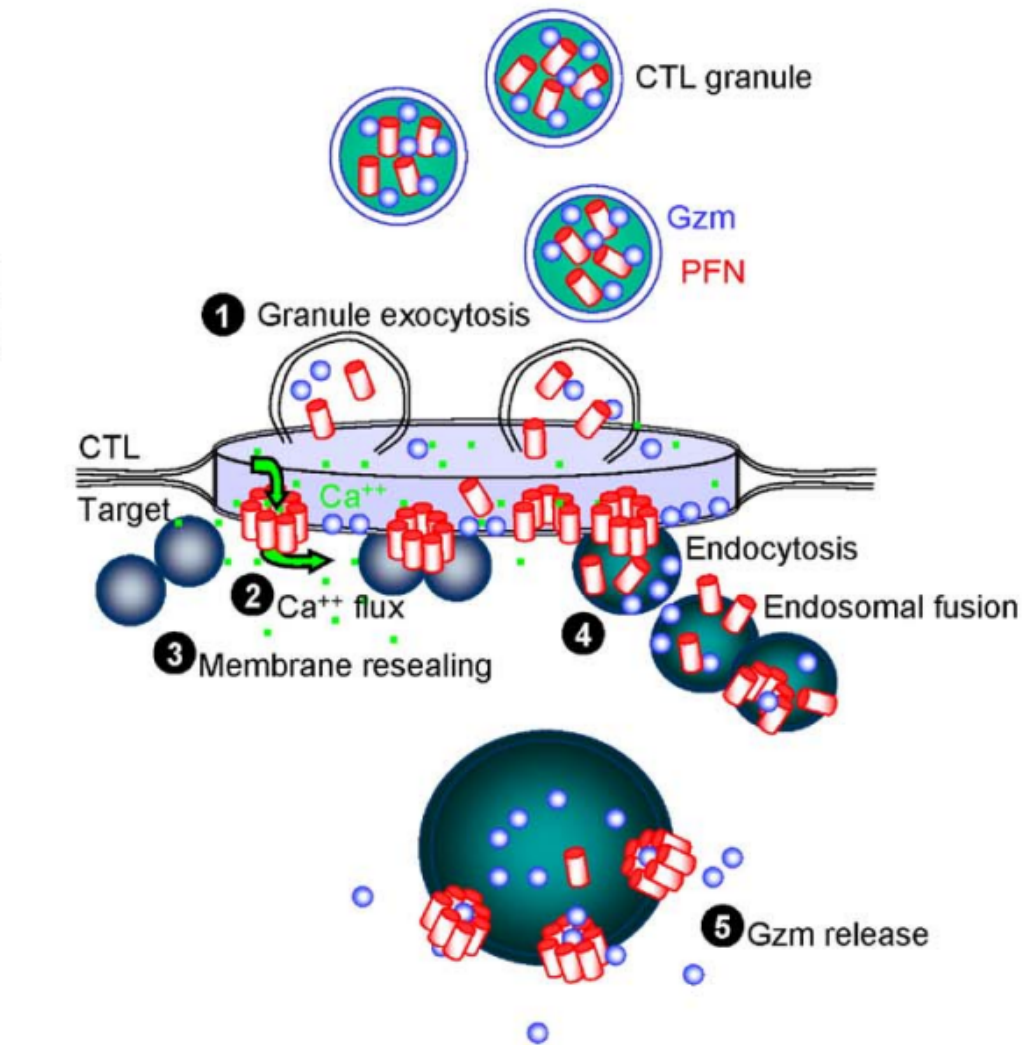


**Figure 1.5:** Lytic granule secretion and perforin pore formation

A schematic of lytic granule secretion and entry of perforin and granzyme into the target cell. Lytic granules are coordinated to the immune synapse and selectively fuse at the synapse, emptying their cytotoxic contents, perforin (red) and granzymes (blue), into the intercellular space. Perforin requires the presence of calcium ions ( $\text{Ca}^{2+}$ , green) to pierce the target cell membrane. and permit entry of granzyme proteases. Target cell membrane repair programs begin to repair the damaged membrane. The resealing of the target membrane results in endocytosis of intercellular granzyme and perforin (as well as  $\text{Ca}^{2+}$  ions), which again re-pierce the endocytic vesicular membrane and allow for true granzyme entry into the cytosol. where granzymes cleave apoptotic effectors. This figure is adapted from [22].

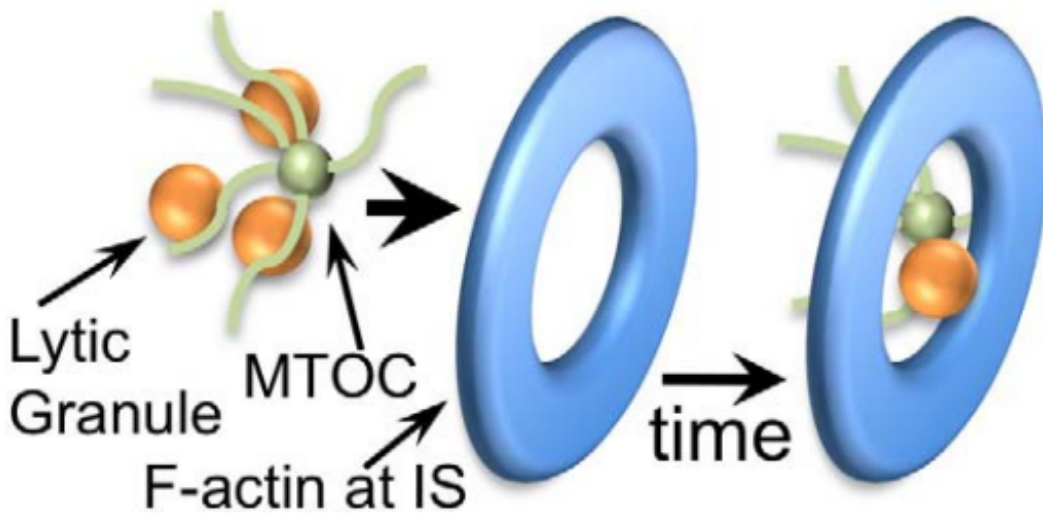


**Figure 1.6:** Canonical model of actin clearance as a necessary condition for lytic granule secretion

Model of central actin clearing for MTOC polarization and lytic granule fusion. Upon TCR activation, MTOC polarizes towards the immune synapse with the assistance of the motor protein dynein, bringing lytic granules towards the IS and docking them in preparation for degranulation. The actin meshwork clears from the center of the IS, forming a mature dSMAC actin-ring (as well as the associated pSMAC and cSMAC) and exposing available synaptic membrane for degranulation. This figure is adapted from [23].

Newer, more recent models of degranulation highlight the need for transient actin polymerization at the site of degranulation to potentiate the pore forming effects of perforin [24]. This is related to T cell mechanical force exertion against the target, which significantly amplifies T cell effector function [24].

## 1.6 T cell mechanical force exertion

Immune cell-immune cell interactions are typically described as a series of interrelated biochemical receptor-ligand signaling processes (and this introduction has done the same). While this characterization is not incorrect, it ignores the

mechanical dimension of immune cell interactions, which have been identified as a significant hubs of cellular decision making. Immune cells have been demonstrated to have a number of biophysical sensing functions, including cancer cell surveillance and immune cell function and cytotoxicity.

The CTL immune synapse has been shown to be a physically dynamic structure, capable of exerting force against a resisting target or surface and

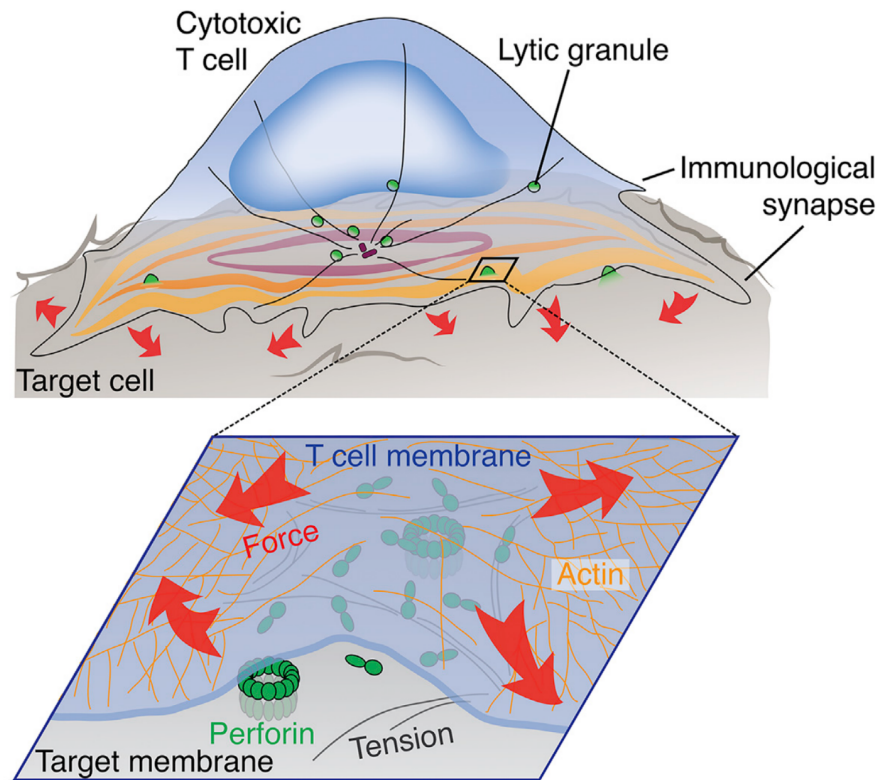


**Figure 1.7:** T cells exert mechanical force against target cells

Illustration of T cell force exertion against the target cell. T cells use biophysical force (via cytoskeletal proteins such as actin) in concert with biochemical signaling axes to optimize their own activation and cytotoxic programming. This force focuses the secretion of lytic granules and the pore-forming effect of perforin. This figure is adapted from [23].

Some recent studies demonstrate that the actin-rich structures formed during T cell adhesion and degranulation are actually involved in boosting the lytic

activity of perforin by dynamically applying mechanical force against the target cell [25, 24] and sensitizing the target cell to perforin insertion, which must overcome the hydrophobic interior of the plasma membrane in order to pierce the target cell plasma membrane and trigger cell lysis.

Recent work has provided insight into how the TCR can distinguish single amino acid substitutions in short peptides. Previous research has shown that the  $\zeta$ -chain of the TCR undergoes conformational changes to expose phosphorylation sites in its ITAM domains<sup>67</sup>. Other work has shown that the TCR is an anisotropic mechanosensor that requires force orthogonal to the IS for the induction of calcium signaling<sup>68</sup>. The model that these two observations suggest is that force is required to expose ITAM domains on the TCR, which leads to the induction of membrane proximal signaling. Furthermore, the TCR-pMHC interaction has been shown to function as a catch bond<sup>69</sup>. A catch bond is a type of bond in which application of a force increases the lifetime of the interaction. It was shown that the capacity to form a catch bond plays a critical role in enabling the TCR to discriminate between high and low affinity agonists<sup>69</sup>. Together these studies demonstrate the important role of mechanobiology in TCR activation and signaling.

The IS has been shown to be a dynamic and physical structure that is capable of exerting mechanical force<sup>70,71</sup>. Naïve T cells have been shown to exert mechanical force on polydimethylsiloxane (PDMS) pillars coated with activating proteins<sup>71</sup>. It is conceivable that T cells could exert forces as a way of sensing the mechanical properties of activating surfaces. This is supported by previous research demonstrating that T cells are more strongly activated on softer rather than stiffer PDMS surfaces, as measured by cytokine production and prolif-

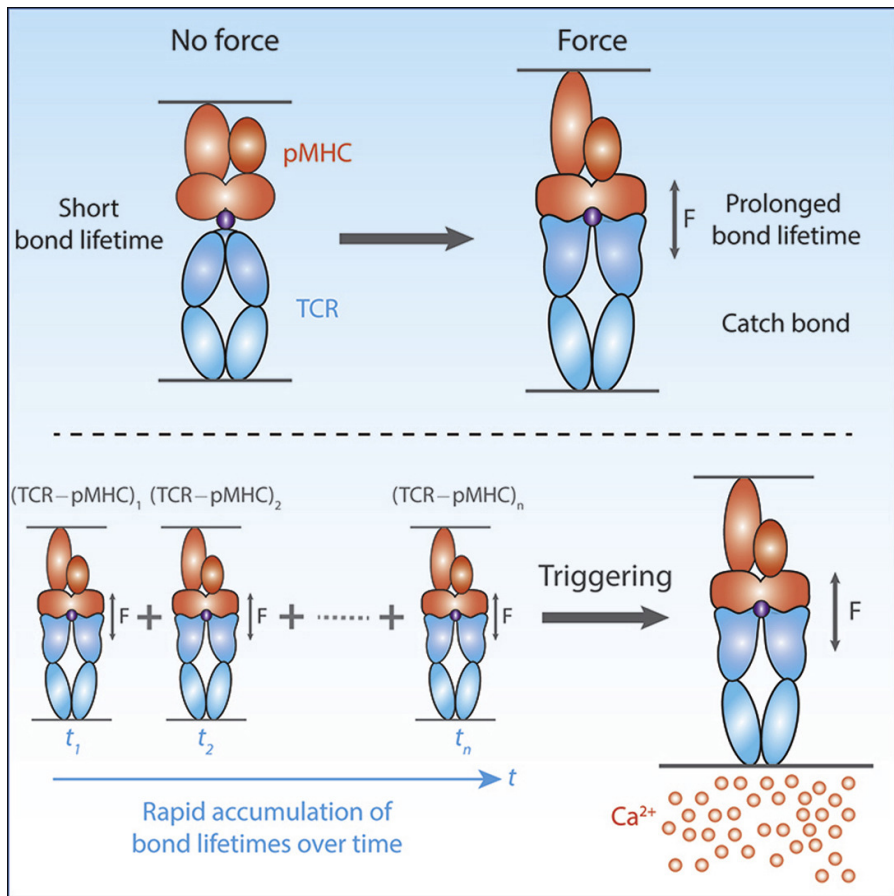


**Figure 1.8:** Mechanosensitive receptors of the immune synapse

An illustration of the principle of mechanosensitive receptors. The lifetime of a receptor-ligand interaction in response to applied force across the bond can either significantly increase the lifetime of the bond (a catch bond) or rapidly decrease (slip bond). The TCR is an example of a mechanosensitive receptor - it demonstrates catch bond behavior with applied force. If a sufficient accumulation of signaling bonds accrue (here, the TCR) then TCR activation is triggered (e.g. flux of  $Ca^{2+}$  ions, see 1.3) and highly potentiated by the increased avidity and number of active TCR-pMHC bonds. This figure is adapted from [26].

eration72. Activating peripheral blood mononuclear cells (PBMCs) on softer surfaces with CD3/CD28 antibodies tended to increase shedding of CD62L, which is a consequence of T cell activation<sup>72</sup>. This is intriguing because the opposite phenomenon has been observed for naïve mouse T cells activated on polyacrylamide surfaces with CD3/CD28<sup>73</sup>. Possible explanations for this discrepancy include a difference between human and mouse cells. It is also

possible T cells respond differently to antibodies on PDMS and polyacrylamide surfaces. Further research is needed to understand the precise role of surface tension on T cell activation. Yet, these studies are intriguing and support the concept that signaling and cell biology are not merely biochemical reactions. These observations show that mechanical properties of biology are important factors that have been largely overlooked in immunology until recently.

## 1.7 Thesis Aims

The further successful development of immune cell therapies thus far has been and will continue to be dependent on a deeper understanding of basic T cell effector function. To this end, this thesis is chiefly focused on a molecular approach to studying the mechanotransduction of T cell effector function and the dynamic relationships between its biophysical and biochemical dimensions. The results of this study are broken across two chapters, whose contents are summarized below.

While it was known that the CTLs use physical force to amplify the pore-forming effects of perforin and resulting positive correlation between force exertion and target cell death, it was unclear what cellular structures T cells form in order to actualize this force against the target cell membrane and manipulate this relationship. It was also unclear what proteins or molecules were involved in this membrane perturbation/distortion process. Chapter 2 of this thesis will address the results of the experiments testing these outstanding questions through the use of pharmacological and genetic perturbations against the actin nucleation promoting factors (NPFs) Wiskott–Aldrich Syndrome protein (WASP)

and WAVE2 (WASP-verprolin homolog 2) that directly affected T cell force exertion, and studying their resulting cytotoxic capabilities and dynamics via co-culture assays and imaging.

Another outstanding question arose from the observation that T cells degranulate specifically near areas of synaptic force exertion. While this dovetails with the observation that force exertion amplifies the pore-forming effects of perforin (as discussed in the Introduction and Chapter 2), it was unknown what types of forces or interactions coordinated these two phenomena of degranulation and synaptic force exertion so that they could be unified in space and time. It was also unknown what force-sensitive molecules could be mediating this intercellular communication. Chapter 3 addresses the study conducted to address these questions, which also used pharmacological and genetic perturbations against integrins (primarily lymphocyte function-associated antigen 1, or LFA-1) on T cells in order to modify the force output of these T cells and change their degranulation and cytotoxic behavior as observed through co-culture assays and unique and creative imaging experiments. Altogether, this thesis aims to clarify the specifics of the T cell killing event (encompassing T cell force exertion and degranulation) in order to better inform future T cell studies and therapy design.

## CHAPTER 2

# INTERFACIAL ACTIN PROTRUSIONS MECHANICALLY ENHANCE KILLING BY CYTOTOXIC T CELLS

Results presented in this chapter have been published as: Tamzalit, F., Wang, M. S., Jin, W., Tello-Lafoz, M., Boyko, V., Heddleston, J. M., Black, C. T., Kam, L. C., and Huse, M. *Interfacial actin protrusions mechanically enhance killing by cytotoxic T cells*. Science Immunology. 2019 Mar 22;4(33).

### 2.1 Background

Dynamic cell-cell interactions coordinate bidirectional information transfer in the immune system and control the potency and the scope of effector responses [27]. One of the most important of these interactions is the immunological synapse (IS) formed between a cytotoxic T lymphocyte (CTL) and the infected or transformed target cell it aims to destroy [15] (3). IS formation is rapidly induced by recognition of cognate peptide-major histocompatibility complex (MHC) on the target cell by T cell antigen receptors (TCRs) on the CTL. Once firm contact is established, the CTL secretes a toxic mixture of granzyme proteases and the hydrophobic protein perforin into the intercellular space. Perforin forms pores in the target cell membrane that stimulate the uptake of granzymes into the cytoplasm, where they induce apoptosis by cleaving specific substrates (4). Perforin- and granzyme- mediated killing is the most prevalent mode of lymphocyte cytotoxicity, and it likely plays an important role in cellular immunotherapy approaches against cancer (5).

IS formation is accompanied by dramatic reorganization of both microtubules and filamentous actin (F-actin) (6). Within minutes of TCR stimulation, the centrosome (also called the microtubule-organizing center) moves to a position just beneath the IS. The centrosome is closely associated with lytic granules, the secretory lysosomes that store perforin and granzyme, and its reorientation positions these granules next to the synaptic membrane (3). This promotes the directional secretion of granule contents into the intercellular space, enhancing both the potency and the specificity of killing. Whether (and how) F-actin remodeling contributes to cytotoxicity is, by comparison, less clear. Our current conception of synaptic F-actin is strongly influenced by imaging studies in which the target cell is replaced by a glass surface or a supported bilayer containing stimulatory TCR ligands. In this context, T cells form radially symmetric synapses characterized by intense F-actin accumulation at the periphery and depletion from the center (7–10). This annular configuration is thought to encourage lytic granule fusion at the center of the IS by clearing F-actin from the plasma membrane in this zone (3, 11, 12). Although this model is conceptually appealing, it is unclear how well it applies to granule release in bona fide CTL–target cell conjugates, where synaptic F-actin rings are less apparent and, when observed, often quite transient. Synaptic F-actin is also highly dynamic, forming protrusions and lamellipodial sheets that exhibit both centripetal retrograde flow and radial anterograde movement (10, 12–15). These dynamics enable T cells to impart mechanical force across the IS (16, 17). In CTLs, the capacity to exert synaptic force is notably correlated with cytotoxic potential (18). Biophysical and imaging experiments suggest that force enhances cytotoxicity by increasing the membrane tension of the target cell, which in turn promotes the pore-forming activity of secreted perforin. Here, we applied microfabrication and high-resolution live imaging to

investigate how CTLs mechanically potentiate the chemical activity of perforin, a process we refer to as mechanopotentiation. Using stimulatory micropillar arrays that trigger IS formation in three dimensions, we have found that lytic granule release occurs at the base of F-actin-rich synaptic protrusions that extend into the antigen-presenting surface. These protrusions, which are generated by the Wiskott-Aldrich syndrome protein (WASP) and the actin related protein (Arp)2/3 actin nucleation complex, are required for synaptic force exertion and cytotoxic efficiency. Our results provide insight into how cytotoxic lymphocytes organize mechanical output and demonstrate how three-dimensional architecture influences the functionality of communicative interfaces in the immune system.

### **2.1.1 Force exertion through the actin cytoskeleton**

PI3K PTEN IS actin dynamics Summarize PI3K and PTEN data

### **2.1.2 Modifying target cell sensitivity to perforin**

distinguish between membrane and cortical tension

## 2.2 Results

### 2.2.1 CTLs form actin-rich protrusions on stimulatory micropillars

Synaptic force exertion can be measured by imaging T cells on arrays of flexible polydimethylsiloxane (PDMS) micropillars bearing immobilized TCR ligands and adhesion proteins (Figure 2.1) (17, 18). T cells form IS-like contacts with these arrays and induce pillar deflections that can be converted into force vectors based on the known dimensions and composition of the pillars. Using this approach, we previously found that lytic granule release tends to occur in regions of active pillar deflection (18). This result raised the possibility that there might be specific structures within the IS that mechanopotentiate perforin function by imparting force in close proximity to granule secretion.

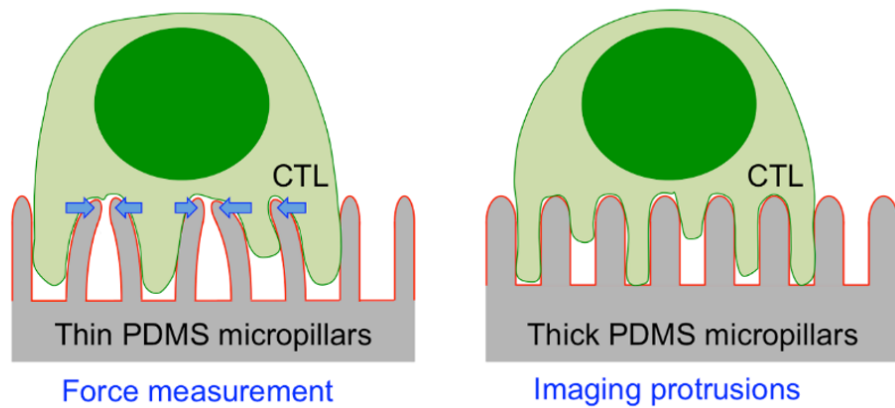


**Figure 2.1:** Using PDMS micropillars as 3D environment to observe and measure CTL cytoskeletal structures.

Schematic diagram of thin micropillars used for force measurements (left) and thicker micropillars used for imaging protrusions (right).

To identify candidate structures that could be involved in this mechanopotentiation, we closely examined the dynamic architecture of CTL synapses on micropillar arrays. For these experiments, we used primary CTLs expressing the OT1 TCR, which is specific for the ovalbumin 257–264 peptide presented by the class I MHC protein H2-K<sup>b</sup> [H2-K<sup>b</sup>–ovalbumin (OVA)]. OT1 CTLs were retrovirally transduced with Lifeact–green fluorescent protein (GFP), a fluorescent probe for F-actin, and imaged by confocal microscopy on micropillars coated with H2-Kb-OVA and ICAM1 (intercellular adhesion molecule 1), a ligand for the  $\alpha$ L $\beta$ 2 integrin LFA1. The pillars in these arrays (1 to 1.5  $\mu$ m in diameter and 4 to 5  $\mu$ m tall) were thicker, shorter, and therefore more rigid than the pillars used for T cell force measurements (0.7  $\mu$ m in diameter and 6  $\mu$ m tall) (Fig. 1A). These thicker pillars are not substantially deflected by CTLs and function as a regularly crenulated stimulatory surface that facilitates quantitative assessment of IS growth in three dimensions.

Within minutes of initial contact with the arrays, the CTLs formed F-actin–rich protrusions that invaded the spaces between adjacent pillars (Figure 2.1). Time-lapse experiments using both confocal and lattice light-sheet microscopy revealed that the F-actin in these protrusions was highly dynamic, coruscating up and down the length of each pillar (Figure 2.1). Periodically, F-actin–free gaps appeared at the base of the protrusions, in the regions around the pillar tops. During protrusion growth, F-actin accumulation was often strongest at the leading edge, implying a causative relationship between actin polymerization and the formation of these structures (Figure 2.3). Most of the microtubule cytoskeleton, by contrast, was constrained to the region above the pillars, although individual microtubules were observed to extend into a subset of protrusions (Figure 2.1). In most cells, the centrosome reoriented to a position in the plane of the pillar

tops but did not proceed into the interpillar spaces. Hence, on micropillar arrays, CTLs form dynamic, F-actin-rich protrusions at the IS that exclude the centrosome.

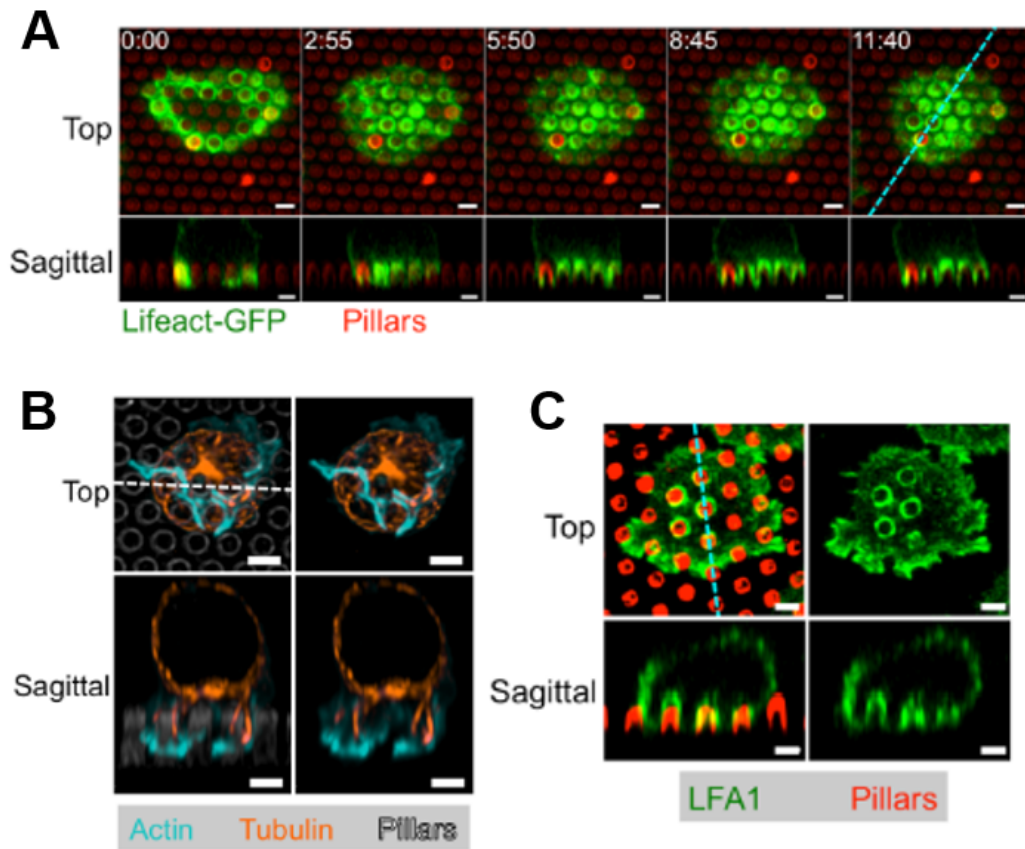


**Figure 2.2:** Characterizing the architecture of protrusions using micropillars.

(A-C): OT1 CTLs were imaged by confocal microscopy on micropillars bearing H2-K<sup>b</sup>-OVA and ICAM1. z-projection images (top views) are shown above with sagittal views below. Dashed lines [cyan in (A) and (C); white in (B)] denote the slicing plane used for the sagittal images. (A): Time-lapse montage of a representative CTL expressing Lifeact-GFP, with micropillars shown in red. (B): Fixed image of a representative CTL stained with phalloidin (to visualize F-actin) and antitubulin antibodies. Micropillars are shown in gray in the left images. (C): Fixed image of a representative CTL stained with anti-LFA1 antibodies, with micropillars shown in red. All scale bars, 2  $\mu$ m.

During initial cell spreading, invasion into the micropillar zone was typically constrained to the periphery of the contact (Figure 2.2). However, once the radial size of the IS stabilized, after around 60s, protrusions formed in the more central

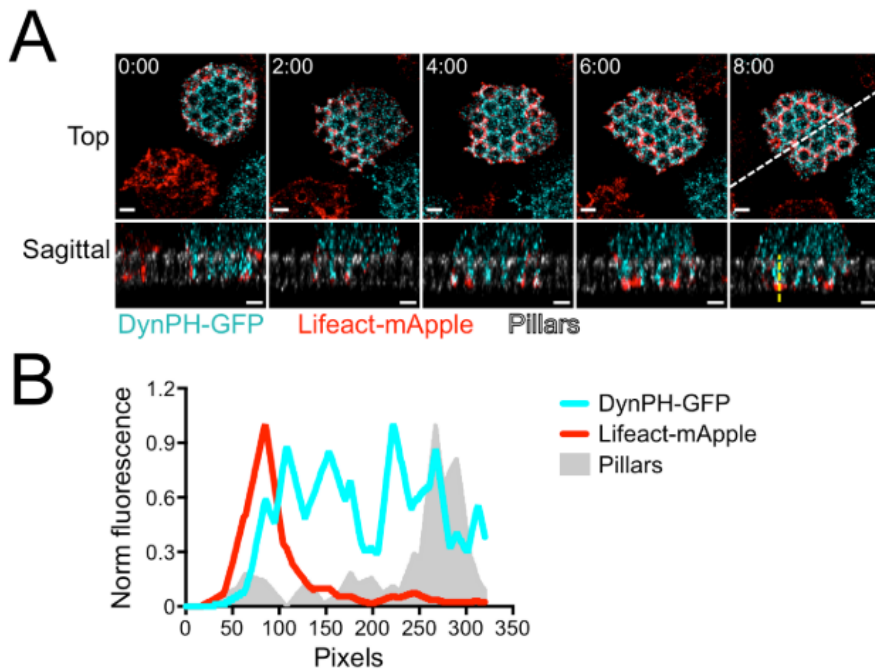


**Figure 2.3:** F-actin accumulates at the leading edges of synaptic protrusions.

OT1 CTLs expressing Lifeact-mApple and DynPH-GFP (a membrane marker) were imaged by confocal microscopy on fluorescent micropillars bearing H2-K<sub>b</sub>-OVA and ICAM1. **(A)**: Time-lapse montage of a representative CTL, with z-projection images (top views) shown above and sagittal views below. The white dashed line denotes the slicing plane used for the sagittal images. Pillars (gray) appear in the sagittal images only. Time in M:SS is indicated in the upper left corner of each top view. Scale bars = 2  $\mu$ m. **(B)**: Linescan (derived from the dashed yellow line in **(A)**) showing normalized fluorescence intensity of DynPH-GFP, Lifeact-mApple, and the pillars.

regions of the interface. This was intriguing to us because previous studies had indicated that lytic granules accumulate beneath the more central IS domains (3, 11, 19, 20). To investigate the spatial relationship between synaptic protrusions and lytic granules, we imaged CTLs expressing Lifeact-mApple together with a GFP-labeled form of the lysosomal-associated membrane protein 1 (Lamp1-GFP). Lytic granules appeared as a cluster of distinct compartments within the CTL cytoplasm. In the first 2 min of contact formation, the granule cluster moved downward, settling around 5  $\mu$ m from the cell front, roughly at the level of

the pillar tops (Figure 2.4). This behavior implied a close association between granules and the centrosome, as previously reported (11, 20, 21).

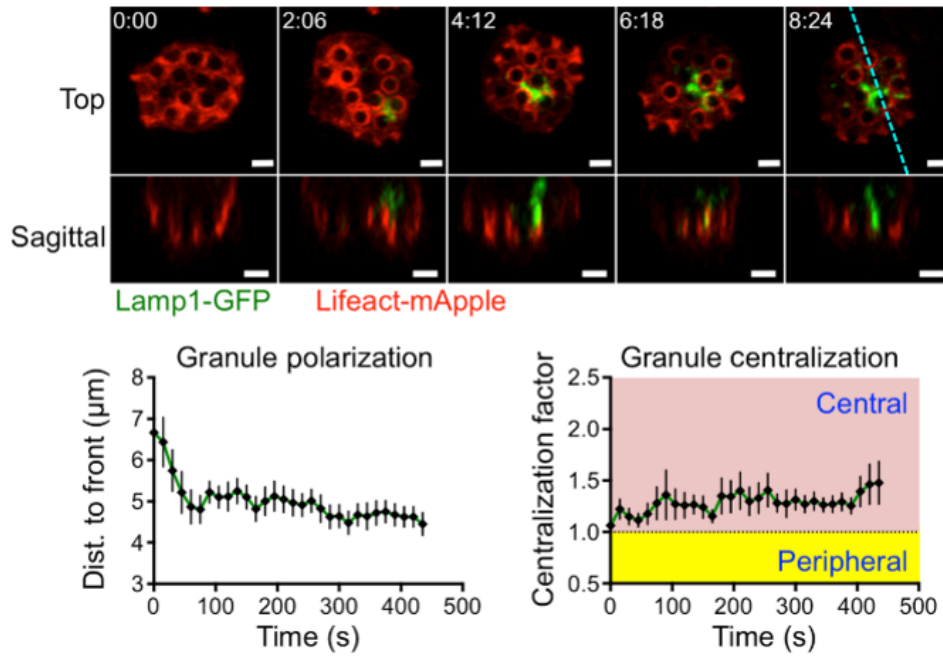


**Figure 2.4:** Granules polarize towards the center of the immune synapse.

Above, time-lapse montage of a representative CTL expressing Lifeact-mApple and Lamp1-GFP. Below left, mean distance between the lytic granule cloud and the cell front, graphed against time. Below right, centralization factor analysis of Lamp1-GFP. In both graphs, time 0 denotes initial contact with the pillars and error bars indicate SEM. n = 10.

After orienting downward, the granules tended to occupy central locations within the IS, which we quantified by calculating the normalized proximity of granule fluorescence to the IS center of gravity (COG) (Figure 2.5). Analysis of this “centralization factor” revealed that the granules tended to be closer to the center of the IS than would be expected by chance (Figure 2.4).

The proximity of lytic granules to the base of synaptic protrusions at the center of the IS raised the possibility that these structures might be involved in cytolytic mechanopotentiation. Synaptic protrusions were highly enriched in LFA1 (Figure

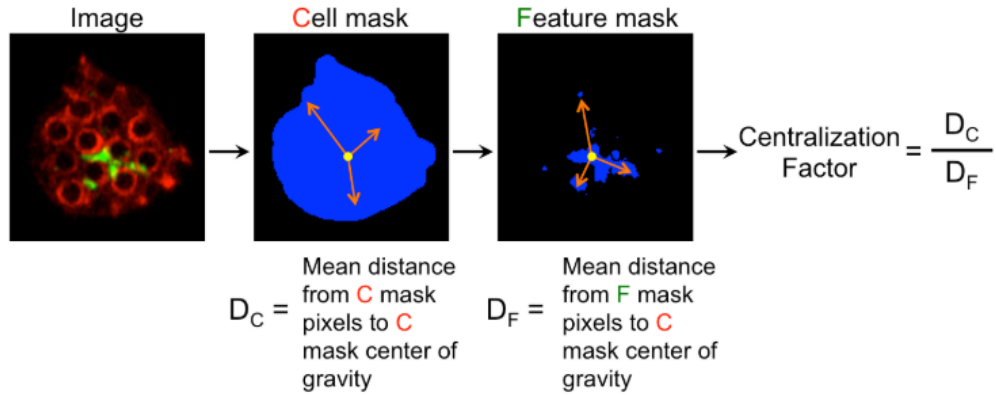


**Figure 2.5:** Centralization factor analysis.

The centralization factor compares the mean distance between a given feature within the IS (e.g. lytic granules) and the IS center of gravity ( $D_F$ ) to the mean distance between all positions within the IS and the IS center of gravity ( $D_C$ ).

2.2), consistent with them being strongly adhesive and capable of exerting force. Previously, we found that mechanopotentiation requires phosphoinositide 3-kinase (PI3K) signaling and is enhanced by the depletion of phosphatase and tensin homolog (PTEN) that antagonized PI3K. Short hairpin RNA (shRNA)-mediated suppression of PTEN augmented F-actin accumulation in synaptic protrusions (Figure 2.6), further supporting the idea that these structures transmit forces that promote cytotoxicity.

### 2.2.2 Granule fusion occurs at the base of synaptic protrusions

Granule fusion events can be detected in single-cell imaging experiments with a fluorescent reporter containing a pH-sensitive GFP (pHluorin) fused to the granule-targeting domain of Lamp-1 (22). Within lytic granules, the low pH environment quenches the fluorescence of pHluorin-Lamp1. Granule fusion with the plasma membrane, however, neutralizes the pH around the reporter,

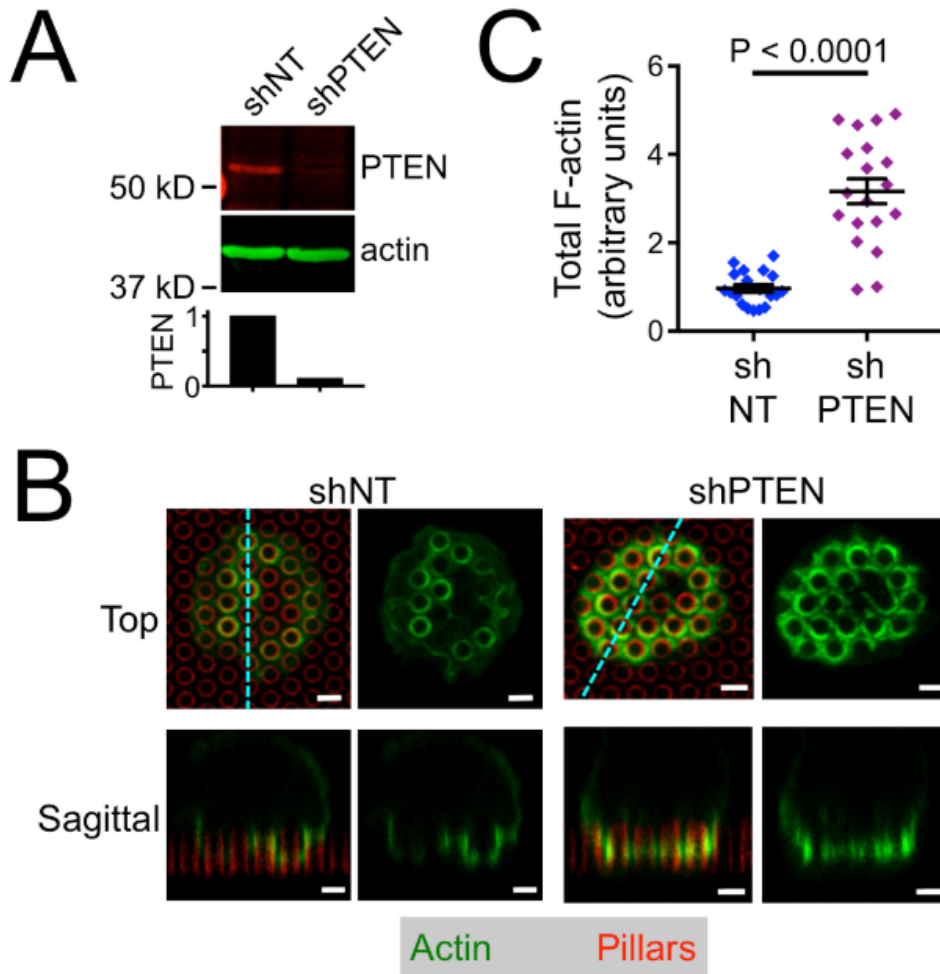


**Figure 2.6:** PTEN depletion enhances F-actin accumulation in protrusions.

OT1 CTLs expressing shRNA against PTEN (shPTEN) or a control nontargeting shRNA (shNT) were applied to fluorescent micropillars bearing H2-K<sup>b</sup>-OVA and ICAM1, fixed, and stained with phalloidin. **(A)**: Immunoblot analysis of PTEN expression in shNT and shPTEN CTLs. Actin served as a loading control. Bars denote intensity of PTEN bands. **(B)**: Representative images of shNT and shPTEN CTLs, with z-projection images (top views) shown above and sagittal views below. Cyan dashed lines denote the slicing planes used for the sagittal images. Scale bars = 2  $\mu$ m. **(C)**: Quantification of sum F-actin intensity on micropillar arrays. Error bars denote SEM. N = 19 for each cell type. P calculated from two-tailed Student's T-test.

leading to a rapid increase in fluorescence. To explore the relationship between cytolytic secretion and synaptic protrusions, we imaged OT1 CTLs expressing pHluorin-Lamp1 by confocal and lattice light-sheet microscopy on fluorescent micropillars coated with H2-K<sup>b</sup>-OVA and ICAM1I (Fig. 2A). Protrusions were visualized in these experiments either via Lifeact-mRuby2 or by staining with a fluorescent Fab against the surface marker CD45. After IS formation, fusion events appeared as sudden flashes of GFP fluorescence, which were often visible for only one time point. These events clustered close to the plane of the pillar tops (Fig. 2, B and C, and movie S2), the same vertical zone occupied by lytic granules and the centrosome. This position was well behind the leading edge of CTL protrusions, which extended about 5  $\mu\text{m}$  into the interpillar space.

Granule fusion was not observed in zones of sustained F-actin depletion. Instead, it tended to occur in regions containing synaptic protrusions (Fig. 2B and movie S2). To quantify this effect, we determined the Lifeact-mRuby2 intensity over time in the 1- $\mu\text{m}$ -diameter synaptic domain around each fusion site. F-actin accumulation within this domain actually increased modestly during granule fusion (Fig. 2D), implying that cytolytic secretion and protrusion growth could occur concurrently in the same region. Linescans of sagittal slice images demonstrated that F-actin did not overlap precisely with the fusion site. Instead, it tended to accumulate underneath it, closer to the bottoms of the pillars (Fig. 2E). We conclude that granule fusion on micropillar arrays occurs in small F-actin-free zones that form transiently at the base of active F-actin-rich protrusions.

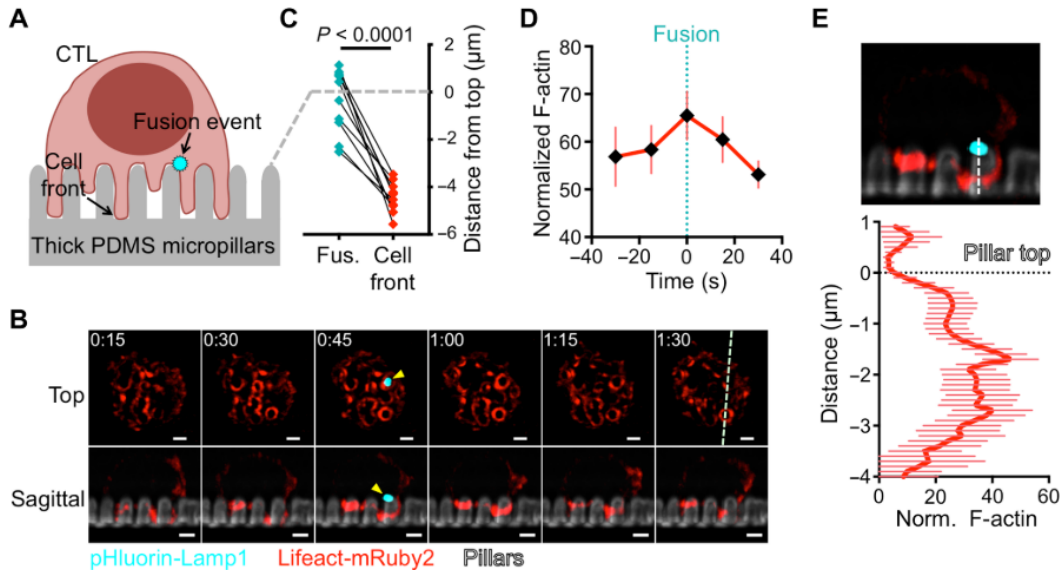


**Figure 2.7:** Granule fusion occurs at the base of synaptic protrusions.

**(A)**: Schematic diagram showing lytic granule fusion (visualized by pHluorin-Lamp1) on micropillar arrays. **(B to E)**: OT1 CTLs expressing pHluorin-Lamp1 were imaged by confocal (**C**) or lattice light-sheet (**B, D, and E**) microscopy on micropillars bearing H2-K<sup>b</sup>-OVA and ICAM1. **(B)**: Time-lapse montage of a representative CTL expressing Lifeact-mRuby2 and pHluorin-Lamp1, with micropillars shown in gray. z-projection images (top views) are shown above with sagittal views below. The white dashed line denotes the slicing plane used for the sagittal images. Yellow arrowheads indicate the fusion event. Time in minutes:seconds is indicated in the upper left corner of each top-view image. Scale bars, 2  $\mu$ m. **(C)**: Graph showing the vertical displacements of fusion events (Fus., cyan) relative to the plane of the pillar tops (dashed gray line) along with the corresponding position of the cell front (red, visualized with a fluorescent Fab fragment against CD45). n = 11 events. P values were calculated from two-tailed paired Student's t test. **(D)**: F-actin accumulation in the region of granule fusion in z-projection images of CTLs expressing Lifeact-mRuby2 and pHluorin-Lamp1. Graph shows the average Lifeact-mRuby2 intensity within a 1- $\mu$ m-diameter circle centered on the fusion site, starting two time points before the fusion event and ending two time points after. **(E)**: Below, mean normalized (Norm.) Lifeact-mRuby2 intensity derived from linescans vertically bisecting the midpoint of the granule fusion site. The dotted black line denotes the plane of the pillar tops. Above, a representative image used for the analysis, with the linescan region indicated by the dashed white line. Error bars in **(D)** and **(E)** denote SEM. n = 18 events.

### 2.2.3 WASP and WAVE2 control distinct subsets of protrusions

Having characterized the structure and dynamics of synaptic protrusions, we turned our attention to their molecular basis and biological function. Arp2/3 complex activity is controlled by regulators of the nucleation-promoting factor (NPF) family. Among NPFs, both WASP and WASP-verprolin homolog 2 (WAVE2) have been implicated in synaptic F-actin remodeling. WAVE2, which is activated by the guanosine triphosphate– bound form of the small guanosine triphosphatase (GTPase) Rac, is thought to promote cell spreading and adhesion during IS formation (8, 28–30). WASP, for its part, functions downstream of the GTPase Cdc42 and the adaptor protein Nck, and it has been linked to IS stability and the formation of protrusive structures during diapedesis and antigen scanning (31–34). In humans, loss-of-function WASP mutations cause WAS, a primary immunodeficiency associated with increased incidence of autoimmunity and cancer (35, 36).

To investigate the role of WASP and WAVE2 in the formation of synaptic protrusions, we imaged OT1 CTLs expressing GFP-labeled forms of each protein on stimulatory micropillars. WAVE2-GFP accumulated strongly in the periphery of the IS during initial cell spreading (<1 min; Figure 2.8). In subsequent time points, transient bursts of WAVE2-GFP appeared in isolated peripheral domains (Figure 2.8, magenta arrowheads), often occurring concomitantly with lateral movement of the IS toward the same side. By contrast, WASP-GFP accumulated in annular structures that encircled individual pillars in central and intermediate synaptic domains (Figure 2.8). WASP-GFP exhibited a significantly higher mean centralization factor than WAVE2-GFP at all time points (Figure 2.8), confirming that WASP localized more centrally than WAVE2.

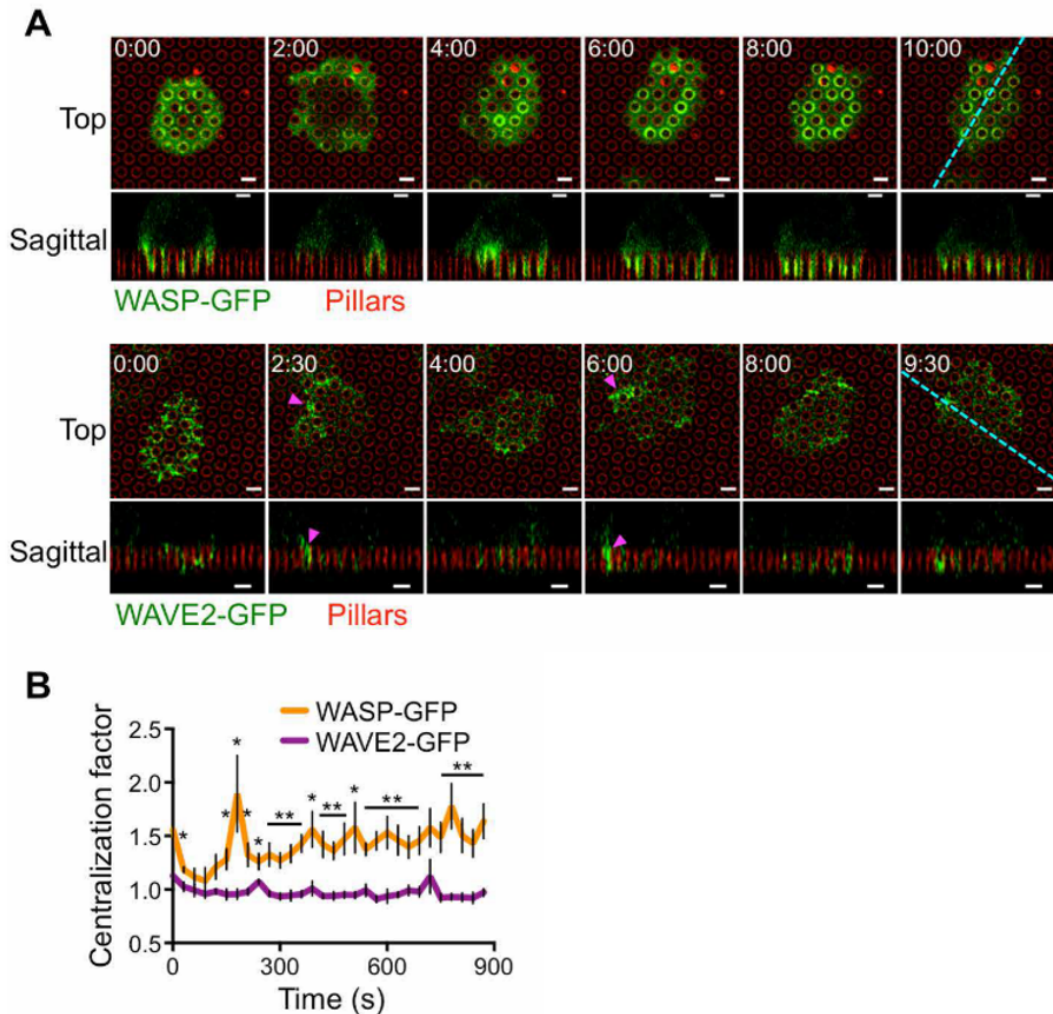


**Figure 2.8:** WASP and WAVE2 segregate at the synapse.

**(A and B):** OT1 CTLs expressing WASP-GFP or WAVE2-GFP were imaged by confocal microscopy on fluorescent micropillars bearing H2-K<sup>b</sup>-OVA and ICAM1. **(A):** Time-lapse montages of representative CTLs, with micropillars shown in red. z-projection images (top views) are shown above with sagittal views below. Cyan dashed lines denote the slicing planes used for the sagittal images. Magenta arrowheads indicate representative lateral accumulations of WAVE2-GFP. **(B):** Centralization factor analysis of WASP-GFP and WAVE2-GFP, with time 0 denoting initial contact with the pillars. n = 6 for each cell type. In graphs, \*P < 0.05 and \*\*P < 0.01, calculated by two-tailed Student's t test comparing WASP-GFP to WAVE2-GFP **(B)**. Error bars denote SEM.

To assess the importance of WASP and WAVE2 for IS re-modeling, we used CRISPR (CR)-Cas9 to target the *Was* and *Wasf2* genes, respectively, in OT1 CTLs (Figure ??). WASP- or WAVE2-deficient CTLs prepared in this manner (WASP-CR and WAVE2-CR, respectively) were transduced with Lifeact-GFP and then imaged on micropillar arrays. Whereas control CTLs expressing nontargeting guide RNA (NT-CR) formed protrusions in both the center and the periphery of the IS, the protrusive activity of WASP-CR cells was largely constrained to the periphery (Figure 2.9). Centralization factor analysis revealed that the F-actin distributions of WAVE2-CR CTLs were more centralized than those of NT-CR controls, which were in turn more centralized than those of WASP-CR CTLs (Figure 2.9). Hence, WASP deficiency leads to a specific loss of central protrusions, whereas WAVE2 deficiency eliminates peripheral structures. Collectively, these data indicate that WAVE2 controls peripheral F-actin growth involved in lateral motion, whereas WASP drives protrusion formation closer to the center of the IS.

#### **2.2.4 WASP and WAVE2 depletion induce distinct functional phenotypes**

Next, we investigated the mechanical consequences of WASP and WAVE2 depletion by imaging NT-CR, WASP-CR, and WAVE2-CR CTLs on narrow micropillar arrays (Figure 2.1). WASP-CR CTLs avidly engaged the arrays and deformed them as quickly as did NT-CR controls. The overall magnitude of WASP-CR force exertion, however, was significantly reduced (Figure 2.10). By contrast, depletion of WAVE2 delayed the onset of force exertion but did not affect its overall magnitude (Figure 2.10). To assess the spatial patterns of these

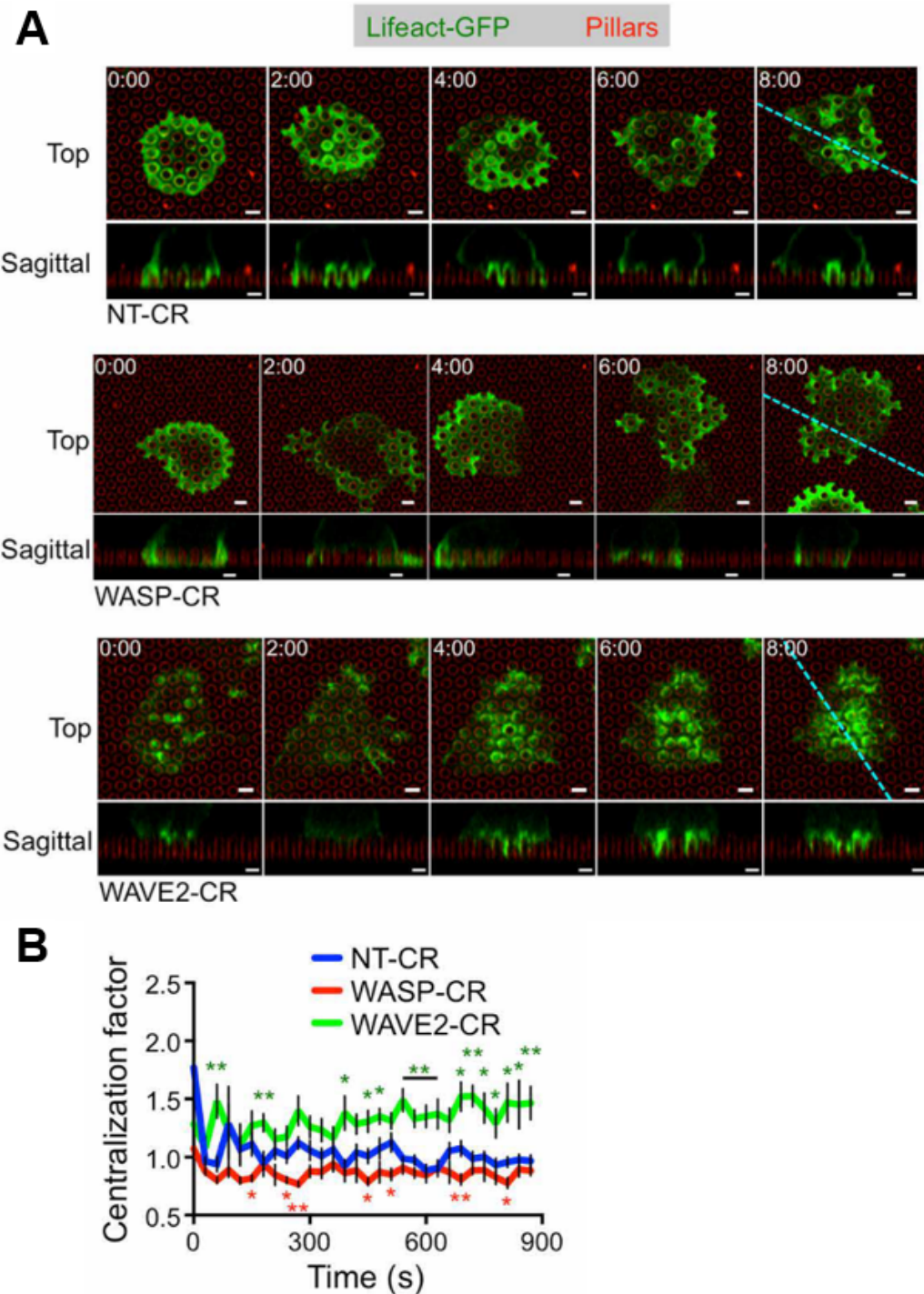


**Figure 2.9:** WASP and WAVE2 control distinct subsets of protrusions.

(A: Time-lapse montages of representative CTLs, with micropillars shown in red. z-projection images (top views) are shown above with sagittal views below. Cyan dashed lines denote the slicing planes used for the sagittal images. (B): Centralization factor analysis of Lifeact-GFP in NT-CR, WASP-CR, and WAVE2-CR OT1 CTLs, with time 0 denoting initial contact with the pillars. n = 6 for each cell type. In all montages, time in minutes:seconds is indicated in the upper left corner of each top-view image. Scale bars, 2  $\mu$ m. In graphs, \*P < 0.05 and \*\*P < 0.01, calculated by two-tailed Student's t test WASP-CR (red) and WAVE2-CR (green) to NT-CR (B). Error bars denote SEM.

mechanical responses, we plotted the number of strongly deflected pillars as a function of radial distance from the IS COG (Figure 2.12). NT-CR and WAVE2-CR CTLs induced pillar deflections in both the central IS ( $< 3 \mu\text{m}$  from the COG) and the periphery ( $> 3 \mu\text{m}$  from the COG). By contrast, in WASP-CR CTLs, there was a marked absence of centrally localized events (Figure 2.11). Hence, the capacity to generate protrusions in the center of the IS was associated with force exertion in that domain.

Last, we examined the cytotoxic function of CTLs lacking WASP and WAVE2. WASP depletion induced a significant defect in killing, which we observed using both lymphocytic (RMA-s lymphoma) and adherent (MB49 urothelial carcinoma, B16 melanoma) target cells (Figure 2.11). This defect was most pronounced (around a 50% reduction) at low levels of antigen. At higher antigen concentrations, however, killing by NT-CR and WASP-CR CTLs was quite comparable. WASP-CR CTLs did not exhibit lower levels of lytic granule fusion (Figure 2.11), indicating that their reduced cytotoxicity could not be attributed to a defect in perforin and granzyme release. Depletion of WAVE2 led to a distinct and somewhat variable cytotoxicity phenotype. In some experiments, we found little to no change in killing and granule fusion, whereas in others, we observed modest reductions that were most pronounced at high antigen concentrations (Figure 2.11 and 2.12). WAVE2-CR CTLs, but not their WASP-CR counterparts, exhibited significantly reduced conjugate formation (Figure 2.11), implying that WAVE2 promotes target cell adhesion. Consistent with this interpretation, depletion of WAVE2, but not WASP, impaired CTL adhesion to ICAM1-coated surfaces, both in the presence and in the absence of H2-K<sup>b</sup>-OVA (Figure 2.12). We also examined indices of TCR signaling and found that WASP-CR and WAVE2-CR CTLs exhibited normal TCR-induced  $\text{Ca}^{2+}$  flux and activation of the MAPK,

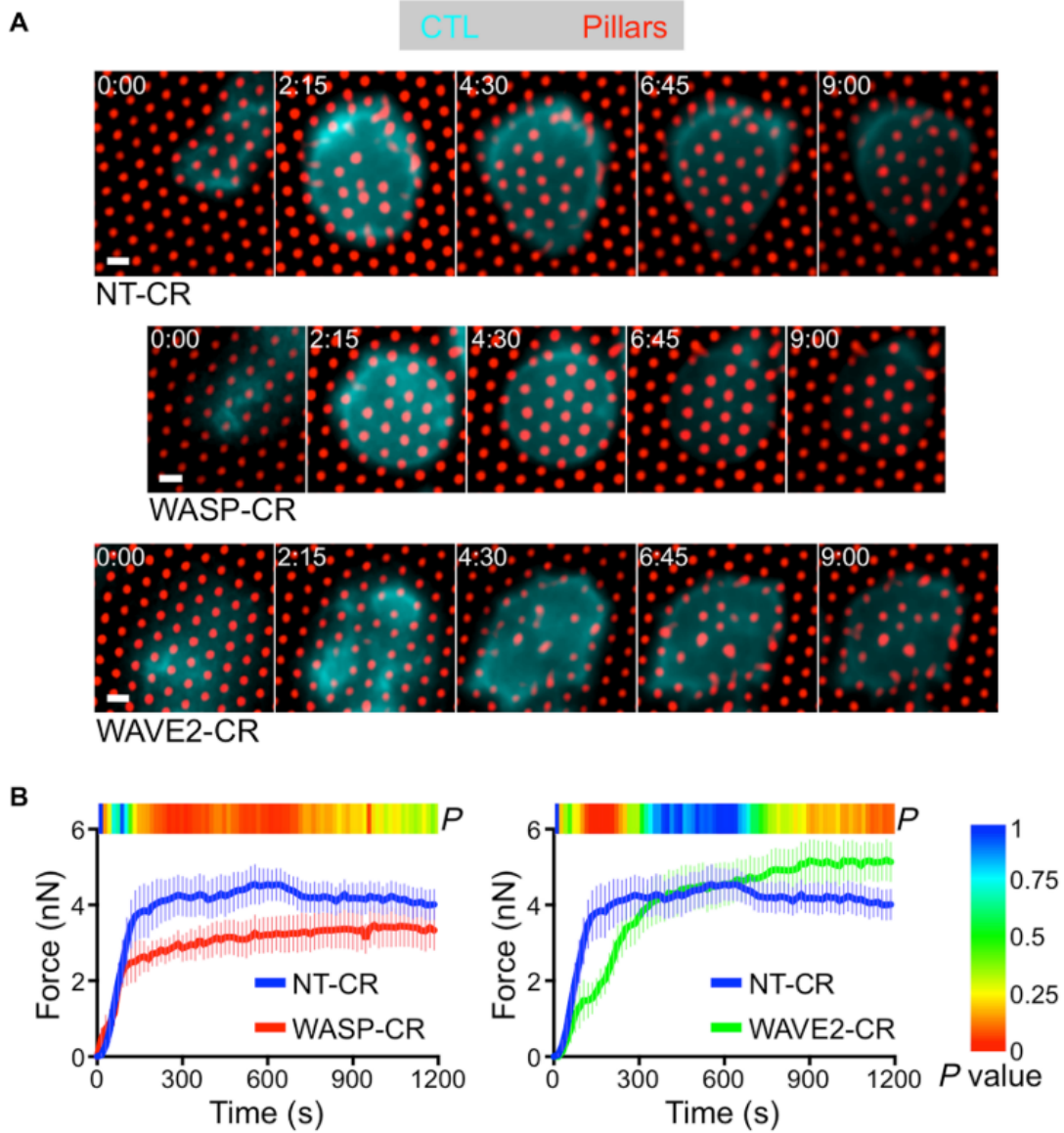


**Figure 2.10:** WASP and WAVE2 depletion induces spatially different patterns of force exertion.

**(A and B):** NT-CR, WASP-CR, and WAVE2-CR OT1 CTLs were labeled with a fluorescent anti-CD45 Fab and imaged on narrow fluorescent micropillars coated with H2-K<sup>b</sup>-OVA and ICAM1. **(A):** Time-lapse montages of representative CTLs showing pillar deflection. Time in minutes:seconds is indicated in the upper left corner of each top-view image. Scale bars, 2  $\mu$ m. **(B):** Total force exertion against pillar arrays was graphed versus time. Color bar above each graph indicates the P value for each time point (two-tailed Student's t test).

PI3K, and NF- $\kappa$ B pathways (Figure 2.12). Hence, depletion of WASP or WAVE2 does not broadly disrupt early T cell activation.

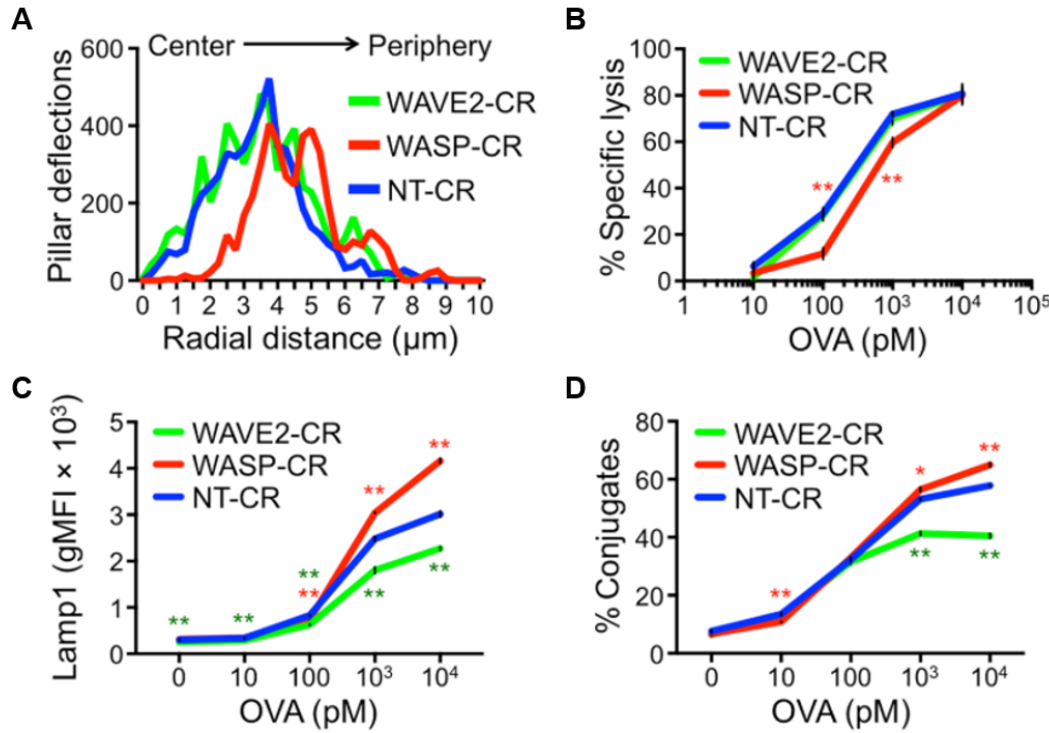


**Figure 2.11:** WASP and WAVE2 depletion induce distinct functional phenotypes.

(A): Histogram showing the distribution of strong deflections as a function of radial distance from the center of the IS. n = 10 for each cell type in Figure 2.10. (A to D): RMA-s target cells were loaded with increasing concentrations of OVA and mixed with NT-CR, WASP-CR, or WAVE2-CR OT1 CTLs. (B): Specific lysis of RMA-s cells. (C): Lytic granule fusion measured by surface exposure of Lamp1. (D): CTL-target cell conjugate formation measured by flow cytometry. All error bars denote SEM. In (A to D), \*P < 0.05 and \*\*P < 0.01, calculated by two-tailed Student's t test comparing WASP-CR (red) and WAVE2-CR (green) to NT-CR.

We conclude that WASP plays a more important role than WAVE2 in boosting cytotoxicity and that it does so in a manner independent of TCR signaling, conjugate formation, and granule release. The WASP-CR killing defect was strongest at low antigen concentrations, when granule release was lower and perforin levels were limiting, and it disappeared at high antigen concentrations, when perforin was abundant. Previous studies of CTLs derived from patients

with WAS revealed a similar cytotoxicity phenotype: reduced killing (despite normal conjugate formation and granule release), which was rescued by strong TCR stimulation (33, 37). This is precisely the pattern of results one would expect after blocking a mechanical process that boosts the per-molecule efficiency of perforin. Together with the imaging data described above, these results suggest a model in which centralized, WASP-dependent protrusions enhance target cell killing through cytolytic mechanopotentiation.

### 2.2.5 WASP controls target cell deformation at the IS

If synaptic protrusions mechanopotentiate perforin function, then they should be capable of physically deforming the target cell surface. To investigate this hypothesis, we performed live imaging experiments using H2-K<sup>b</sup> murine endothelial cells as targets for OT1 CTLs (13, 31). In culture, endothelial cells adopt a flat, stellate architecture that is stable over time. Hence, deviations in this morphology within the IS can be attributed to the physical activity of the T cell (Figure 2.13). To facilitate imaging of cellular volume, we prepared endothelial cell lines that expressed mApple or infrared fluorescent protein 670 nm (iRFP670) uniformly in both the cytoplasm and the nucleus. These target cells were loaded with OVA, mixed with OT1 CTLs expressing fluorescently labeled Lifeact, and imaged by lattice light-sheet microscopy. Synapses formed readily and could be identified by their stability, as well as the strong accumulation of interfacial F-actin within the CTL. Within minutes of IS initiation, CTLs generated small, protrusive F-actin structures that invaded the space occupied by the target cell (Figure 2.13, yellow arrowheads). This was followed shortly thereafter by rapid displacement of the target surface, which was most obvious in conjugates where

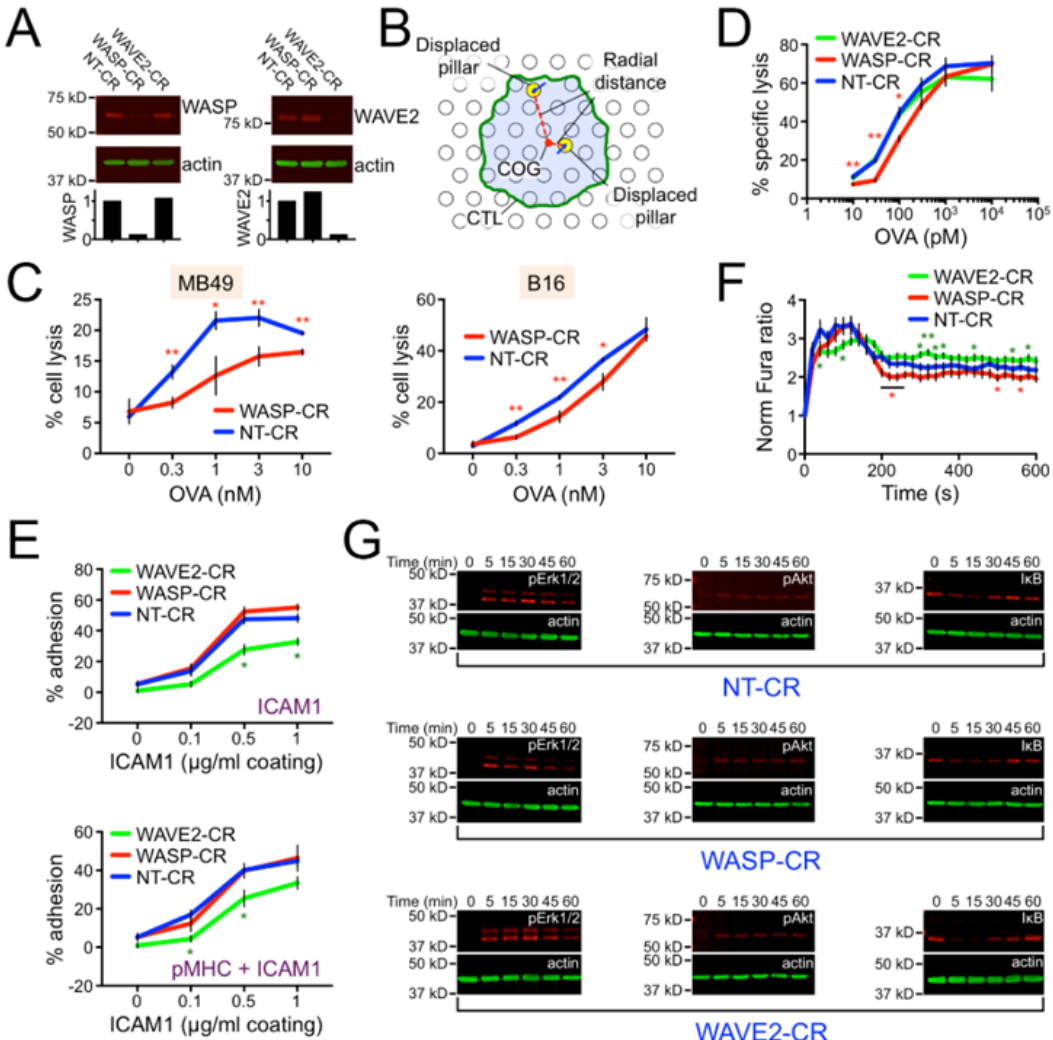


**Figure 2.12:** WASP and WAVE2 depletion induce distinct functional phenotypes.

(A): Immunoblot analysis of WASP and WAVE2 expression in NT-CR, WASP-CR, and WAVE2-CR CTLs. Actin served as a loading control. Bars denote intensity of WASP and WAVE2 bands. (B): Diagram schematizing the radial distance histogram analysis of pillar deflections shown in Figure 2.10. (C): Adherent MB49 (left) or B16 (right) cells were loaded with increasing concentrations of OVA and then mixed with NT-CR or WASP-CR OT1 CTLs. Target cell lysis was measured by LDH release. (D): RMA-s target cells were loaded with increasing concentrations of OVA and then mixed with NT-CR, WASP-CR, or WAVE2-CR OT1 CTLs. Specific lysis of RMA-s cells is shown. This experiment highlights the reduced cytotoxicity occasionally observed in WAVE2-CR CTLs at high antigen concentrations. (E): Adhesion of fluorescently labeled NT-CR, WASP-CR, and WAVE2-CR OT1 CTLs to wells coated with the indicated concentrations of ICAM1 in the absence (top) or presence (bottom) of H2-K<sup>b</sup>-OVA (pMHC). (F): NT-CR, WASP-CR, and WAVE2-CR OT1 CTLs were loaded with Fura2-AM  $Ca^{2+}$  dye and then imaged on stimulatory glass surfaces coated with H2-K<sup>b</sup>-OVA and ICAM1.  $Ca^{2+}$  signaling was analyzed by quantifying mean normalized Fura2 ratio over time. N ≥ 29 for each cell type. In (C-F), \* and \*\* indicate P < 0.05 and P < 0.01, respectively, calculated by two-tailed Student's T-test comparing WASP-CR (red) and WAVE2-CR (green) to NT-CR. (G): NT-CR, WASP-CR, and WAVE2-CR OT1 CTLs were stimulated with beads coated with H2-K<sup>b</sup>-OVA and ICAM1 for the indicated times and then lysed. pErk1/2, pAkt, and I $\kappa$ B levels were assessed by immunoblot using actin as a loading control. All error bars denote SEM.

the CTL attacked from above (Figure 2.13). This displacement typically occurred before any obvious signs of target cell blebbing, suggesting that it was not part of the apoptotic cascade. CTLs lacking perforin also formed large holes in target cells (Figure 2.14), further supporting the idea that synaptic deformations result from a physical, rather than a chemical, process. TCR engagement was critical for these mechanical effects. In the absence of antigen, both the speed and the magnitude of target cell displacement diminished substantially (Figure ??), consistent with previous work (13). Last, imaging of CTLs expressing Lamp1-GFP revealed that lytic granules accumulated close to areas of deformation (Figure 2.14), implying that physical manipulation of the target cell contributes to perforin- and granzyme-mediated killing.

Next, we investigated the molecular basis of target cell displacement by comparing synapses formed by NT-CR, WASP-CR, and WAVE2-CR CTLs. Depletion of WASP markedly inhibited physical deformation of the target surface, despite the fact that robust synaptic F-actin accumulation still occurred (Figure 2.13). To quantify this result, we determined the volume beneath the CTL occupied by the target cell at a given time point and normalized this value to the volume occupied by the target cell in that same region before IS formation (Figure 2.15). Analysis of this “target IS volume” parameter confirmed that WASP depletion significantly reduced the target cell displacement response (Figure 2.13). CTLs lacking WAVE2 exhibited a qualitatively distinct phenotype; although they were still capable of substantial deformation, their mechanical responses were somewhat delayed relative to those of NT-CR controls (Figure 2.13). Collectively, these results mirror the force exertion analysis of WASP-CR and WAVE2-CR CTLs (Fig. 6, A to C), and they suggest that WASP-dependent synaptic protrusions play a particularly important role in the physical deformation of target cells.

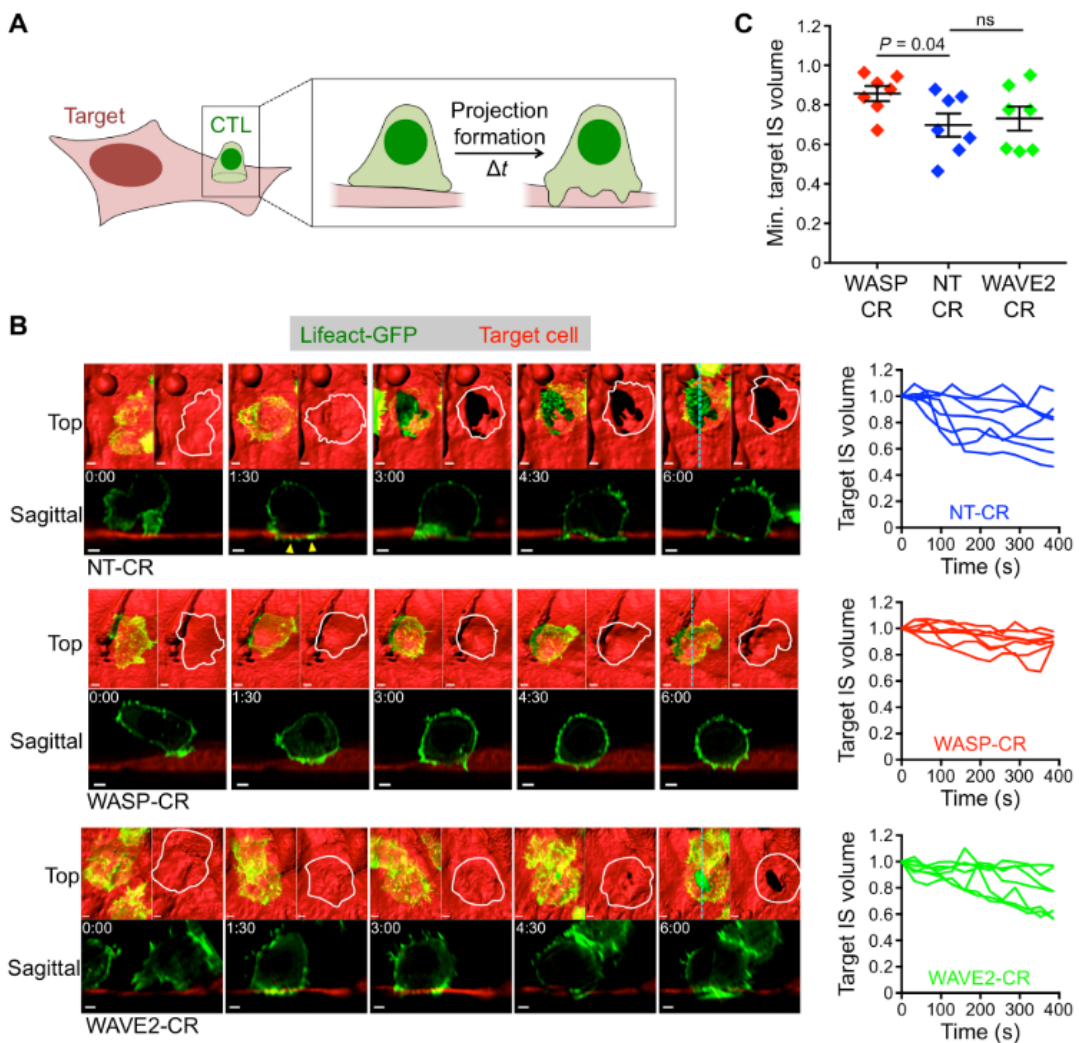


**Figure 2.13:** WASP controls target cell deformation at the IS.

**(A):** Schematic diagram of a CTL deforming an adherent target cell. **(B and C)** NT-CR, WASP-CR, and WAVE2-CR OT1 CTLs expressing Lifeact-GFP were applied to cultures of OVA-loaded endothelial target cells expressing iRFP670 and imaged using lattice light-sheet microscopy. **(B):** Left: Time-lapse montages of representative “vertically” oriented synapses, with z-projection images (top views) shown above and sagittal views below. Cyan dashed lines denote the slicing planes used for the sagittal images. In z-projection images, target cells are visualized by surface representation. Two z-projections are shown for each time point; Lifeact-GFP is shown on the left and the outline of the CTL of interest is shown on the right. Time in minutes:seconds is indicated in the upper left corner of each sagittal image. Scale bars, 2  $\mu$ m. Yellow arrowheads denote protrusive structures in the NT-CR CTL that invade the target cell space. Right: Target IS volume graphed against time, with time 0 denoting IS initiation. Each line corresponds to one CTL-target cell conjugate. **(C):** Graph of minimum target IS volume values achieved during the first 400 s of conjugate formation. n = 7 for each cell type. Error bars denote SEM. P value was calculated by two-tailed Student’s t test.

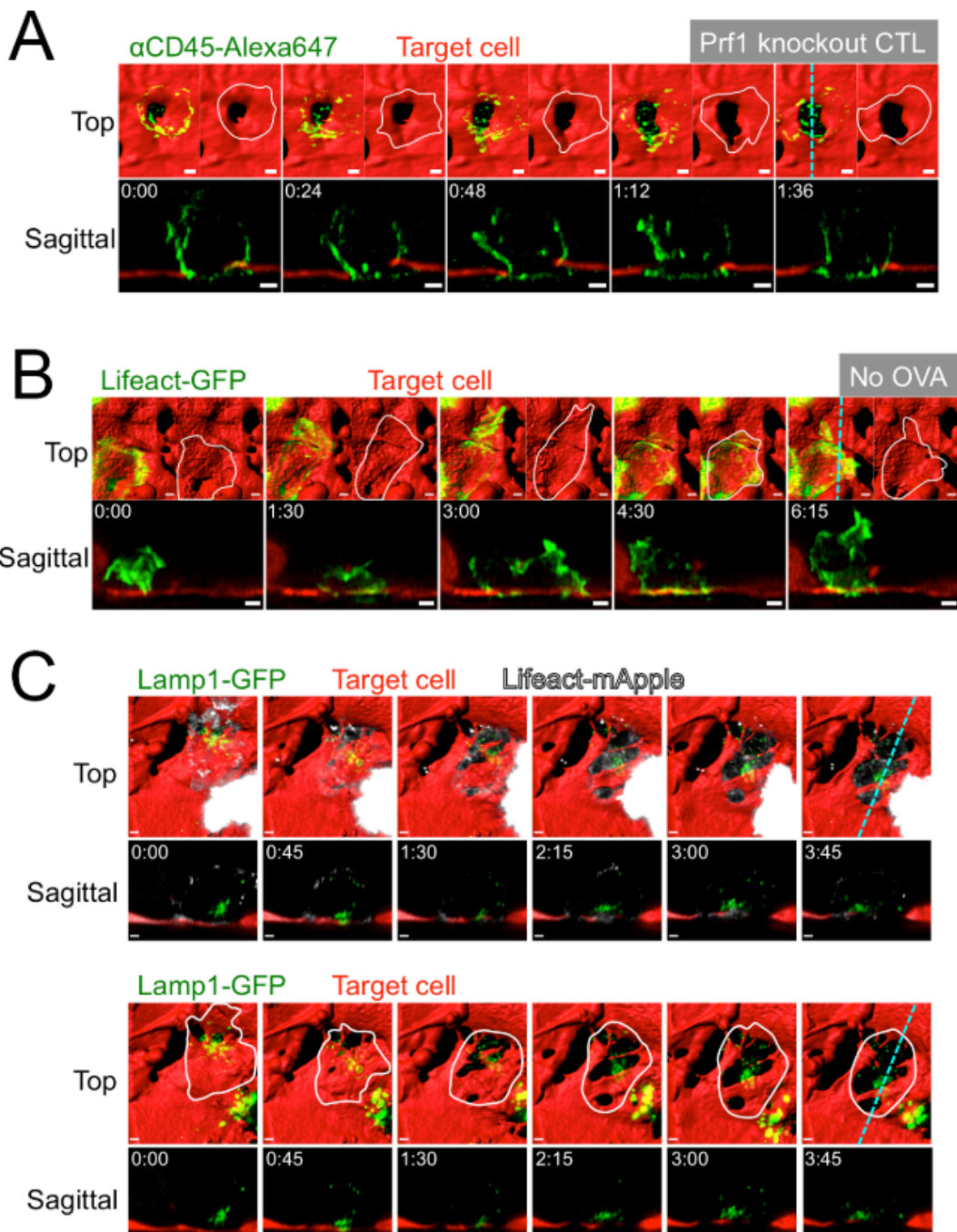


**Figure 2.14:** CTLs physically manipulate the target cell surface.

(A-C): OT1 CTLs were applied to OVA-loaded endothelial target cells expressing mApple (**A**) or iRFP670 (**B and C**) and then imaged using lattice light-sheet microscopy. All time-lapse montages show “vertically” oriented synapses, with z-projection images (top views) shown above and sagittal views below. Target cells are visualized by surface representation in all z- projection images. Cyan dashed lines denote the slicing planes used for the sagittal images. Time in M:SS is indicated in the upper left corner of each sagittal image. Scale bars = 2  $\mu$ m. (**A**) A representative Prf1<sup>-/-</sup> CTL, visualized using fluorescent Fab fragments against CD45, engaging a target cell. (**B**): A representative CTL expressing Lifeact-GFP engaging a target cell in the absence of OVA. In A and B, two z-projections are shown for each time point; the fluorescent signal from the CTL appears on the left and is replaced with an outline of the CTL of interest on the right. (**C**): A representative CTL expressing Lifeact-mApple and Lamp1-GFP, engaging a target

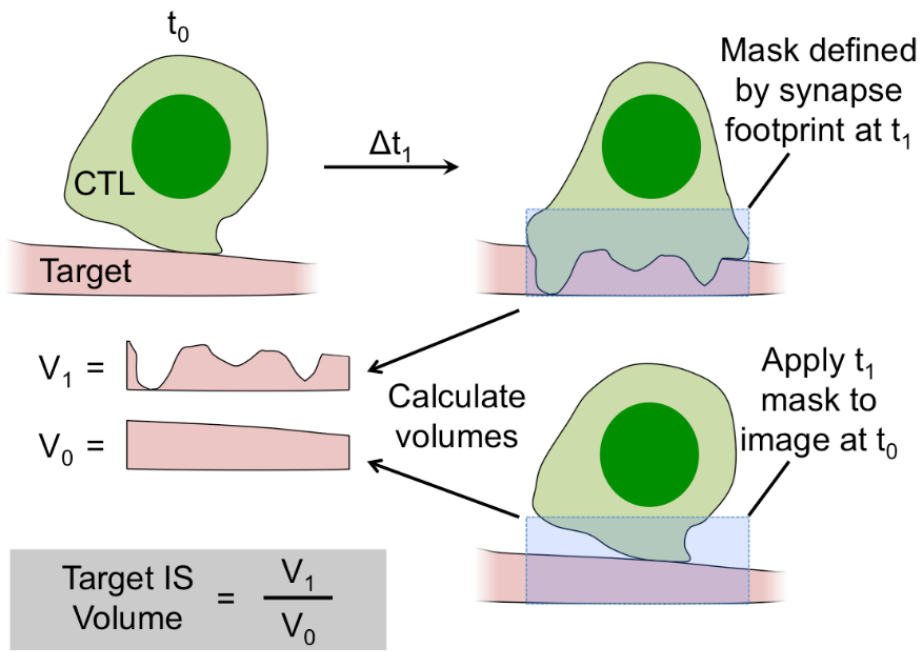


**Figure 2.15:** Target volume analysis.

Target IS volume compares the endothelial cell volume in the region beneath a CTL at a given time ( $V_1$ ) with the volume occupied by the endothelial cell in that same region at time 0 ( $V_0$ ).

## 2.3 Discussion

The cytotoxic IS boosts perforin toxicity by spatially coordinating its secretion with the exertion of mechanical force. In the present study, we found that perforin release occurs at the base of WASP-dependent, F-actin-rich protrusions (Figure 2.16). These protrusions were necessary for synaptic force exertion, particularly in more central regions of the IS close to lytic granules. They were also required for physical deformation of target cells in bona fide cytolytic interactions. WASP-deficient CTLs exhibited a defect in killing that could not be explained by reduced granule release or conjugate formation. Together, these data identify synaptic protrusions as key components of a physical delivery system that enables CTLs

to kill target cells with high efficiency. In putting forth this model, we do not suggest that synaptic protrusions are a prerequisite for lytic granule release. Indeed, multiple groups have demonstrated that rigid stimulatory surfaces induce robust cytolytic secretion in the absence of protrusive activity (19, 22, 38–40). However, the converse relationship may be worth considering, namely, that lytic granule docking and fusion might influence local F-actin architecture and IS mechanics.

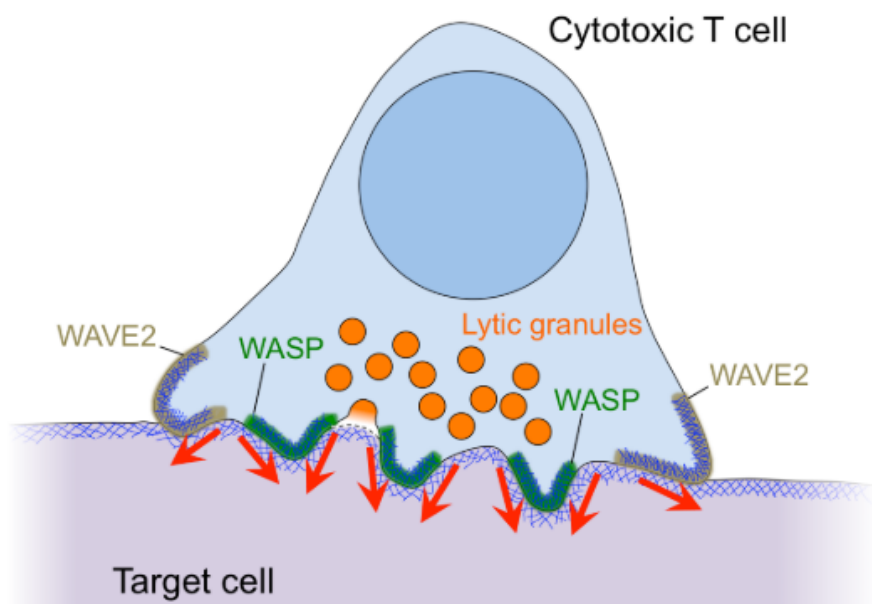


**Figure 2.16:** Cytolytic mechanopotentiation by WASP-dependent synaptic protrusions. Diagram of the cytolytic IS showing peripheral WAVE2-dependent protrusions and central WASP-dependent protrusions. Red arrows denote force exertion.

The marked concentration of granule fusion events at the base of synaptic protrusions implies that mechanisms exist for granule targeting to these domains. Previous studies have highlighted the importance of F-actin clearance for enabling granule access to the plasma membrane (11, 12, 22, 40). This is consistent with our observation that, on micropillar arrays, granule fusion occurs

in transient F-actin–free regions at the base of synaptic protrusions. However, the presence of other F-actin hypodense areas in the CTL, which are not targeted by granules, implies that other factors contribute to the process. Lipid second messengers are known to influence exocytosis and membrane trafficking in a variety of cellular contexts (41). Among these, diacylglycerol is an interesting candidate because it tends to accumulate in central synaptic domains that experience F-actin depletion (42–44). Granule delivery via microtubules is another possibility (45, 46). We observed that a small subset of microtubules extends into synaptic protrusions, and it will be interesting to explore whether and how this subset contributes to granule trafficking from the centrosome toward fusion sites in the synaptic membrane. Last, it is possible that WASP itself plays a role. A recent super-resolution imaging study demonstrated that WASP promotes granule docking close to regions of integrin clustering (47). T cells form a variety of protrusive structures at both interfacial and noninterfacial surfaces, which have been documented previously by electron microscopy and high-resolution fluorescence imaging (13, 14, 20, 34, 48, 49). Although the spatial distribution of these protrusions and their dynamics have implied roles in antigen scanning, signaling, and motility, their precise functions have, in most cases, remained undefined. Probably the best-studied are the invadosome-like protrusions (ILPs), which were first observed in T cells initiating diapedesis through endothelial monolayers (34). Subsequently, ILPs were also found in antigen-induced synapses formed between T cells and endothelial cells, dendritic cells, or B cells (13). ILPs are podosomal structures that are enriched in LFA1 and require WASP and Arp2/3 for their formation (31, 34). The synaptic protrusions we have observed share these characteristics, and it is therefore tempting to speculate that they are a form of ILP. That CTLs might use the same structures to facilitate both diapedesis and

target cell killing highlights an underappreciated similarity between the two processes. Both rely on the physical deformation of other cells through direct contact, in the first case to facilitate transmigration and in the second to promote destruction.

The functional defects observed in T cells from patients with WAS and Wasp<sup>-/-</sup> mice have been attributed to specific effects of WASP on TCR signaling (31, 33, 50-52). WASP is expressed by all lymphoid and myeloid lineages (35, 36), however, and consequently, the phenotypes exhibited by any one immune subset in a WASP-deficient background result not only from the cell-intrinsic functions of the protein but also from the dysfunction of other cell types. Interpreting studies from patient samples is particularly complex because of the wide range of pathological WASP mutations, which vary in their penetrance and can therefore yield markedly distinct disease phenotypes (36). In the present study, we circumvented this complexity by selectively deleting Wasp in CTLs using CRISPR-Cas9 targeting. The resulting cytotoxicity defect was not associated with reduced TCR signaling,  $Ca^{2+}$  flux, or granule release, but rather was caused by a failure to generate interfacial protrusions during the effector phase of the response. These data raise the possibility that WASP-dependent protrusions may contribute to interfacial effector pathways in other immune subsets. Previous studies have implicated WASP in macrophage phagocytosis (53, 54), T cell priming by dendritic cells (55, 56), and the induction of B cell class switching by follicular T helper cells (57). It will be interesting to investigate how the protrusive activity of WASP influences these and other cell-cell interactions and, in turn, how defects in these interactions contribute to the complex etiology of WAS. In marked contrast to WASP, WAVE2 accumulated in peripheral synaptic protrusions, and CTLs lacking WAVE2 exhibited adhesion and conjugation defects. These observations

suggest a role in cell spreading and adhesion that is consistent with previous reports (28–30). WAVE2 depletion only weakly affected synaptic force exertion and killing, indicating that the protein and the peripheral structures it generates are not involved in cytolytic mechanopotentiation. These results do not exclude the possibility that WAVE2 might promote cytotoxicity in other settings, particularly when target cells are more limiting and robust migration and adhesion are required for their destruction. What is clear from our data, however, is that the functionality of synaptic protrusions is partitioned both spatially (center versus periphery) and molecularly (WASP versus WAVE2). In vitro systems that collapse the IS into two dimensions have been invaluable for investigating its structure and function (58, 59). The inherent constraints of these systems, however, have limited our understanding in significant ways. It was only by analyzing the IS in an oriented, three-dimensional environment that we were able to assess the formation of synaptic protrusions and to study the implications of these structures for IS mechanics and effector responses. Micropatterned reconstitution systems can reveal unexplored aspects of cellular architecture, and we anticipate that they will become increasingly important in future studies of complex immune cell biology.

## 2.4 Materials and Methods

### 2.4.1 Study design

The goal of this study was to understand how CTLs combine cytolytic secretion with force exertion at the IS. We used fluorescence imaging of mouse

CTLs, single-cell biophysical assays, and functional experiments. Micropatterned PDMS substrates were used both to visualize the growth of synaptic protrusions and to measure mechanical activity. To perturb protrusion formation and synaptic F-actin dynamics, we used CRISPR-Cas9 technology, shRNA, and the Arp2/3 inhibitor CK666. Experimental sample sizes were not pre-determined, and there were no predefined study end points. Experiments were not randomized, and investigators were not blinded during acquisition and data analysis. In general, experiments were performed at least twice (two biological replicates). Specific information about analysis methods can be found in the “Image analysis” section below.

#### 2.4.2 Micropillar preparation

PDMS (Sylgard 184; Dow Corning) micropillar arrays were prepared as previously described (17). Two types of pillars were used for this study: (i) 1  $\mu\text{m}$  in diameter, 5  $\mu\text{m}$  in height, and spaced hexagonally with a 2  $\mu\text{m}$  center-to-center distance; and (ii) 0.7  $\mu\text{m}$  in diameter, 6  $\mu\text{m}$  in height, and spaced hexagonally with a 2- $\mu\text{m}$  center-to-center distance. Micropillars were cast on chambered coverglass (Lab-Tek), washed with ethanol and phosphate-buffered saline (PBS), and stained with fluorescently labeled streptavidin (20  $\mu\text{g}/\text{ml}$ ) (Alexa Fluor 647 or Alexa Fluor 568, Thermo Fisher Scientific) for 2 hours at room temperature. After additional washing in PBS, the arrays were incubated with biotinylated H2-K<sup>b</sup>-OVA and ICAM1 (10  $\mu\text{g}/\text{ml}$  each) overnight at 4°C (8). The pillars were then washed into RPMI containing 5% (v/v) fetal calf serum (FCS) and lacking phenol red for imaging.

### **2.4.3 Live imaging on micropillars**

For force measurements, T cells were stained with Alexa Fluor 488–labeled anti-CD45.2 Fab (clone 104-2) and imaged on fluorescently labeled 0.7- $\mu\text{m}$ -diameter pillars. Videomicroscopy was performed using an inverted fluorescence microscope (Olympus IX-81) fitted with a 100x objective lens and a mercury lamp for excitation. Images in the 488-nm (CTLs) and 568-nm (pillars) channels were collected every 15 s using MetaMorph software. Protrusion formation was imaged on 1- $\mu\text{m}$ -diameter pillars stained with Alexa Fluor 647-labeled or Alexa Fluor 568-labeled streptavidin. Cells expressing fluorescent probes were added to the arrays and imaged using a confocal laser scanning microscope fitted with a 40x objective lens and 488-nm, 560-nm, and 642-nm lasers (Leica SP5 or Zeiss LSM 880).

### **2.4.4 Lattice light-sheet imaging**

Lattice light-sheet microscopy was performed as previously described using 488-nm, 560-nm, and 642-nm lasers for illumination and a 25x water immersion objective (60). Micropillar arrays were cast on 5-mm-diameter coverslips, which were coated with stimulatory proteins as described above and then mounted for imaging. Movies (3- to 20-s time-lapse intervals) were recorded immediately after addition of fluorescently labeled CTLs using two cameras. We collected 488-nm (30–60 mW laser power) and 560-nm (50 mW laser power) images on one camera and 642-nm (50 mW laser power) images on a second camera. For CTL-target cell imaging, CTLs were added to coverslips bearing 90% confluent monolayers of mApple- or iRFP670-labeled endothelial cells that had been in-

cubated overnight in 2- $\mu$ M OVA. Movies (15- to 20-s time-lapse intervals) were recorded immediately after addition of CTLs. We collected 488-nm (50 mW laser power), 560-nm (200 mW laser power), and 642-nm (200 mW laser power) images on one camera. Raw data were deskewed and deconvolved as previously described (60) using experimentally derived point spread functions. For two camera experiments, image alignment was performed in MATLAB using reference images of fluorescent beads.

#### 2.4.5 Image analysis

Imaging data were analyzed using SlideBook (3i), Imaris (Bitplane), Excel (Microsoft), Prism (GraphPad), and MATLAB (MathWorks).  $Ca^{2+}$  responses were quantified by first normalizing the ratiometric Fura2 response of each cell to the last time point before the initial influx of  $Ca^{2+}$  and then by aligning and averaging all responses in the dataset based on this initial time point. To quantify F-actin intensity in fixed images (fig. S3C), we determined the sum intensity of Alexa Fluor 546–labeled phalloidin in the region beneath the pillar tops for each cell after intensity thresholding. For protrusion enrichment (Fig. 3C), total Lifeact-GFP intensity in the region beneath the pillar tops was divided by the total Lifeact-GFP intensity in a region of identical volume beginning from the first z-section above the pillar tops and extending upward (fig. S4A). Force exertion against 0.7  $\mu$ m-diameter pillars was calculated after extracting pillar displacements from the imaging data and then converting these displacements into force vectors using custom MATLAB scripts (17, 18). Radial distributions of pillar deflections (Fig. 6C) were generated by calculating the distances between strongly deflected pillars ( $\geq 0.6 \mu$ m deflection) and the IS COG at each time point

(fig. S5B). COG coordinates for the IS were generated from masks derived from the Alexa Fluor 488 (CTL) channel. To calculate the centralization factor (Figs. 1D and 5, B and D), we first generated a mask encompassing the entire IS (MC) and a mask containing only the features of interest (e.g., lytic granules) (MF) using xy-projection images. Then, the average distance between every pixel in MC and the COG of MC (DC) was determined and subsequently divided by the average distance between every pixel in MF and the COG of MC (DF) (fig. S2). Granule polarization (Fig. 1D) was quantified by determining the vertical distance between the centroid of a mask encompassing the lytic granules and the deepest CTL protrusion, using xz- or yz-projection images. To calculate target IS volume (Fig. 7, B and C), we generated a three-dimensional mask at a time point of interest by tracing the edges of the IS and then propagating the resulting shape downward to encompass the sample lying directly beneath the CTL. The volume of this region occupied by the target cell was then divided by the volume of this same region occupied by the target cell at time 0 (Figure ??).

#### **2.4.6 Killing assay, granule fusion assays, and conjugate formation**

RMA-s target cells were labeled with carboxyfluorescein succinimidyl ester (CFSE) or the membrane dye PKH26, loaded with OVA and mixed in a 96-well V-bottomed plate with CellTrace Violet (CTV)-stained OT1 CTLs. To assess killing, we mixed cells at a 1:3 effector: target (E:T) ratio and incubated them for 4 hours at 37 °C. Specific lysis of CFSE+ target cells was determined by flow cytometry (61).

For granule fusion assays, the E:T ratio was 1:1, and cells were incubated at 37°C for 90 min in the presence of eFluor 660-labeled anti-Lamp1 (clone eBio1D4B; eBioscience). Lamp1 staining was then assessed by flow cytometry. To measure conjugate formation, we mixed CTLs and targets 1:1, lightly centrifuged (100g) the mixture to encourage cell contact, and incubated the mixture for 20 min at 37°C. Cells were then resuspended in the presence of 2% paraformaldehyde, washed in fluorescence- activated cell sorting buffer (PBS + 4% FCS), and analyzed by flow cytometry. Conjugate formation was quantified as (CFSE+ CTV+)/(CTV+). For killing of adherent target cells, MB49 or B16 cells were cultured overnight on fibronectin and then pulsed with OVA for 2 hours. OT1 CTLs were added at a 4:1 E:T ratio and incubated for 3 hours (MB49 cells) or 4 hours (B16) at 37°C in RPMI medium supplemented with interleukin-2 (30 IU/ml). Target cell death was quantified with an LDH (lactate dehydrogenase) cytotoxicity assay kit (Clontech) using the manufacturer's recommended protocol. All functional assays were performed in triplicate.

#### 2.4.7 Statistical analysis

Figures show representative experiments. Analysis was carried out using either representative experiments or pooled data as indicated (n refers to the number of cells analyzed). Statistical analyses (unpaired or paired t tests) were carried out using GraphPad Prism or Microsoft Excel. All error bars denote SEM.

## 2.4.8 Constructs

Retroviral expression constructs for Lifeact-GFP, Lifeact-mRuby2, DynPH-GFP, and pHluorin-Lamp1 were previously described (8, 22). The Lamp1-GFP, WASP- GFP, and WAVE2-GFP constructs were prepared by ligating the full-length coding sequences of mouse Lamp1, mouse WASP, and human WAVE2 into a pMSCV retroviral expression vector upstream of GFP (61). The Lifeact-mApple fusion was prepared by PCR from an mApple-N1 template plasmid using oligos that encoded the Lifeact peptide N-terminal to mApple, followed by subcloning into pMSCV. shRNA constructs (shNT and shPTEN) (8) were subcloned into the miR30E vector (62) using the following primers: miRE-Xho-fw (5'-TGAACTCGAGAAGGTATAT TGCTGTTGACAGTGAGCG-3') and miRE-EcoOligo-rev (5'-TCTCGAATTCT AGCCCCCTGAAGTCCGAGGCAGTAGGC -3'). gRNAs targeting WASP and WAVE2 were generated as previously described (63, 64) using the following oligos: NT gRNA: oligo-1 (5'- CAC- CGGGATACTGGGCCGACTTTC -3') and oligo-2 (5'- AAACGAAAGTCG- GCCCAGGTATCCC -3'). WASP gRNA: oligo-1 (5'- CACCGCTGGACCATG- GAACACTGCG -3') and oligo-2 (5'- AAACCGCAGTGTCCATGGTCCAGC -3'). WAVE2 gRNA: oligo-1 (5'-CACCGAGCAAGGGAGTTACTCGGG-3') and oligo-2 (AAACCCCGAGTAAACTCCCTGCTC -3'). Each gRNA was cloned into the LentiGuide-Puro vector and then amplified by PCR using the following primers: LMP BamHI F2 (5'- TTTTGATCCTAGTAGGAGGCTGGTAG -3') and LMP EcoRI R2 (5'- TTTTGAAATTCTGTCTACTATTCTTCCC -3'). The resulting fragments were digested with BamHI and EcoRI and ligated into miR30E previously digested with EcoRI and BglII.

#### **2.4.9 Cells and small molecule inhibitors**

The animal protocols used for this study were approved by the Institutional Animal Care and Use Committee of Memorial Sloan-Kettering Cancer Center. Primary CTL blasts were prepared by pulsing irradiated C57BL/6 splenocytes with 100 nM OVA and then mixing them with T cells from OT1  $\alpha\beta$  TCR transgenic mice in RPMI medium containing 10%(vol/vol) FCS. Cells were supplemented with 30 IU/ml IL2 after 24 h and were split as needed in RPMI medium containing 10% (vol/vol) FCS and IL2. RMA-s cells were maintained in RPMI containing 10% (vol/vol) FCS, while C57BL/6 murine cardiac microvascular endothelial cells (CellBiologics), MB49 cells, and B16 cells were maintained in DMEM medium containing 10% (vol/vol) FCS. To inhibit Arp2/3, CTLs were preincubated with CK666 (100-150  $\mu$ M, Sigma-Aldrich) for 10 min at 37°C, and CK666 was then maintained at the same concentration for the duration of the experiment.

#### **2.4.10 Retroviral transduction**

Phoenix E cells were transfected with expression vectors and packaging plasmids using the calcium phosphate method. Ecotropic viral supernatants were collected after 48 h at 37°C and added to  $1.5 \times 10^6$  OT1 blasts 2 days after primary peptide stimulation. Mixtures were centrifuged at  $1400 \times g$  in the presence of polybrene (4  $\mu$ g/ml) at 35°C, after which the cells were split 1:3 in RPMI medium containing 10% (vol/vol) FCS and 30 IU/ml IL2 and allowed to grow for an additional 4-6 days.

#### **2.4.11 Fixed imaging**

OT1 cells were incubated on stimulatory micropillars for 20 min at 37°C, fixed by adding 4% paraformaldehyde for 5 min, and washed with PBS. Samples were then blocked in PBS solution supplemented with 2% goat serum for 1 h at room temperature and stained overnight at 4°C with anti- $\beta$ -tubulin (clone TUB 2.1; Sigma) or anti-LFA1 (clone M14/7; eBioscience). Actin was visualized using Alexa 546-labeled phalloidin (ThermoFisher Scientific). After washing, samples were incubated with the appropriate secondary antibody for 2 h at room temperature, washed and imaged using a Leica SP8 confocal laser scanning microscope fitted with a white light laser and a 40x objective lens.

#### **2.4.12 $Ca^{2+}$ imaging**

CTLs were loaded with 5  $\mu$ g/ml Fura2-AM (ThermoFisher Scientific), washed, and then imaged on stimulatory glass surfaces coated with H2- $K^b$ -OVA and ICAM-1 as previously described (62). Images were acquired using 340 nm and 380 nm excitation every 30 seconds for 30 min with a 20x objective lens (Olympus).

#### **2.4.13 Adhesion assay**

Integrin-mediated adhesion was measured in flat-bottomed 96-well plates bearing increasing densities of ICAM1. The plates were coated with 10  $\mu$ g/ml streptavidin in PBS followed by increasing concentrations of biotinylated ICAM1 in the presence or absence of 1  $\mu$ g/ml biotinylated H2- $K^b$ -OVA in Hepes buffered

saline (10 mM Hepes pH 7.5, 150 mM NaCl) with 2 % BSA. The total concentration of biotinylated protein during coating was kept at 5  $\mu$ g/ml by the addition of nonspecific biotinylated MHC (H2-Db). OT1 CTLs were fluorescently labeled with cell trace violet (CTV), resuspended in adhesion buffer (PBS with 0.5% BSA, 2 mM MgCl<sub>2</sub>, 1 mM CaCl<sub>2</sub>), and added to ICAM1-bearing wells in triplicate. After a 20 min incubation at 37°C, wells were washed with warmed adhesion buffer as described (62), and the bound cells quantified by fluorimetry.

#### 2.4.14 Immunoblot

0.2-1  $\times$  10<sup>6</sup> CTLs were lysed using cold cell lysis buffer containing 50 mM TrisHCl, 0.15 M NaCl, 1 mM EDTA, 1% NP-40 and 0.25% sodium deoxycholate. Suppression of PTEN, WASP, and WAVE2 was confirmed using the following antibodies: anti-PTEN monoclonal antibody (clone D4.3; Cell Signaling Technology), anti-WASP monoclonal antibody (clone B-9; Santa Cruz) and anti-WAVE2 monoclonal antibody (clone D2C8; Cell Signaling Technology). Actin served as a loading control (clone AC-15, Sigma). For signaling assays, serum and IL2 starved OT1 CTLs were incubated with streptavidin polystyrene beads (Spherotech) coated with H2-K<sup>b</sup>-OVA and ICAM1 at a 1:1 ratio for various times at 37°C and immediately lysed in 2  $\times$  cold lysis buffer containing phosphatase inhibitors (1 mM NaF and 0.1 mM Na<sub>3</sub>VO<sub>4</sub>) and protease inhibitors (cOmplete mini cocktail, EDTA-free, Roche). Activation of PI3K, MAP kinase and NF- $\kappa$ B signaling was assessed by immunoblot for pAkt (Phospho-Akt (Ser473) Ab; Cell Signaling Technology), pErk1/2 (Phospho-Thr202/ Tyr204; clone D13.14.4E; Cell Signaling Technology), and I $\kappa$ B (Cell Signaling Technology).

# CHAPTER 3

## MECHANICALLY ACTIVE INTEGRINS DIRECT CYTOTOXIC SECRETION AT THE IMMUNE SYNAPSE

Results presented in this chapter have been submitted as: Wang, M. S., Hu, Y., Sanchez, E. E., Xie, X., Roy, N. H., de Jesus, M., Jin, W., Lee, J. H., Hong, Y., Kam, L. C., Salaita, K., Huse M., as *Mechanically active integrins direct cytotoxic secretion at the immune synapse*.

### 3.1 Background

The secretory output of cell-cell interfaces must be tightly controlled in space and time to ensure functional efficacy. This is particularly true for the cytotoxic immune synapse (IS), the stereotyped junction formed between a cytotoxic lymphocyte and the infected or transformed target cell it aims to destroy<sup>1</sup>. Cytotoxic lymphocytes kill their targets by channeling a mixture of granzyme proteases and the pore forming protein perforin directly into the IS<sup>2, 3</sup>. The synaptic secretion of these toxic molecules constrains their deleterious effects to the target cell alone, thereby protecting innocent bystander cells in the surrounding tissue from collateral damage. Despite the importance of this process for immune specificity, the molecular and cellular mechanisms that establish secretory sites within the IS remain poorly understood. Here, we identified an essential role for integrin mechanotransduction in cytotoxic secretion using a combination of single cell biophysical measurements, ligand micropatterning, and functional assays. Upon ligand-binding, the  $\alpha L\beta 2$  integrin LFA-1 functioned as a spatial cue, attracting lytic granules containing perforin and granzyme and inducing their

fusion at closely adjacent sites within the synaptic membrane. LFA-1 molecules were subjected to pulling forces within these secretory domains, and genetic or pharmacological suppression of these forces abrogated cytotoxicity. We conclude that lymphocytes employ an integrin-dependent mechanical checkpoint to enhance both the potency and the security of their cytotoxic output.

### **3.1.1 Canonical centrosome-based model of degranulation**

Given that degranulation is the lynchpin to effector T cell function, there has been much research into the precise mechanism of degranulation and how lytic granules arrive and fuse at the immune synapse for optimized killing. Effective target killing depends on the exclusive release of granule contents solely at the IS. This creates a local hyperconcentration of perforin and granzymes delivered to the target, while simultaneously minimizing damage to bystander cells in the surrounding tissue. Directional granule release (also called degranulation) is generally thought to depend on the centrosome, a membraneless organelle that serves as the microtubule-organizing center (MTOC) in most cells (7, 8). Microtubules radiate from the centrosome with their minus ends directed inward and their plus ends outward. Centrosomes usually contain two centrioles, which are cylindrical structures made of parallel microtubule triplets, surrounded by a cloud of proteinaceous pericentriolar material (PCM). The centrioles maintain centrosomal organization, while the PCM, which is highly enriched in  $\gamma$ -tubulin, is responsible for nucleating microtubule growth. A defining stage of IS formation is the movement of the centrosome to a position just beneath the center of the interface. Lytic granules cluster around the centrosome in activated lymphocytes, and, therefore, its reorientation to the IS positions the granules close to the

synaptic membrane (2, 9). The temporal coordination among granule clustering, centrosome reorientation, and target cell killing implies that the centrosome delivers the granules to the IS for fusion, thereby maintaining the potency and specificity of the response. Consistent with this model, multiple studies have associated delayed or impaired centrosome reorientation with reduced cytotoxicity (10–13). Furthermore, deletion of Cep83, a centrosomal protein required for centriole docking with the plasma membrane, was found to inhibit CTL degranulation (14). Other studies, however, have suggested that robust CTL and NK cell-mediated killing occurs in the absence of centrosome polarization (15–17). Hence, the precise role of the centrosome during cytotoxic responses remains unelucidated.

### **3.1.2 Force-directed localization of synaptic granule fusion**

- discuss fig 7 in detail, 2016 basu cell paper

### **3.1.3 Actin cytoskeletal direction of synaptic integrin localization**

WASP LFA1 loic dupre paper

### **3.1.4 Integrin biology and mechanotransduction**

Transmembrane heterodimers

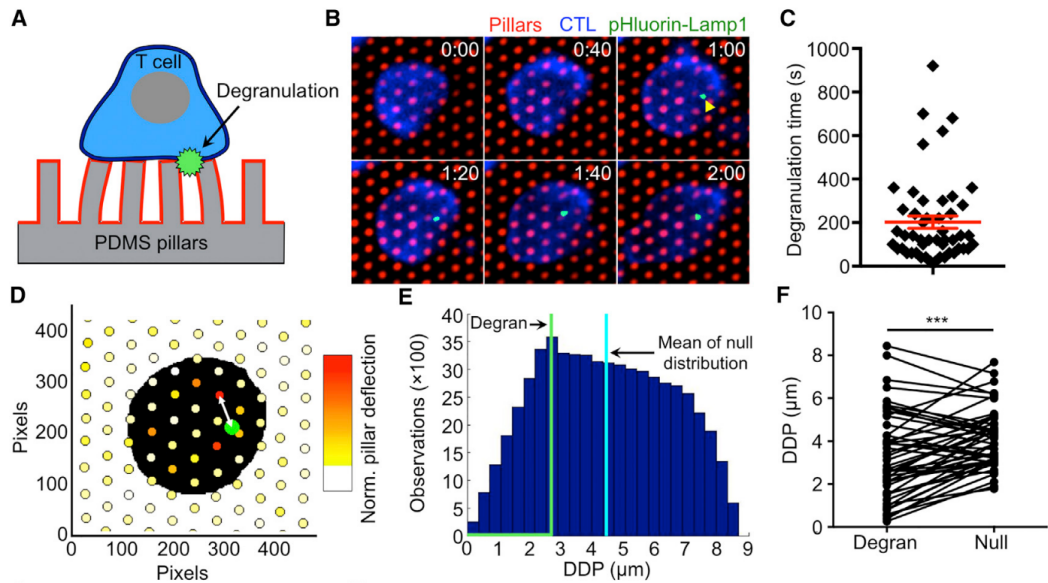


**Figure 3.1:** Degranulation is spatiotemporally correlated with force exertion at the IS.

**(A)**: Diagram schematizing fluorescent detection of degranulation during a micropillar experiment. **(B)**: Representative time-lapse montage showing pillar deflections during a degranulation event (indicated by the yellow arrowhead). Time is indicated in M:SS in the top right corner of each image. **(C)**: Graph of the offset time between contact formation and degranulation (degranulation time). **(D)**: Graphical representation of the pillar array in **(B)**, with the degranulation position depicted as a green circle and the cell envelope at the moment of degranulation shown in black. Pillars are color-coded based on their average deflection during the degranulation. Warmer colors (e.g., orange, red) denote stronger deflections. The DDP for this degranulation is indicated by the double-headed white arrow. **(E)**: Histogram plot derived from the experiment in **(B)** showing the DDP for each position in the CTL interface. The mean value for the distribution is denoted by the vertical cyan line. The vertical green line indicates the DDP for the degranulation itself. **(F)**: DDPs of degranulation (Degran) were compared to the mean values of their paired null distributions. \*\*\* $p < 0.001$ , calculated by two-tailed paired t test. This figure is adapted from [25].

Integrins fine-tune TCR signaling by restricting the flow of actin at the immune synapse [28].

LFA-1 function is essential for the activation and proliferation of naïve T cells [29]

## 3.2 Results

### 3.2.1 LFA-1 is required for synaptic force exertion, degranulation, and cytotoxicity

Lytic granules, the specialized secretory lysosomes that store perforin and granzyme, are known to accumulate at the IS and fuse selectively with the synaptic membrane<sup>2, 3</sup>. This behavior has long been attributed to the centrosome, which serves as a focal point for intracellular granules and polarizes toward the target cell during IS formation<sup>2, 4</sup>. Studies from our group and others, however, indicate that the centrosome is dispensable for synaptic secretion, implying the existence of other targeting mechanisms<sup>5-7</sup>. Cytotoxic lymphocytes exert nanonewton scale forces across the IS that have been implicated in both the activation of mechanosensitive cell surface receptors and the potentiation of perforin function<sup>8-14</sup>. We have found that lytic granule exocytosis (degranulation) tends to occur in regions of active force exertion within the IS<sup>8</sup>, raising the possibility that local mechanosensing might play an instructive role in guiding perforin and granzyme release. To explore this hypothesis, we studied the degranulation requirements of primary murine CD8+ cytotoxic T lymphocytes (CTLs), which are activated by T cell receptor (TCR)-mediated recognition of antigenic peptide-major histocompatibility complex (pMHC) on the target cell. The CTLs we used for our experiments expressed the OT-1 TCR, which is specific for the ovalbumin<sup>257-264</sup> peptide (OVA) bound to the class I MHC protein H2-K<sup>b</sup>. pMHC recognition by the TCR triggers IS formation and the “inside-out” activation of cell surface integrins<sup>1, 15</sup>, including LFA-1 (Lymphocyte function-associated antigen-1), which establishes strong adhesion by binding to its cognate

ligands Intercellular adhesion molecule-1 (ICAM-1) and ICAM-2 on the opposing membrane. Using micropillar-based traction force microscopy<sup>16</sup>, we found that LFA-1 engagement substantially increased synaptic force exertion (Figure ??), implying that this integrin is a key player in IS mechanics and therefore a candidate for mediating coupling between mechanical and secretory output.

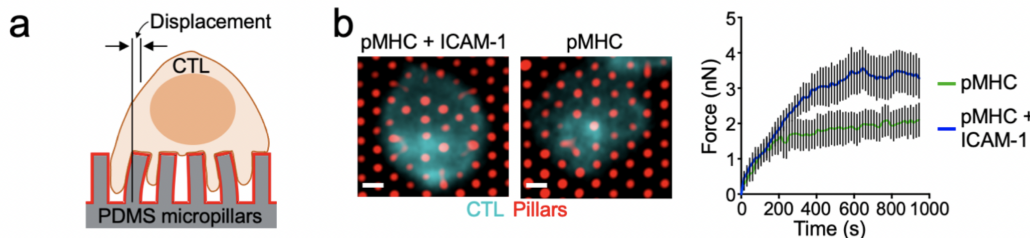


**Figure 3.2:** LFA-1 is required for synaptic force exertion.

(A): OT-1 CTLs labeled with fluorescent anti-CD45 Fab were stimulated on PDMS micropillar arrays coated with pMHC  $\pm$  ICAM-1. Traction forces were derived from pillar displacement. (B): Left, representative images of CTLs interacting with the arrays. Scale bars = 2  $\mu$ m. Right, mean force exertion against the array graphed against time. N is  $\geq$  to 8 for each sample.

To evaluate the importance of LFA-1 for degranulation and cytotoxicity, we treated cocultures containing OT-1 CTLs and OVA-loaded RMA-s target cells with a neutralizing antibody that specifically disrupts LFA-1-ICAM-1/2 binding (Figure 3.3). Blocking LFA-1 in this manner dramatically inhibited antigen-induced degranulation, which we measured by surface exposure of the lysosomal marker Lamp1 (Fig. 1d and Fig. S1a) and by the depletion of intracellular granzyme B (Fig. S1b).

Anti-LFA-1 neutralizing antibodies also strongly suppressed cytotoxicity, as quantified by lysis of target cells (Fig. 1e). LFA-1 engagement was similarly important for degranulation responses elicited by stimulatory beads coated with pMHC and/or ICAM-1 (Fig. S1c-e).

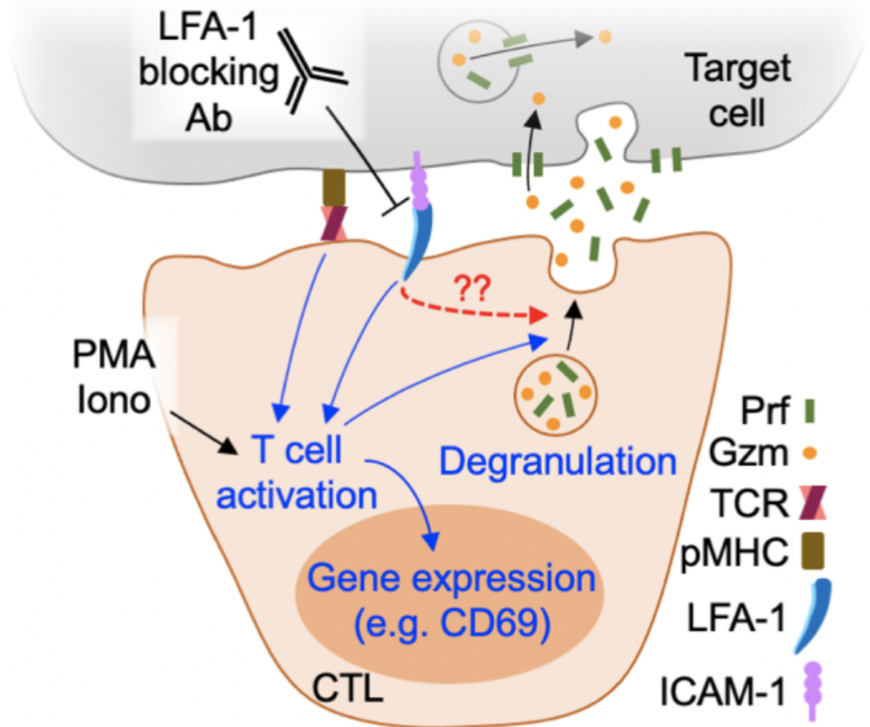


**Figure 3.3:** Model of antibody blocking of LFA-1 and small molecule-mediated T cell activation.

OVA-loaded RMA-s target cells were mixed with OT-1 CTLs in the presence of LFA1 blocking antibody ( $\alpha$ LFA-1) or isotype control. PMA/Iono was applied to some samples in order to drive TCR independent CTL activation.

Collectively, these results were consistent with a specific role for LFA-1 in degranulation, but they did not rule out the possibility that LFA-1 engagement might promote this response secondarily by augmenting T cell activation (Fig. 1c). Indeed, LFA-1 is known to function as a “costimulatory” receptor by lowering the antigen threshold required for signaling and TCR-induced gene expression<sup>17, 18</sup>. In our hands, LFA-1 blockade altered some, but not all, of these responses. We observed no effect on antigen-induced proliferation (Fig. S2a), assessed by dilution of CellTrace Violet dye. Signaling through the MAP kinase (MAPK) and PI-3 kinase (PI3K) pathways, which we measured by phosphorylation of

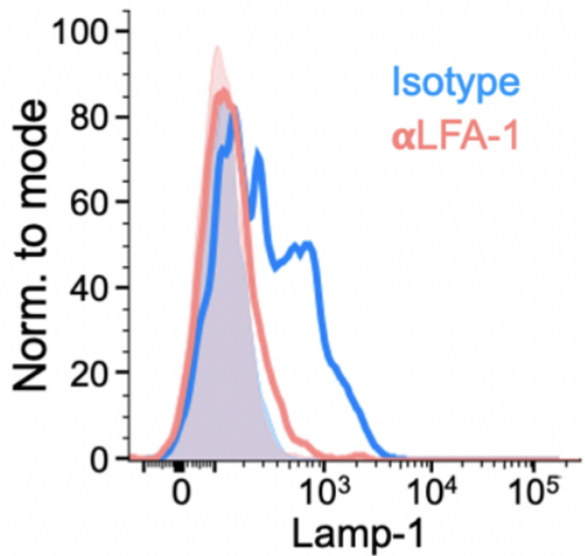


**Figure 3.4:** Measuring degranulation via flow cytometry.

A representative FACS histogram of CTL Lamp1 staining, measured 90 min after cell mixing.

Erk1/2 and Akt, respectively, was also normal (Fig. S2b). Conversely, antibody treatment dampened cytosolic calcium ( $Ca^{2+}$ ) influx (Fig. S2c) and inhibited the upregulation of CD69, an immediate early response gene (Fig. 1f and S1f).

To decouple these LFA-1 dependent effects on T cell activation from a distinct and specific role in degranulation, we used a combination of phorbol myristate acetate (PMA) and the  $Ca^{2+}$  ionophore A23187 (Iono) to induce T cell activation in the absence of TCR engagement (Fig. 1c, S1c). CTLs treated with PMA/Iono alone exhibited robust CD69 expression (Fig. 1f, S1f), indicative of strong activation. Their degranulation responses were quite modest, however (Fig. 1d, S1e), pointing to the importance of target contact/proximity in stimulating cytotoxic secretion. Indeed, robust Lamp1 exposure was only observed in CTLs that were concomitantly exposed to antigenic pMHC and ICAM, either on target cells or on beads. Critically, this ligand-induced component of degranulation was com-

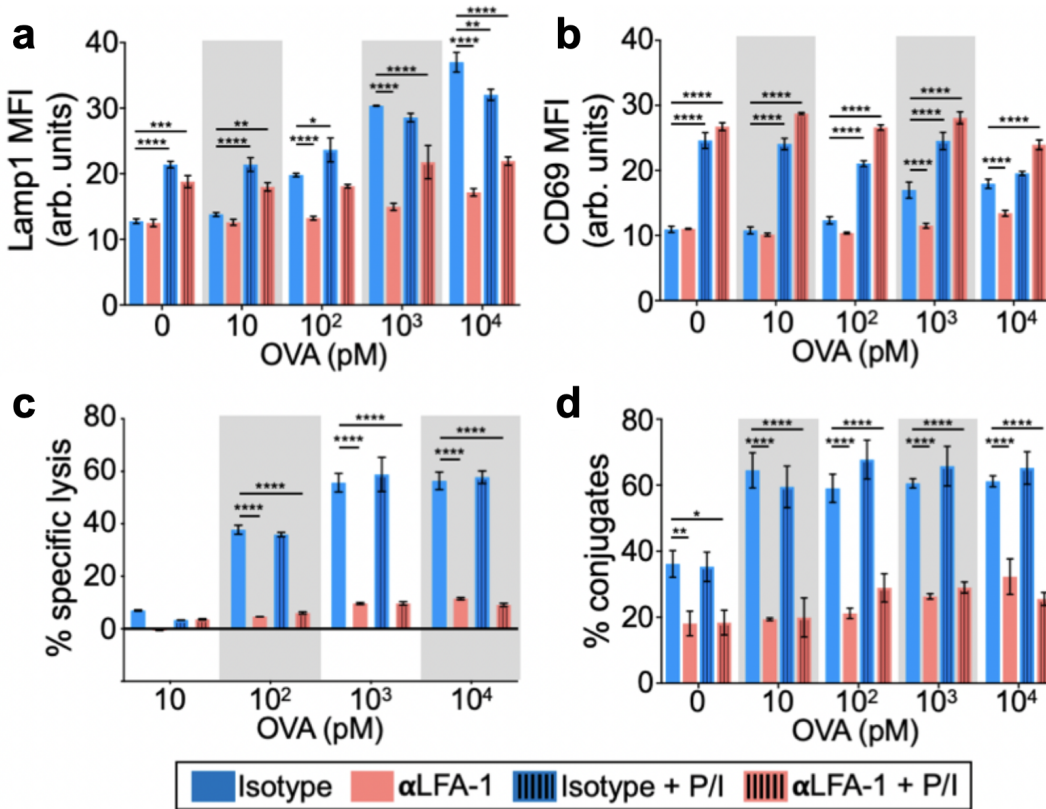


**Figure 3.5:** LFA-1 is required for synaptic force exertion, degranulation, and cytotoxicity.

(A): Lamp1 exposure (degranulation), measured 90 min after CTL-target cell mixing. (B): Target cell killing, measured 4 h after CTL-target cell mixing. (C): CD69 expression, measured 90 min after CTL-target cell mixing. (D): Conjugate formation, measured 90 min after CTL-target cell mixing. Data in (A-D) were derived from technical triplicates. All error bars denote SEM. \*, \*\*, \*\*\*, and \*\*\*\* denote  $P \leq 0.05$ ,  $P \leq 0.01$ ,  $P \leq 0.001$ , and  $P \leq 0.0001$ , calculated by 2way ANOVA. All data are representative of at least two independent experiments.

pletely inhibited by LFA-1 blockade (Fig. 1d, S1e). Taken together, these results indicate that LFA-1 engagement promotes cytotoxic secretion independently of T cell activation and at a level downstream of early signaling events. Notably, LFA-1 was also required for the formation of strong CTL-target cell conjugates, both in the presence and in the absence of PMA/Iono (Fig. 1g). Hence, the capacity of LFA-1 to stimulate degranulation was phenotypically linked to its ability to mediate strong adhesion.

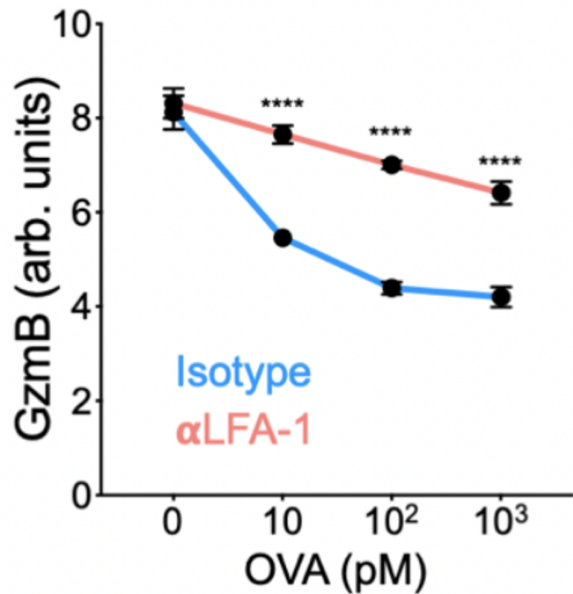


**Figure 3.6:** LFA block prevents release of granzyme B.

Staining for intracellular granzyme B (GzmB) in CTLs, performed 90 min after cell mixing.

### 3.2.2 Degranulation occurs in IS domains containing ligand-bound TCR and ligand-bound LFA-1

That both the TCR and LFA-1 were required for robust degranulation (Fig. 1 and S1) raised the possibility that both receptor types must be engaged within the same cell-cell interface to elicit cytotoxic responses. This requirement would presumably enhance the specificity of killing by ensuring that toxic factors are released only against bona fide target cells (expressing cognate pMHC) that are tightly associated with the CTL (via integrin adhesion). To test this idea, we stimulated CTLs using beads coated with both pMHC and ICAM-1 (cis) or using a mixture of beads coated separately with only pMHC or ICAM-1 (trans) (Fig. 2a). Care was taken to make sure that the total amount of accessible pMHC and

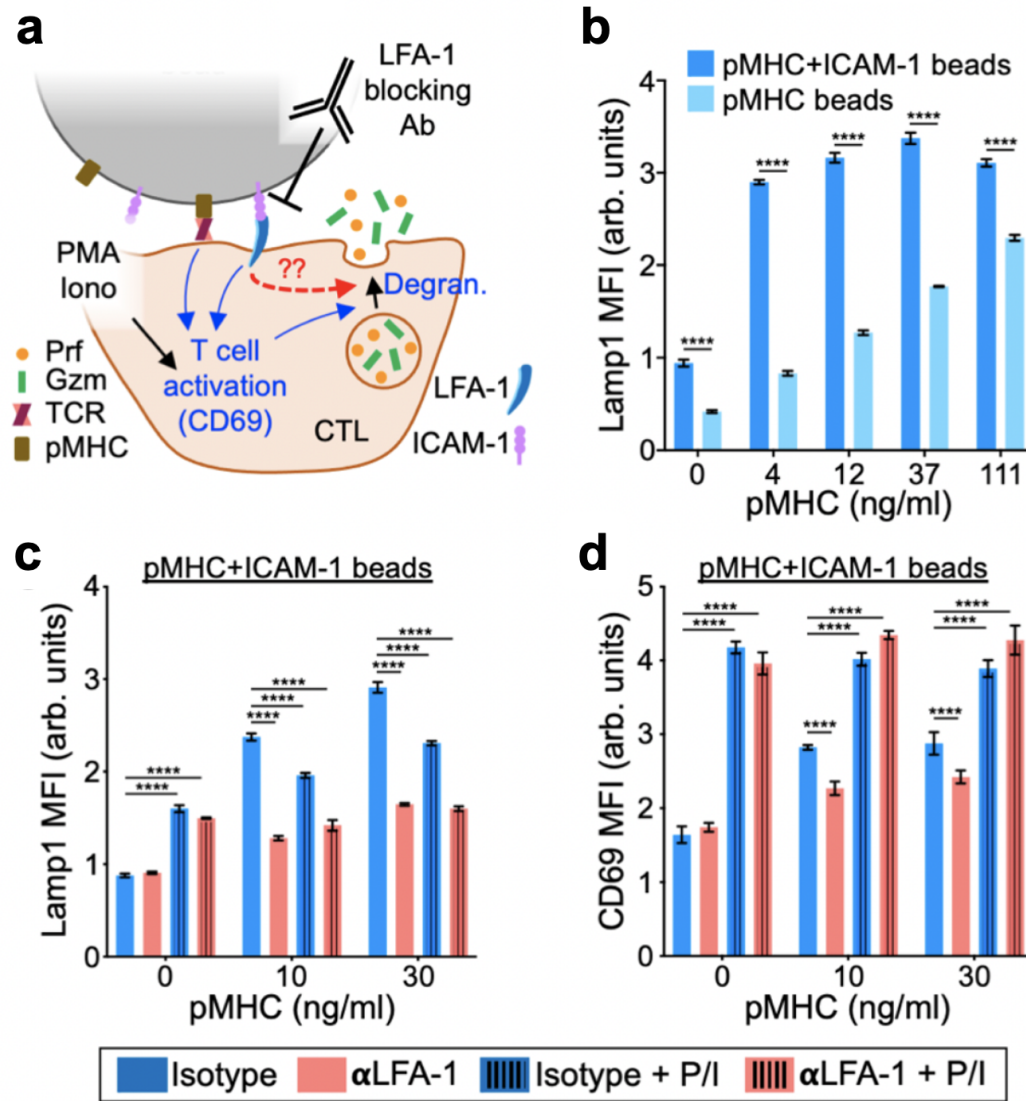


**Figure 3.7:** LFA-1 blockade disrupts CTL degranulation.

(A): A diagram schematizing CTL activation by stimulatory beads coated with pMHC (H-2K<sup>b</sup>-OVA) ± ICAM-1. (B): OT-1 CTLs were mixed with beads coated with increasing amounts of pMHC in the presence or absence of ICAM-1. Degranulation was measured 90 min after CTL stimulation. (C-D) Beads coated with pMHC and ICAM-1 were incubated with OT-1 CTLs in the presence or absence of PMA/Iono and treated with either  $\alpha$ LFA-1 or isotype control. Graphs show degranulation (C) and CD69 expression (D) measured 90 min after CTL stimulation. All error bars denote SEM. \*, \*\*, \*\*\*, and \*\*\*\* denote  $P \leq 0.05$ ,  $P \leq 0.01$ ,  $P \leq 0.001$ , and  $P \leq 0.0001$ , calculated by 2way ANOVA. All data are representative of at least two independent experiments.

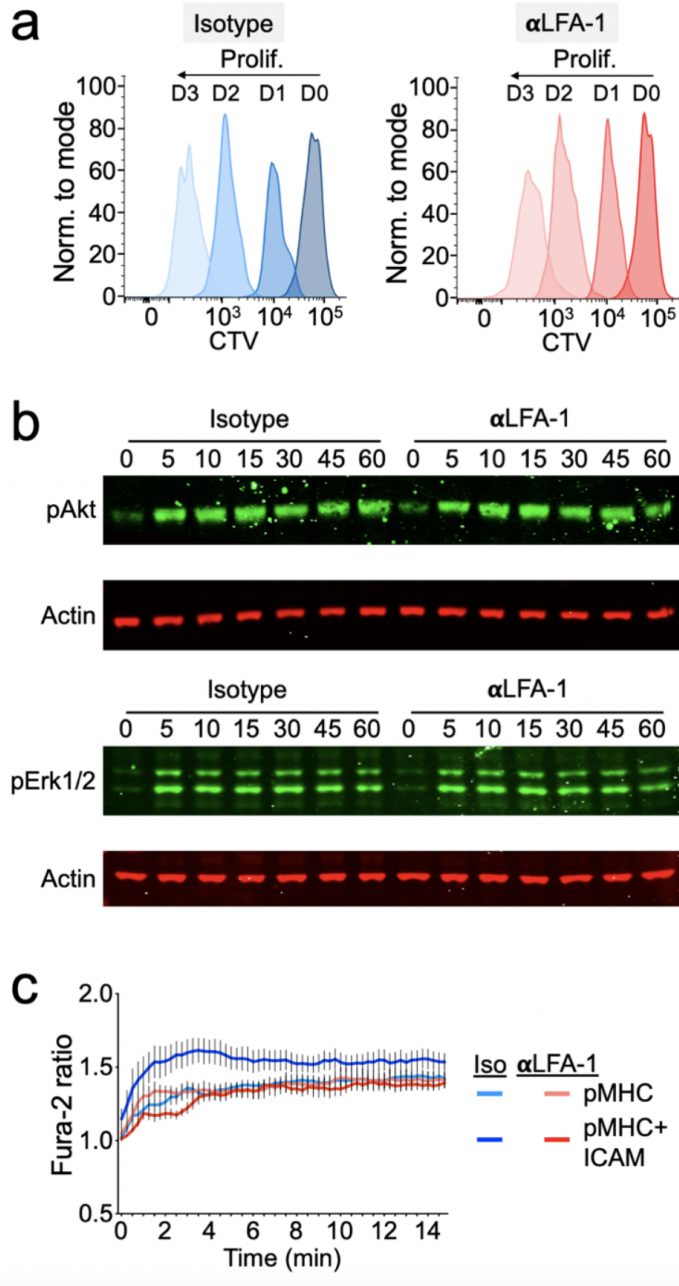


**Figure 3.8:** LFA-1 blockade alters only some indices of T cell activation.

(A): OT-1 CTLs were labeled with CellTrace Violet (CTV) and incubated with OVA-loaded splenocytes in the presence of  $\alpha$ LFA-1 or isotype control. CTV dilution was monitored over 3 days (A) by flow cytometry. (B): OT-1 CTLs were mixed with pMHC ( $H2-K^b$ -OVA) and ICAM-1 coated beads and, at the indicated timepoints, pAKT (top) and pErk1/2 (bottom) were assessed by immunoblot, with actin serving as a loading control. (C) OT-1 CTLs were loaded with Fura-2-AM and imaged on glass surfaces coated with the indicated proteins in the presence of  $\alpha$ LFA-1 or isotype control. Graph shows the mean Fura-2 ratio of all CTLs in the imaging field, averaged over 6 positions. Error bars denote SEM. All data are representative of at least two independent experiments.

ICAM-1 was identical in each experimental group and that CTLs could engage multiple beads simultaneously (Fig. S3a).

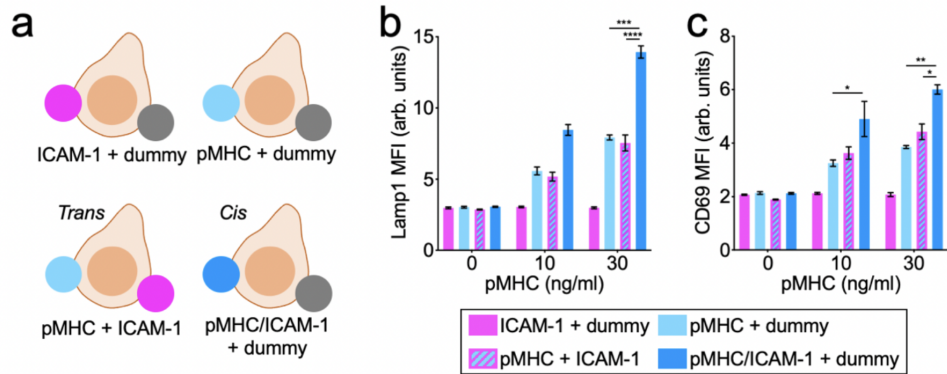


**Figure 3.9:** Degranulation occurs in IS domains containing both ligand-bound TCR and ligand-bound LFA-1.

**(A-C):** OT-1 CTLs were activated by equal mixtures of stimulatory beads bearing the indicated proteins. **(A):** A schematic of the experiment. Dummy denotes beads coated with nonstimulatory pMHC ( $H2-K^b$ -KAVY) alone. Trans and cis copresentation of  $H2-K^b$ -OVA and ICAM-1 are indicated. **(B-C):** Graphs showing CTL degranulation **(B)**: and CD69 expression **(C)**: measured 90 min after CTL stimulation. Data were derived from technical triplicates.

Strikingly, immobilized ICAM-1 boosted TCR-induced degranulation only when presented in the cis configuration (Fig. 2b). Indeed, CTLs stimulated with the trans mixture of pMHC- and ICAM-1- coated beads responded indistinguishably from CTLs stimulated with pMHC beads alone. We observed the same pattern of results using CD69 upregulation as the downstream readout (Fig. 2c). Hence, ligand-bound LFA-1 must share the same interface as the ligand-bound TCR in order to boost cytotoxicity and T cell activation. Building upon this idea, we next examined whether local coengagement of LFA-1 and the TCR could control the position of degranulation events within the IS. Using protein microstamping<sup>19</sup>, we prepared glass coverslips containing  $2\ \mu m$  spots of fluorescent streptavidin spaced in a  $10\ \mu m \times 10\ \mu m$  square grid. These surfaces were then incubated with mixtures of unbiotinylated proteins to coat/block the

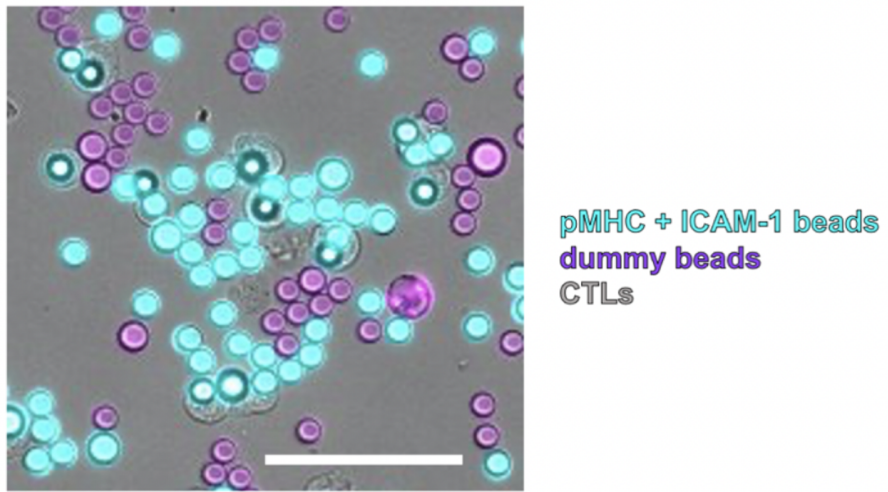


**Figure 3.10:** CTL stimulation with spatially segregated ligands on beads.

Representative image of OT-1 CTLs, pMHC-coated beads, and ICAM-1 coated beads mixed at the proportions used for Figure 2a-c. Scale bar = 50  $\mu\text{m}$ .

empty glass between streptavidin spots, and then with biotinylated proteins to load the spots themselves. By varying the composition of coating and loading mixtures, we were able to generate a panel of distinct micropatterned substrates: 1) ICAM-1 spots within a uniform background of pMHC (ICAM-spot), 2) pMHC spots on an ICAM-1 background (Antigen-spot), and 3) spots containing both ICAM-1 and pMHC on a nonstimulatory (BSA coated) background (Dual-spot) (Fig. 2d). We also generated control surfaces containing empty streptavidin spots in a background of admixed pMHC and ICAM-1. CTLs plated on Dualspot surfaces evinced  $\text{Ca}^{2+}$  flux only during periods of spot contact (Fig. S3b and Movies S1-2), confirming that biotinylated stimulatory ligands could be constrained in space by the patterned streptavidin.

To monitor degranulation position in this system, we employed a reporter construct in which the pH-sensitive fluorescent protein pHluorin is linked to the lytic granule resident protein Lamp120. Because pHluorin is quenched in the

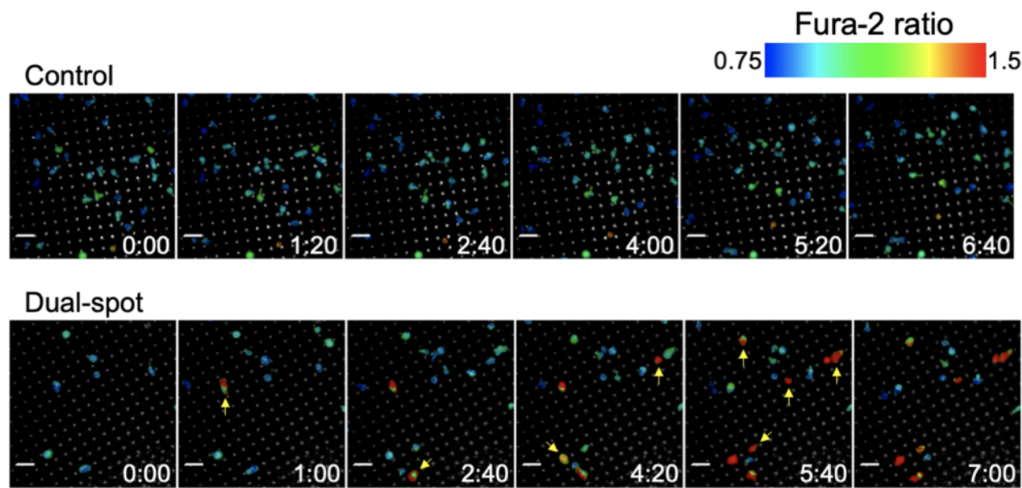


**Figure 3.11:** CTL stimulation with spatially segregated ligands via micropatterning.

Representative time-lapse montages of Fura-2-AM-loaded OT-1 CTLs imaged on Dual-spot and control surfaces. Yellow arrows denote the onset of  $\text{Ca}^{2+}$  flux in individual cells. Time in M:SS is shown in the bottom right corner of each image. Scale bars =  $10 \mu\text{m}$ . All data are representative of at least two independent experiments.

low pH granule environment, it becomes visible only upon fusion, generating a transient burst of fluorescence that reveals the position of the degranulation site within the IS. When CTLs expressing pHluorin-Lamp1 were imaged on ICAMspot, Antigen-spot, or Dual-spot surfaces, degranulation events tended to cluster around the fluorescent spots containing ICAM-1 and/or pMHC (Fig. 2e-f and Movie S3). In all three cases, the mean distance between degranulation events and the spots closest to them was substantially lower than one would expect by chance (dotted line in Fig. 2f) and significantly less than the corresponding distances measured between empty SA spots and degranulations on control surfaces. The enrichment of degranulation in zones where pMHC and ICAM-1 were either copresented (Dual-spot) or closely apposed (ICAM-spot and Antigen-spot) further supports a critical role for the coengagement of the TCR and LFA-1 in guiding cytotoxic secretion and suggests that permissive secretory

domains of receptor coengagement can be substantially smaller than the IS itself [30].

Although all three micropatterned substrates elicited targeted degranulation, responses to the Dual-spot and Antigen-spot configurations were significantly more focused than what we observed on ICAM-spot surfaces (Fig. 2f). To explore the basis for this difference, we imaged CTLs expressing a fluorescent form of the LFA-1 α-chain (CD11a-YFP) on surfaces containing focal LFA-1 or TCR ligands. Because the CD11a-YFP CTLs were derived from a polyclonal animal rather than an OT-1 transgenic, we used an anti-CD3 antibody instead of antigenic pMHC to engage the TCR. On ICAM-spot surfaces (anti-CD3 in the background), LFA-1 tended to localize to the micropatterned ICAM-1 (Fig. 2g), consistent with ligand recognition. The Anti-CD3-spot configuration, however, induced even stronger focal accumulation of LFA-1 (Fig. 2h), which was surprising considering that ICAM-1 was coated in the background of these surfaces. Interestingly, LFA-1 recruitment on Anti-CD3-spot substrates was most apparent not over the anti-CD3 spot itself but in the surrounding 1-2 μm neighborhood. This could potentially reflect inside-out integrin activation and clustering induced by local TCR signaling<sup>15</sup>. The unexpectedly robust accumulation of LFA-1 to areas of focal TCR stimulation potentially explains why Antigen-spot surfaces elicited more focused degranulation than their ICAM-spot counterparts. Within the IS, both the TCR and LFA-1 are subjected to F-actin dependent pulling forces, which are thought to drive the formation of catch bonds between each receptor and its respective ligand, promote conformational changes, and induce signal transduction<sup>10, 11, 14, 21</sup>.

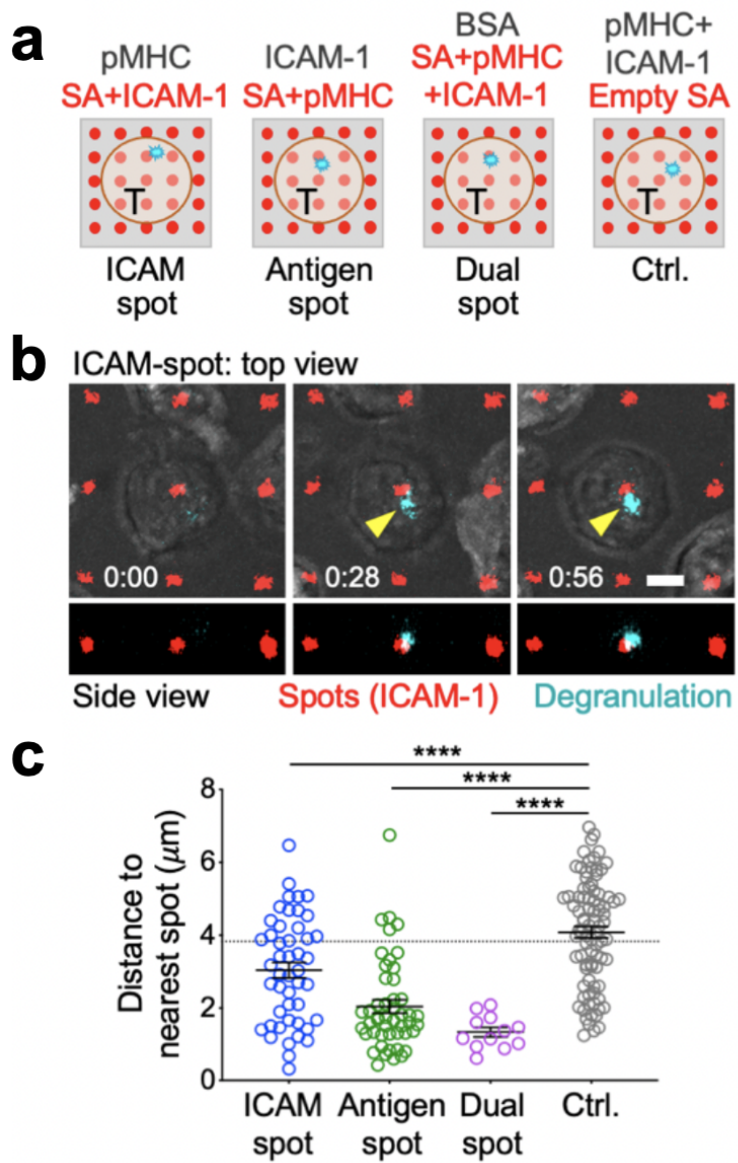


**Figure 3.12:** Degranulation occurs in IS domains containing both ligand-bound TCR and ligand-bound LFA-1.

**(A-B):** OT-1 CTLs expressing pHluorin-Lamp1 were imaged on micropatterned surfaces coated with stimulatory pMHC ( $H2-K^b$ -OVA) and ICAM-1 in 4 different configurations (A). SA = streptavidin. **(B)** Time-lapse montage showing a representative degranulation event (indicated by the yellow arrowhead) on an ICAM-spot surface. In the top views, fluorescent signals have been superimposed on the brightfield image. Time in M:SS is shown at the bottom left corner of the top view images. Scale bars =  $4 \mu\text{m}$ . **(C)** Distance between each degranulation event and the closest fluorescent SA spot in the IS. Dotted line indicates the mean distance expected from randomly placed degranulation.  $N = 12$  for Dual-spot and  $\geq 47$  for the other conditions.

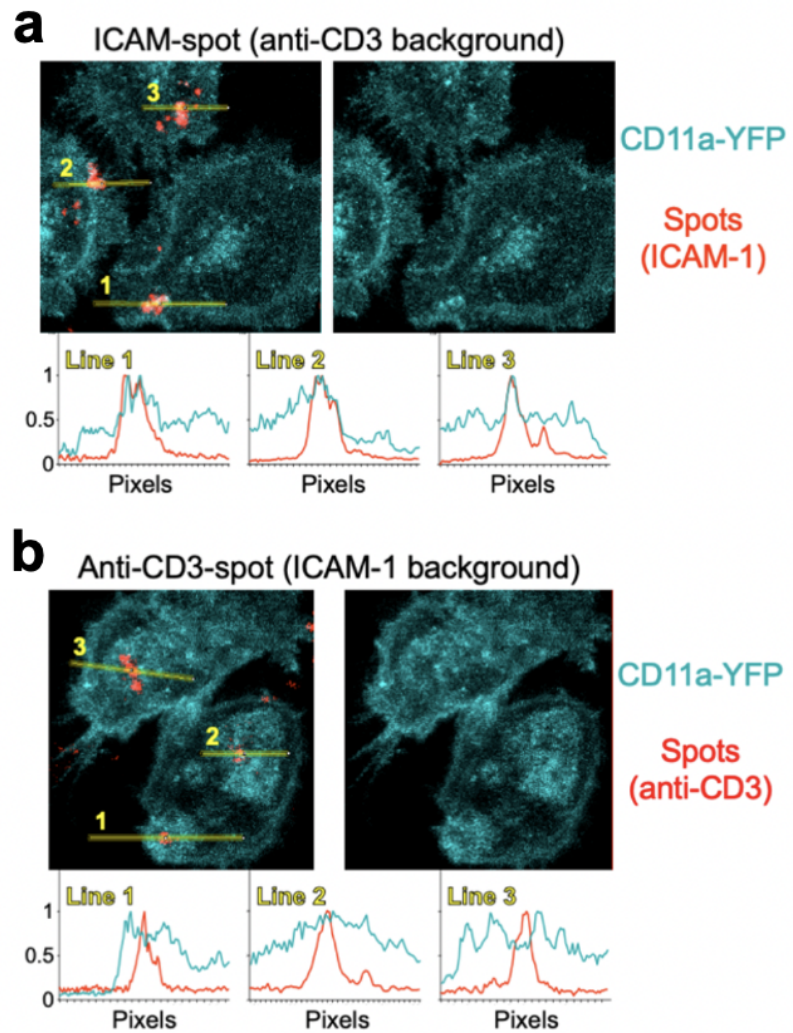


**Figure 3.13:** Local TCR signaling induces adjacent integrin activation.

**(A-B):** CD11a-YFP CTLs were imaged on ICAM-spot **(A)** and Anti-CD3-spot **(B)** surfaces. Representative images are shown in the top of each panel, with linescans through the fluorescent SA spots below. The lines used to generate the linescans are shown in the left image of each panel. All error bars denote SEM. \*, \*\*, \*\*\*, and \*\*\*\* denote  $P \leq 0.05$ ,  $P \leq 0.01$ ,  $P \leq 0.001$ , and  $P \leq 0.0001$ , calculated by 1way (f) and 2way (b-c) ANOVA. All data are representative of at least two independent experiments.

### 3.2.3 LFA-1 pulling forces define degranulation domains

Given the importance of these forces for the function of each receptor, we reasoned that they might also play a role in guiding cytotoxic secretion. To investigate this hypothesis, we employed Förster resonance energy transfer (FRET)-based molecular tension probes (MTPs)<sup>22</sup> specific for the TCR and LFA-1. Each MTP comprised a stimulatory ligand (pMHC or ICAM1) attached to a DNA hairpin containing a fluorophore at one end (Atto647N or Cy3B, respectively) and a quencher (BHQ-2) at the other (Fig. 3a). When folded at resting state, MTPs do not fluoresce due to the close proximity between quencher and fluorophore. Applied forces capable of unwinding the hairpin (in this case, 4.7 pN) pull the quencher and fluorophore apart, dramatically increasing fluorescence. Consistent with prior reports<sup>23, 24</sup>, surfaces coated with pMHC-MTPs and ICAM-1-MTPs induced IS formation by OT1 CTLs and the exertion of dynamic forces through both LFA-1 and the TCR (Fig. 3b and Movie S4), which we visualized by time-lapse imaging.

To measure the association between degranulation and receptor-specific forces, we used CTLs expressing pHluorin-Lamp1 to record exocytic events elicited by stimulatory MTPs (Fig. 3c). The mean MTP fluorescence in the immediate vicinity of each event (2  $\mu$ m box) was then compared with the mean fluorescence of the entire IS. This approach revealed a marked enrichment of ICAM-1-MTP signal in the degranulation zone (Fig. 3d), indicative of a spatial correlation between cytotoxic secretion and force exertion through LFA-1. pMHC-MTP pulling was not associated with degranulation in this way (Fig. 3d), arguing against a role for the TCR as a critical force bearing receptor in this context. To further characterize the pattern of LFA-1 mechanics, we examined

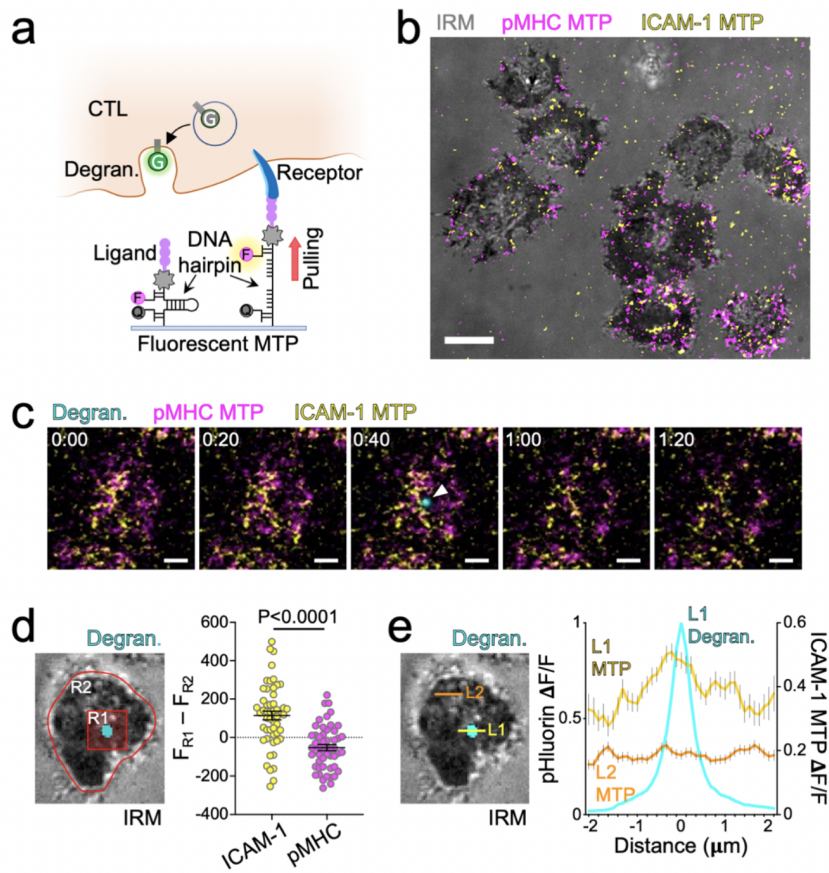


**Figure 3.14:** LFA-1 pulling forces define degranulation domains.

**(A):** Measuring correlations between degranulation (Degran.) and receptor specific pulling forces with MTPs.  $F$  = fluorophore,  $Q$  = quencher,  $G$  = pHluorin. **(B-E):** OT-1 CTLs expressing pHluorin-Lamp1 were imaged by TIRF microscopy on glass surfaces coated with pMHC ( $H2-K^b$ -OVA) and ICAM-1 MTPs. **(B):** Representative image of pMHC-MTP and ICAM-1-MTP signals, overlaid onto the corresponding IRM image. Scale bar =  $5 \mu\text{m}$ . **(C):** Time-lapse montage showing a representative degranulation event (indicated by a white arrowhead) together with pMHC-MTP and ICAM-1-MTP signals. Time in M:SS is shown at the top left corner of each image. Scale bars =  $2 \mu\text{m}$ . **(D):** Left, image of a representative degranulation event, overlaid onto the corresponding IRM image. Regions defining the degranulation subdomain (R1) and the entire IS (R2) are indicated. Right, differences in mean fluorescence intensity between R1 and R2 at the moment of degranulation are shown for the indicated MTPs.  $N = 52$  for each sample. Error bars denote SEM. P value calculated by unpaired Student's t test. **(E):** Left, image of a representative degranulation event, overlaid onto the corresponding IRM image. Linescans sampling the degranulating (L1) and inactive (L2) domains are indicated. Right, normalized ICAM-1-MTP fluorescence along L1 and L2 at the moment of degranulation (see Methods). The pHluorin-Lamp1 (Degran.) signal along L1 is shown for reference. Error bars denote SEM.  $N = 122$  cells, pooled from two independent experiments. All other data are representative of at least two independent experiments.

ICAM-1-MTP fluorescence along linescans bisecting the degranulation peak. Mean LFA-1 forces reached a local maximum in the  $1\ \mu\text{m}$  diameter region surrounding each event (Fig. 3e), consistent with the idea that mechanically active LFA-1 defines permissive zones for cytotoxic secretion. A degranulation zone of this size would accommodate the approach of a typical lytic granule ( $0.5\text{-}1\ \mu\text{m}$  in diameter)25.

### 3.2.4 Talin is required for LFA-1 mediated force exertion, degranulation, and cytotoxicity

Integrins are coupled to the F-actin cytoskeleton via talin, a mechanosensitive scaffolding protein that is critical for the formation and signaling of integrin adhesions26 (Fig. 4a).

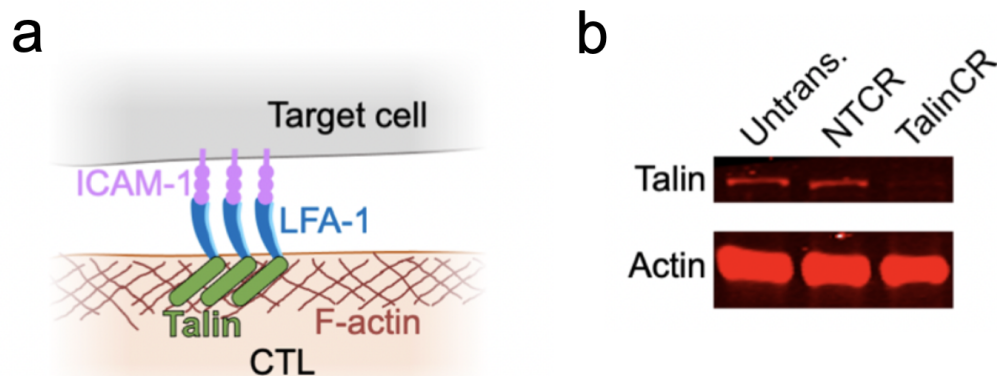


**Figure 3.15:** Talin is required for LFA-1 mediated force exertion, degranulation, and cytotoxicity.

(A): Talin couples ligand-bound integrins to the F-actin cytoskeleton. (B): Immunoblot analysis of talin expression in OT-1 Cas9 CTLs transduced with the indicated gRNAs. Untrans. = untransduced. Actin served as a loading control.

To evaluate the importance of integrin-cytoskeletal linkage for synaptic force exertion, we used CRISPR/Cas9 to deplete talin from OT1 CTLs (Fig. S4a) and then compared the physical output of these cells to that of controls expressing a nontargeting guide RNA. Talin depletion strongly suppressed ICAM-1 pulling on MTP surfaces (Fig. 4b-c) indicative of a profound defect in LFA-1 dependent force exertion. By contrast, pMHC-MTP forces were essentially unchanged (Fig. 4bc and Movie S6), indicating that the mechanical effects of talin were restricted to LFA-1 in this system.

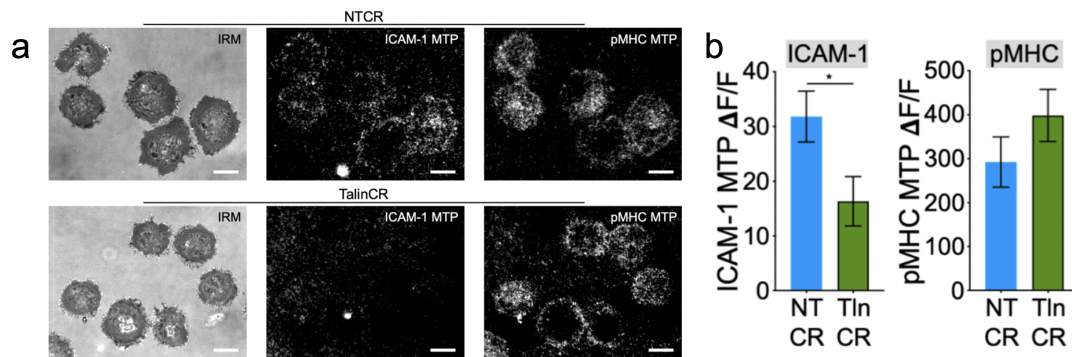


**Figure 3.16:** Talin is required for LFA-1 mediated force exertion.

(A): Representative images showing ligand specific pulling in synapses. Scale bars = 5  $\mu$ m. (c) Mean ICAM-1-MTP (left) and pMHC ( $H2-K^b$ -OVA)-MTP (right) signals, assessed 30 min after the addition of CTLs to the MTP surface.  $N \geq 14$  cells for each sample. Error bars denote SEM (\*)  $P \leq 0.05$ , calculated by unpaired Student's t test.

The selectivity of the talin loss-of-function phenotype allowed us to interrogate the specific role of integrin mechanotransduction in cytotoxicity assays. In cocultures with OVA-loaded RMA-s cells, CTLs lacking talin exhibited sharply reduced degranulation and target cell lysis (Fig. 4de), implying a central role for integrin adhesions in both processes. These loss-of-function phenotypes were not rescued by the application of PMA/Iono (Fig. 4d-e), indicating that they were not caused by impaired T cell activation.

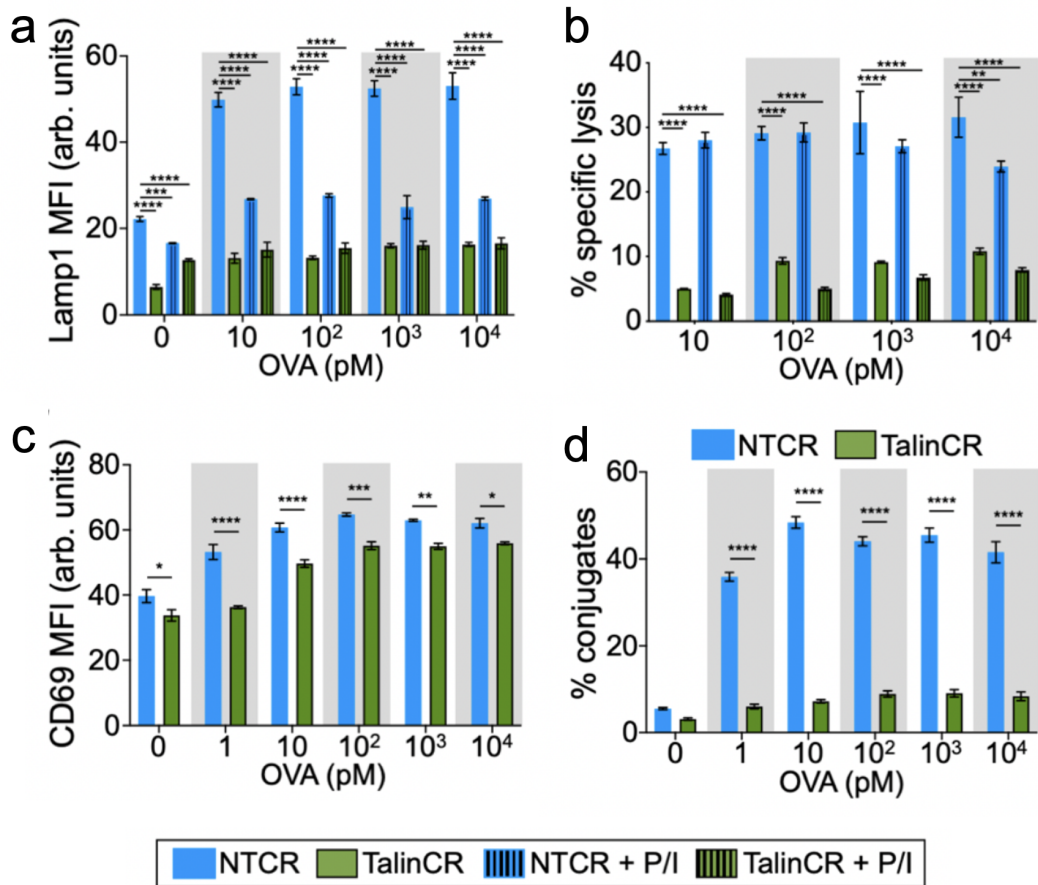


**Figure 3.17:** Talin is required for LFA-1 mediated degranulation, and cytotoxicity.

**(A-D):** OVA-loaded RMA-s target cells were mixed with OT-1 Cas9 CTLs expressing the indicated gRNAs. PMA/Iono was applied to some samples in order to drive TCR independent CTL activation. **(A):** Lamp1 exposure (degranulation), measured 90 min after CTL-target cell mixing. **(B):** Target cell killing, measured 4 h after CTL-target cell mixing. **(C):** CD69 expression, measured 90 min after CTL-target cell mixing. **(D):** Conjugate formation, measured 90 min after CTL-target cell mixing. Data in d-g were derived from technical triplicates. All error bars denote SEM. \*, \*\*, \*\*\*, and \*\*\*\* denote  $P \leq 0.05$ ,  $P \leq 0.01$ ,  $P \leq 0.001$ , and  $P \leq 0.0001$ , calculated by 2way ANOVA (A-D). All data are representative of at least two independent experiments.

Consistent with this interpretation, depletion of talin did not affect TCR-induced MAPK and PI3K signaling (Fig. S4b), and it only modestly suppressed CD69 responses (Fig. 4f). The disproportionately large effect of talin deficiency on cytotoxic secretion was particularly obvious in two-dimensional plots of Lamp1 and CD69 (Fig. S4c), which confirmed that, for a given level of activation, CTLs lacking talin consistently degranulated more weakly than nontargeting controls.

Talin depletion also suppressed CTL-target cell conjugate formation (Fig. 4g), similar to the effects of LFA-1 blockade (Fig. 1g). Collectively, these results support a critical role for talin in LFA-1 dependent IS mechanics and strongly suggest that it is force exertion through LFA-1, rather than the TCR, that imposes spatiotemporal control over CTL degranulation.

### **3.2.5 Talin, but not LFA-1, is required for CTL-mediated killing of B16F10 cells**

Not all cells express LFA-1 ligands, raising the question of whether integrin mechanotransduction controls CTL-mediated killing across a broad spectrum of targets. The capacity of talin deficiency to interrogate integrin function independently of LFA-1 allowed us to address this issue. B16F10 melanoma cells do not express ICAM-1, implying that they cannot engage LFA-1 across the IS (Fig. 5a-b). Nevertheless, they are reasonable targets for OT-1 CTLs, eliciting robust degranulation and cytotoxicity responses in the presence of OVA.

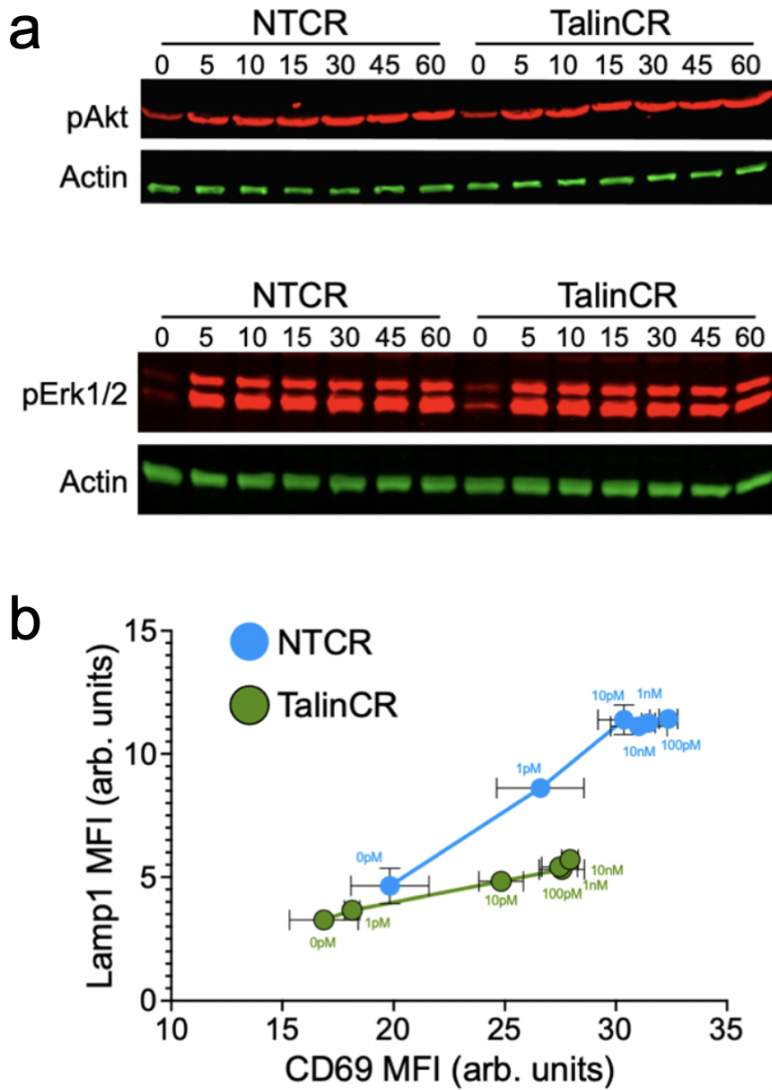


**Figure 3.18:** Talin depletion inhibits degranulation but not early TCR signaling.

(A): OT-1 Cas9 CTLs transduced with the indicated gRNAs were mixed with pMHC (H2-K<sup>b</sup>-OVA) and ICAM-1 coated beads and, at the indicated timepoints, pAKT (top) and pErk1/2 (bottom) were assessed by immunoblot. Actin served as a loading control. (B): 2-dimensional plot correlating degranulation (Lamp1) and T cell activation (CD69), taken from the same data set used to generate Fig. 4d and 4f. Error bars denote SEM. All data are representative of at least two independent experiments.

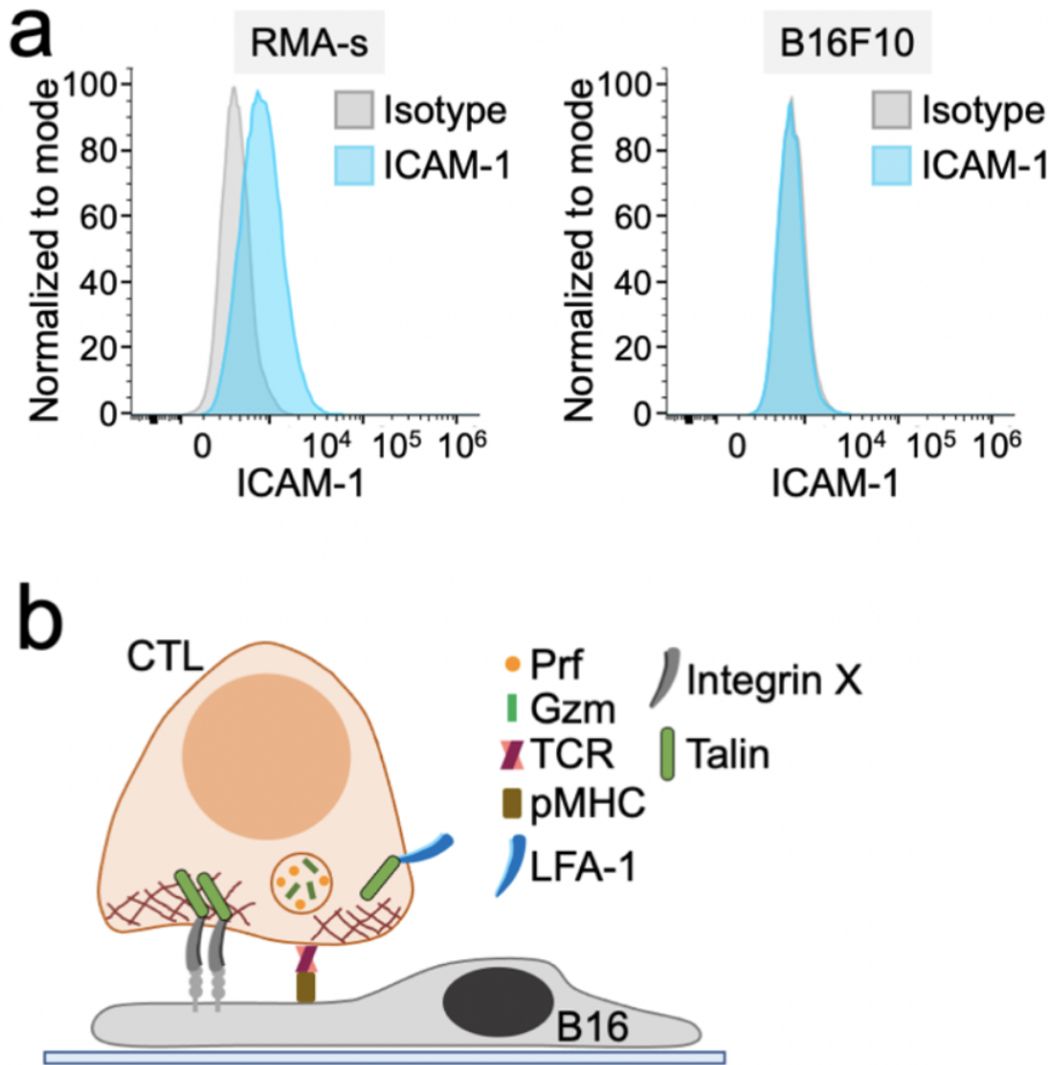


**Figure 3.19:** B16F10 cells do not express ICAM-1.

(A): Representative histograms showing ICAM-1 expression in RMA-s (left) and B16F10 (right) cells. (B) Model of CTL-mediated killing of B16F10 cells that requires both the TCR and an unidentified integrin X.

LFA-1 blockade failed to inhibit either of these responses (Fig. 5c), consistent with the idea that LFA-1 is not involved in the recognition and killing of B16F10 cells. By contrast, talin depletion abrogated both target cell lysis and degranulation (Fig. 5d), strongly suggesting that integrins other than LFA-1 contribute to the killing of ICAM deficient targets. We conclude that integrin-mediated control of cytotoxic secretion is likely to be a general feature of the IS.

### 3.3 Discussion

Taken together, our data suggest a model in which degranulation occurs at permissive secretory subdomains within the IS that are defined by mechanically active integrins (see Figure 1.4). TCR signaling plays critical role in this process by inducing close contact formation and also by triggering  $Ca^{2+}$  influx, which is required for granule fusion<sup>27-29</sup>. In the absence of integrin dependent force exertion, however, TCR signaling alone is insufficient for robust cytotoxic secretion. Indeed, our results imply that one of the major ways that the TCR promotes killing is by locally activating LFA-1 within the IS. This integrin-based model for degranulation both explains our data and is consistent with prior work documenting lytic granule accumulation and perforin release in synaptic subdomains defined by the engagement of adhesive and activating receptors<sup>30, 31</sup>. In the absence of LFA-1 ligands, we speculate that other integrins may assume its licensing role. Indeed, the fact that B16F10 cell killing requires talin, but not LFA-1, strongly implies the existence of alternative integrin activators. CTLs express both VLA-4 ( $\alpha 4\beta 1$ ) and CD103 ( $\alpha E\beta 7$ ), which recognize protein ligands (VCAM-1/2 and E-Cadherin, respectively) found on subsets of potential target cells. CD103 is a particularly interesting candidate, as it has been shown

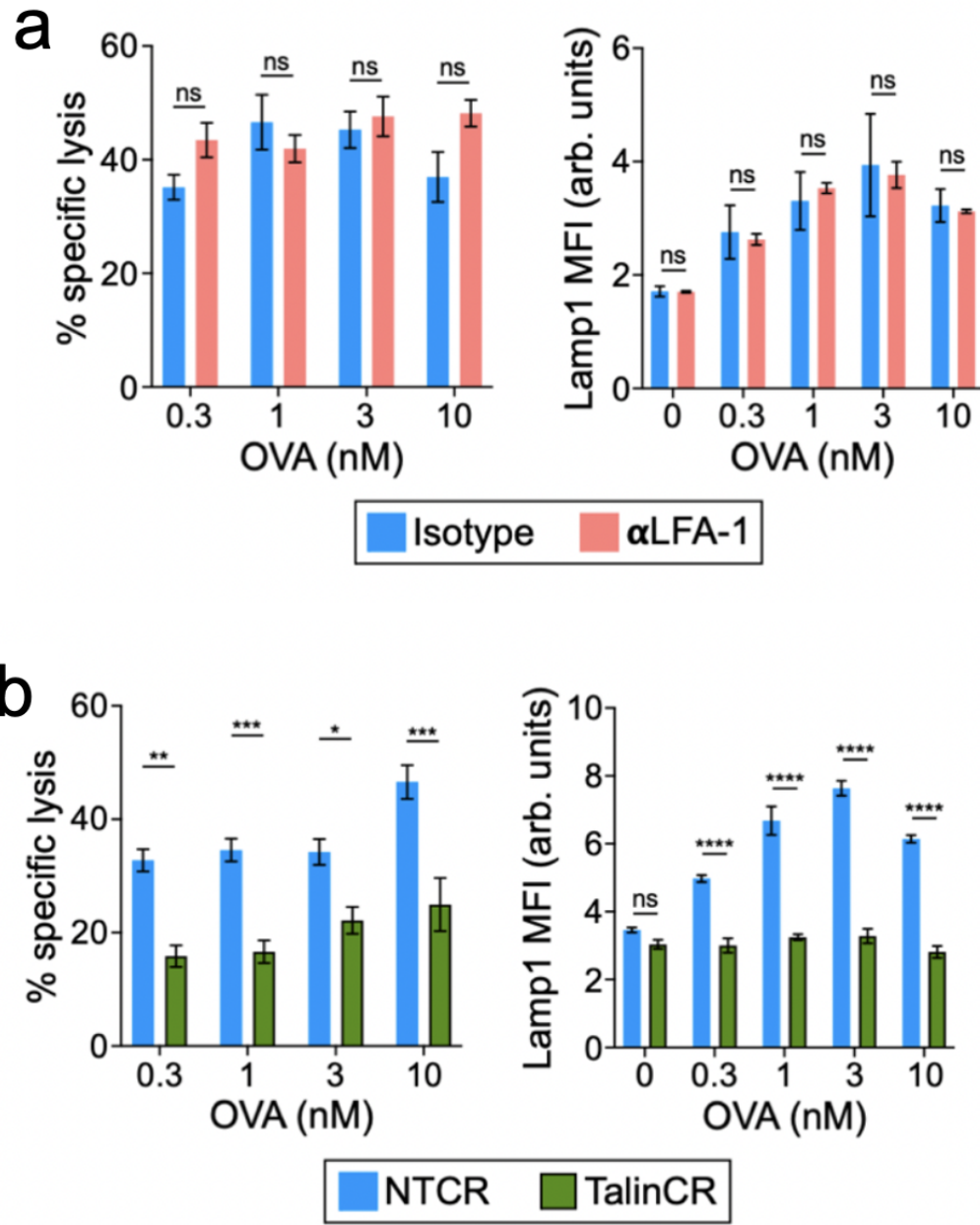


**Figure 3.20:** Talin, but not LFA-1, is required for CTL-mediated killing of B16F10 cells.

(A): OVA-loaded B16F10 target cells were mixed with OT-1 CTLs in the presence of LFA1 blocking antibody ( $\alpha$ LFA-1) or isotype control. Left, specific lysis, measured after 4 h. Right, Lamp1 exposure, measured after 90 min. (d) OVA-loaded B16F10 target cells were mixed with OT-1 Cas9 CTLs transduced with the indicated gRNAs. Left, specific lysis, measured after 4 h. Right, Lamp1 exposure, measured after 90 min. Data in c-d were derived from technical triplicates. All error bars denote SEM. \*, \*\*, and \*\*\* denote  $P \leq 0.05$ ,  $P \leq 0.01$ , and  $P \leq 0.001$ , calculated by 2way ANOVA. All data are representative of at least two independent experiments.

to promote granule polarization and release toward E-Cadherin expressing tumor cells<sup>32</sup>. Previous studies indicate that synaptic forces enhance the pore forming activity of perforin by straining the target membrane<sup>8, 12</sup>. The integrin dependent targeting model described above would be expected to facilitate this process by directing perforin to mechanically active subdomains within the IS. Integrin-mediated mechanotransduction also provides an elegant mechanism for identifying regions of synaptic membrane that are tightly engaged with the target cell, where extensive mechanical coupling between directly opposing membranes would enable the CTL to “feel” the presence of the target by pushing or pulling against it. Guiding degranulation to these regions of close apposition would ensure that only the target is exposed to perforin and granzyme, thereby limiting damage to innocent bystander cells. Hence, using mechanically active integrins to license cytotoxic secretion likely promotes both the potency and the specificity of killing responses.

The centrosome and its associated microtubules are key determinants of lytic granule localization<sup>2, 4</sup>. Target recognition induces the trafficking of lytic granules along microtubules toward the centrosome, which concomitantly reorients to a position just beneath the center of the IS, thereby positioning granules close to the synaptic membrane. Although this mechanism is thought to promote polarized secretion, studies from multiple labs indicate that it is dispensable for the process<sup>5-7</sup>. Indeed, we have found that CTLs lacking a functional centrosome or even the entire microtubule cytoskeleton retain the capacity to release perforin and granzyme directionally into the IS<sup>5</sup>. The integrin licensing model described here explains these prior observations by providing an alternative targeting mechanism. That being said, our results do not exclude an important role for the centrosome and microtubules in enhancing the speed and efficiency

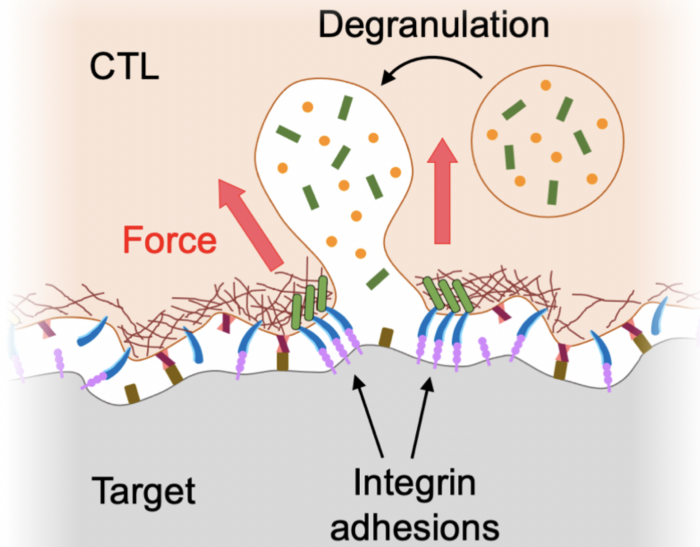


**Figure 3.21:** Mechanical licensing of degranulation by integrin adhesions.

Lytic granules fuse within synaptic subdomains defined by ligand-bound integrins under tension.

of cytotoxic secretion. Indeed, we have shown that microtubule depletion, while failing to disrupt the directionality of degranulation, nevertheless profoundly reduces the magnitude of the secretory response. Accordingly, we favor a model in which centrosome polarization delivers granules into the IS neighborhood, at which point their site of fusion is dictated by integrin licensing. The coupling of mechanical input to secretory output is unlikely to be unique to the cytotoxic IS. Indeed, one can imagine analogous mechanisms regulating other mechanically active processes, like phagocytosis and cell-cell fusion, that involve secretion and/or polarized membrane remodeling. We anticipate that biophysical analysis of systems like these will further illuminate the scope and functional relevance of mechano-secretory crosstalk in communicative cell-cell interactions.

## **3.4 Materials and Methods**

### **3.4.1 Constructs**

The retroviral expression construct for pHluorin-Lamp1 has been described<sup>20</sup>. A CRISPR gRNA construct targeting talin was prepared according to a published protocol<sup>33</sup> using the following targeting sequence: 5'-GCTTGGCTTGAGGCCAGT-3'. A non-targeting control construct was also prepared using the sequence 5'-GCGAGGTATTGGCTCCGCG-3'. After PCR amplification, DNA fragments encoding these guide sequences were subcloned into the pMRIG vector using the BamHI and MfeI restriction sites.

### **3.4.2 Proteins**

Class I MHC proteins (H2-*K<sup>b</sup>* and H2-*D<sup>b</sup>*) were overexpressed in E. Coli, purified as inclusion bodies, and refolded by rapid dilution in the presence of  $\beta$ 2-microglobulin and either OVA (for H2-*K<sup>b</sup>*) or KAVYDFATL (KAVY, for H2-*D<sup>b</sup>*). Monomeric MHC proteins were biotinylated using the BirA enzyme and purified by size exclusion chromatography. The extracellular domain of mouse ICAM-1 (a.a. 28-485, polyhistidine-tagged) was expressed by baculoviral infection of Hi-5 cells and purified by  $Ni^{2+}$  chromatography. After BirA-mediated biotinylation, the ICAM-1 was further purified by size exclusion.

### **3.4.3 Cells**

The animal protocols used for this study were approved by the Institutional Animal Care and Use Committee of Memorial Sloan Kettering Cancer Center. Primary CTL blasts were prepared by pulsing splenocytes from an OT1  $\alpha\beta$  TCR transgenic mice with 100 nM OVA in RPMI medium containing 10% (vol/vol) FCS. Cells were supplemented with 30 IU/mL IL-2 after 24 h and were split as needed in RPMI medium containing 10% (vol/vol) FCS and IL-2. RMA-s cells were maintained in RPMI containing 10% (vol/vol) FCS. B16F10 cells were maintained in DMEM medium containing 10% (vol/vol) FCS.

### **3.4.4 Traction force microscopy**

Arrays of PDMS (Sylgard 184; Dow Corning) micropillars (0.7  $\mu\text{m}$  in diameter, 6  $\mu\text{m}$  in height, spaced hexagonally with a 2- $\mu\text{m}$  center-to-center distance) were cast onto glass coverslips using the inverse PDMS mold method<sup>34</sup>. After an ethanol wash and stepwise exchange into phosphate buffered saline (PBS), pillars were stained with fluorescently labeled streptavidin (20  $\mu\text{g}/\text{mL}$  Alexa Fluor 647, Thermo Fisher Scientific) for 2 hours at room temperature. Following additional PBS washes, the arrays were incubated with biotinylated H2-K<sup>b</sup>-OVA and ICAM-1 (10  $\mu\text{g}/\text{mL}$  each) overnight at 4°C. The pillars were then washed into RPMI containing 5% (v/v) FCS and lacking phenol red for imaging. T cells stained with Alexa Fluor 488-labeled anti-CD45.2 Fab (clone 104-2) were then added to the arrays and imaged using an inverted fluorescence microscope (Olympus IX-81) fitted with a 100 $\times$  objective lens and a mercury lamp for excitation. Images

in the 488-nm (CTLs) and 647-nm (pillars) channels were collected every 15 s using MetaMorph software.

### **3.4.5 Antibody blockade and pharmacolog. activation/inhibition**

To assess the importance of LFA-1, CTLs were pre-incubated with LFA-1 blocking antibody (20 µg/mL, Clone M17/4, BioXCell) or an IgG2ak isotype control antibody (20 µg/mL, Clone RTK2758, BioLegend) at 37°C for 5 minutes before the addition of target cells/stimulatory beads. The final concentration of antibodies during the assay was 10 µg/mL. To induce T cell activation independently of the TCR, CTLs were pre-incubated with phorbol myristate acetate (PMA, 20 ng/mL, Sigma Aldrich) and the  $Ca^{2+}$  ionophore A23187 (2 µM, Tocris Bioscience) at 37°C for 5 minutes before the addition of target cells/stimulatory beads, yielding final concentrations of 10 ng/mL PMA and 1 µM A23187.

### **3.4.6 Retroviral transduction**

Phoenix E cells were transfected with expression vectors and packaging plasmids using the calcium phosphate method. Ecotropic viral supernatants were collected after 48 h at 37°C and added to  $1.5 \times 10^6$  OT-1 blasts 24 h after primary peptide stimulation. Mixtures were centrifuged at 1400g in the presence of polybrene (4 µg/mL) at 35°C, after which the cells were split 1:3 in RPMI medium containing 10% (vol/vol) FCS and 30 IU/mL IL-2 and allowed to grow for an additional 4-6 days.

### 3.4.7 Functional assays

To measure cytotoxicity, RMA-s target cells were labeled with CellTrace Violet (CTV), loaded with increasing concentrations of OVA, and mixed 3:1 with PKH26-stained OT-1 CTLs in a 96-well V-bottomed plate. Specific lysis of CTV+ target cells was determined by flow cytometry after 4 h at 37°C. To quantify degranulation, OT-1 CTLs were mixed with RMA-s target cells as described above and incubated at 37°C for 90 min in the presence of eFluor 660-labeled anti-Lamp1 (clone eBio1D4B; eBioscience). Cells were then stained with FITC-labeled anti-CD69 (clone) and subjected to flow cytometric analysis to quantify Lamp1 and CD69 staining. To measure conjugate formation, labeled OT-1 CTLs and RMA-s targets were mixed 1:1, lightly centrifuged (100g) to encourage cell contact, and incubated 20 min at 37°C. Cells were then resuspended in the presence of 2% paraformaldehyde, washed in fluorescence-activated cell sorting buffer (PBS + 4% FCS), and analyzed by flow cytometry. Conjugate formation was quantified as (PKH26+CTV+)/(PKH26+). For B16F10 killing assays, B16F10 targets were cultured overnight on fibronectin and then pulsed with varying concentrations of OVA for 2 hours. OT1 CTLs were added at an 8:1 E:T ratio and incubated for 3-4 hours at 37°C in RPMI medium supplemented with IL-2 (30 IU/mL). Target cell death was quantified with an LDH (lactate dehydrogenase) cytotoxicity assay kit (Clontech) using the manufacturer's recommended protocol. To measure intracellular granzyme B depletion, OT1 CTLs were mixed 1:3 with OVA-loaded RMA-s cells and incubated for 4-6 hours at 37°C. Intracellular granzyme B levels were then measured by flow cytometry after fixation, permeabilization, and staining with Alexa 647 labeled anti-granzyme B (clone GRB11, Biolegend). All functional assays were performed in triplicate. To quantify ICAM-1 expression, RMA-s or B16F10 cells were stained with a fluorescently labeled anti-ICAM-1

antibody CD54 (Clone YN1/1.7.4, BioLegend) or isotype control antibody (Clone RTK4530, Biolegend).

### 3.4.8 CTL activation with stimulatory beads

Streptavidin-conjugated polystyrene beads (Spherotech) were coated with 1  $\mu\text{g}/\text{mL}$  biotinylated ICAM-1 and/or various concentrations of biotinylated H<sub>2</sub>-K<sup>b</sup>-OVA. Nonstimulatory pMHC (H<sub>2</sub>-D<sup>b</sup>) was used if necessary to adjust the total biotinylated protein concentration of each mixture 2  $\mu\text{g}/\text{mL}$ . After overnight incubation at 4°C, excess unbound protein was washed out and the beads were transferred into RPMI medium containing 10% (vol/vol) FCS (+/- phenol red) for use in experiments. For immunoblot analysis of signaling, beads were mixed with OT-1 CTLs at a 1:1 ratio. For functional studies (e.g. degranulation), the CTL to bead ratio was 1:3. For 2 bead stimulation (Fig. 2a-c), Nile Red and Purple streptavidin beads were coated as described above with H-2Kb-OVA and ICAM-1 in either cis or trans configurations. H-2Db was used to fill empty spaces in the trans configuration and also to generate “dummy” coated beads. In each experimental condition, CTLs were mixed with two kinds of beads at a 1:3:3 ratio. Degranulation and CD69 upregulation were quantified by flow cytometry as described above.

### 3.4.9 Micropatterning experiments

PDMS stamps for imprinting 2  $\mu\text{m}$  in diameter spots in 10  $\mu\text{m}$  center-to-center square arrays were prepared using microfabricated silicon masters as

previously described<sup>19</sup>. Stamps were washed in ethanol and water, then coated with fluorescently-labeled streptavidin (10 µg/mL Alexa Fluor 647, Thermo Fisher Scientific) for 1 hour at room temperature. After PBS washing to remove excess proteins, the stamps were pressed onto 35 mm glass coverslips (# 1.5) to transfer the streptavidin. Coverslips were then incubated with the following unbiotinylated proteins to coat the spaces between streptavidin dots: (1) ICAM-spot – 10 µg/mL H2-K<sup>b</sup>-OVA, (2) Antigen-spot – 10 µg/mL ICAM-1, (3) Dual-spot – 5% BSA, (4) ICAM-spot with anti-CD3 background – 10 µg/mL anti-CD3 antibody (Clone 145-2C11, eBioScience), (5) Anti-CD3-spot – 10 µg/mL ICAM-1, and (6) control – 10 µg/mL unlabeled streptavidin. After 1 h at room temperature, coverslips were rinsed with PBS 3 times to wash away uncoated protein and blocked with 5% BSA at room temperature for 1 hour before another round of PBS washes. Coverslips were then incubated with the following biotinylated proteins to load the streptavidin: (1) ICAM-spot – 2 µg/mL ICAM-1, (2) Antigen-spot – 2 µg/mL H2-K<sup>b</sup>-OVA, (3) Dual-spot – 2 µg/mL H2-K<sup>b</sup>-OVA and 2 µg/mL ICAM-1, (4) ICAM-spot with anti-CD3 background – 2 µg/mL ICAM-1, (5) Anti-CD3-spot – 2 µg/mL anti-CD3 antibody (Clone 145-2C11, eBioScience), and (6) control – 2 µg/mL H2-K<sup>b</sup>-OVA and 2 µg/mL ICAM-1. After 1 h at room temperature, the surfaces were washed into RPMI containing 5% (v/v) fetal calf serum (FCS) and lacking phenol red for imaging. Cells were then added and imaging performed using either a Leica SP5-inverted confocal laser scanning microscope fitted with 488 nm, 563 nm, and 647 nm lasers, or a Leica SP8-inverted confocal laser scanning microscope fitted with a white light laser. In general, samples were imaged every 15 s for 30 min.

### **3.4.10 $Ca^{2+}$ imaging**

CTLs were loaded with 5  $\mu$ g/mL Fura2-AM (ThermoFisher Scientific), washed, and then imaged on stimulatory glass surfaces coated with H2-K<sup>b</sup>-OVA and ICAM-1 as previously described<sup>36</sup>. 340 nm and 380 nm excitation images were acquired every 30 seconds for 30 min using a 20x objective lens (Olympus).

### **3.4.11 DNA hairpins**

Name Sequence (5' to 3')

A21B - /5AmMC6/- CGC ATC TGT GCG GTA TTT CAC TTT - /3Bio/

Quencher strand - /5DBCON/- TTT GCT GGG CTA CGT GGC GCT CTT - /3BHQ\_2/

Hairpin strand - GTG AAA TAC CGC ACA GAT GCG TTT GTA TAA ATG  
TTT TTT TCA TTT ATA CTT TAA GAG CGC CAC GTA GCC CAG C

A mixture of oligo A21B (10 nmol) and excess Cy3B-NHS ester or Atto647N-NHS ester (50  $\mu$ g) in 0.1 M sodium bicarbonate solution was allowed to react at room temperature overnight. The derivatized oligo was then purified by gel filtration and reversed phase HPLC.

### 3.4.12 MTP surface preparation and imaging

Glass coverslips (# 1.5H, Ibidi) were sonicated in MilliQ H<sub>2</sub>O and ethanol, rinsed in H<sub>2</sub>O, and then immersed in piranha solution (3:1 sulfuric acid:H<sub>2</sub>O<sub>2</sub>) for 30 min to remove organic residues and activate hydroxyl groups on the glass. Subsequently, the cleaned substrates were rinsed with more H<sub>2</sub>O and ethanol and then transferred to a 200 mL beaker containing 3% APTES in ethanol for 1 h, washed with ethanol and baked at 100 °C for 30 min. After cooling, slides were mounted to 6-channel microfluidic cells (Sticky-Slide VI 0.4, ibidi). To each channel, 50 μL of 10 mg/mL of NHS-PEG4-azide in 0.1 M NaHCO<sub>3</sub> (pH = 9) was added and incubated for 1 h. The channels were then washed with H<sub>2</sub>O, blocked with 0.1% BSA in PBS for 30 min, and washed with PBS. 50 μL of PBS solution was retained inside the channel after washing to prevent drying. Subsequently, the hairpin tension probes were assembled in 1M NaCl by mixing the Atto647N labeled A21B strand (220 nM), quencher strand (220 nM) and hairpin strand (200 nM) in the ratio of 1.1: 1.1:1. The mixture was heat annealed by incubating at 95°C for 5 min, followed by cool down to 25°C over 30 min. 50 μL of the assembled probe was added to the channels (total volume = 100 μL) and incubated overnight at room temperature. The following day, unbound DNA probes were removed by PBS wash. Then, 10 μg/mL of streptavidin was incubated in the channels for 45 min at room temperature. The surfaces were cleaned with PBS and incubated with 5 μg/mL of biotinylated pMHC ligand for 45 min at room temperature. After PBS washing, a second DNA tension probe (Cy3B labeled) was assembled and attached as described above, followed by loading with streptavidin and 5 μg/mL of biotinylated ICAM-1. Monomeric ICAM-1 was used for pHluorin-Lamp1 experiments (Fig. 3) and dimeric Fc-ICAM1 for talin-KO experiments (Fig. 4). After washing off the unbound ICAM-1

protein, surfaces were rinsed in complete RPMI (no phenol red, supplemented with IL-2) in preparation for imaging with CTLs. MTP imaging was performed on a Nikon Eclipse Ti microscope attached to an electron multiplying charge coupled device (EMCCD; Photometrics), an Intensilight epifluorescence source (Nikon), a CFI Apo 100x (NA 1.49) objective lens (Nikon), and a TIRF launcher with 488 nm, 561 nm, and 638 nm laser lines. In general, IRM, 488 nm, 561 nm, and 638 nm images were collected every 20 s for 30 min. TIRF illumination was used to image pHluorin-Lamp1 and epifluorescence to image the MTPs.

### 3.4.13 Imaging analysis

Imaging data were analyzed using SlideBook (3i), Imaris (Bitplane), Excel (Microsoft), Prism (GraphPad), and Python in Jupyter Notebook37.  $Ca^{2+}$  signaling was quantified by determining the mean Fura2 ratio for all cells in the imaging field using a mask thresholded on the 340 nm excitation signal. To quantify force exertion in traction force microscopy experiments, custom MATLAB scripts were used to extract pillar displacements from the imaging data, which were then converted into force vectors. To measure the distance between degranulation events and the closest streptavidin spot on micropatterned surfaces, pHluorin-Lamp1 and streptavidin Alexa Fluor 647 signals were converted into Imaris spot constructs using Imaris scripts. The distances ( $\mu m$ ) between each pHluorin-Lamp1 signal of interest and the closest streptavidin spot within the synaptic boundary of the CTL were then determined using the Imaris ‘Shortest Distance’ function. The expected distance between randomly placed degranulation events and ligand spots was determined in silico. First, the unit cell of the micropattern was modeled as a  $5 \mu m \times 5 \mu m$  square with a quarter-circle representing the stamped

protein at one corner. Then, the unit square was divided into  $1 \times 10^6$  points (evenly sampling 10-nm spaces in both x and y), and the Euclidean distance of each point to the stamped protein corner was calculated. The mean distance of this distribution is  $3.8266 \mu\text{m}$ . MTP data were analyzed by comparing the mean fluorescence intensity of each MTP within the  $2 \mu\text{m} \times 2 \mu\text{m}$  box centered on a pHluorin-Lamp1 signal of interest with the mean fluorescence intensity of the MTP within the entire IS, defined by threshold masking of IRM images (Fig. 3d). Linescan analysis of ICAM-1-MTP fluorescence at degranulation sites (Fig. 3e) was performed by generating a series of  $2 \mu\text{m}$  linescans bisecting degranulation events of interest. The linescan intensities were aligned around the degranulation, averaged over each pixel, and normalized per linescan. An analogous set of control linescans, collected from parts of the IS lacking degranulation events, were processed in parallel using the same scripts.

### 3.4.14 Proliferation Assay

Day 7 OT-1 CTLs were stained with CellTrace Violet at room temperature for 20 min, washed in serum containing medium, and then incubated with irradiated OVA-loaded C57BL/6 splenocytes ( $0.5 \times 10^6$  CTL with  $4.0 \times 10^6$  splenocytes) the presence of  $10 \mu\text{g/mL}$  anti-LFA-1 or an isotype control antibody. Subsequent dilution of CellTrace Violet was assessed by flow cytometry.

### **3.4.15 Immunoblot**

0.2-1  $\times$  10<sup>6</sup> CTLs were lysed using cold cell lysis buffer containing 50 mM TrisHCl, 0.15 M NaCl, 1 mM EDTA, 1% NP-40 and 0.25% sodium deoxycholate. Suppression of talin 1 was confirmed using an anti-talin 1 antibody (clone 8D4, Abcam). Actin served as a loading control (clone AC-15, Sigma). For signaling assays, serum and IL-2 starved OT1 CTLs were incubated with streptavidin polystyrene beads (Spherotech) coated with H2-K<sup>b</sup>-OVA and ICAM-1 at a 1:1 ratio for various times at 37°C and immediately lysed in 2x cold lysis buffer containing phosphatase inhibitors (1 mM NaF and 0.1 mM Na3VO4) and protease inhibitors (cOmplete mini cocktail, EDTAfree, Roche). Activation of PI3K and MAP kinase signaling was assessed by immunoblot for pAkt (Phospho-Akt (Ser473) Ab; Cell Signaling Technology) and pErk1/2 (Phospho-Thr202/ Tyr204; clone D13.14.4E; Cell Signaling Technology).

## CHAPTER 4

## DISCUSSION

For my doctoral work, I performed research investigating the mechanoregulation of cytotoxic T lymphocyte killing. Together, we found that CTLs form synaptic actin protrusions against target cells [24]. This act sensitizes the target cell to perforin lysis and granzyme entry, heightening the overall cytotoxic effector response. This potentiation is molecularly controlled by the actin nucleation promoting factors WASP and WAVE2, which are concentrically organized (from the center to the periphery, respectively). WASP promotes central actin protrusions associated with lytic granule fusion and content release, while WAVE2 is linked with peripheral actin protrusions and robust conjugate formation. Phenotypically, the increased application of force against targets is associated with an overall better effector response. This biomechanical force-effector relationship again appears in our model of degranulation, in which T cells use mechanical signals via integrins to home their lytic granules towards synaptic 'hotspots'. These synaptic sites of granule fusion are verified to be foreign and accordingly sensitized to perforin.

A number of outstanding questions surrounding T cell mechanobiology remain open for investigation. A discussion of some of these questions and how the results of my thesis work informs these questions follows. These questions remain unanswered today for either knowledge or technically-based reasons, but they will surely be answered in due time.

## **4.1 On the interfacing of mechanical and biochemical signaling planes**

- Different antigen sensitivities / valency or sensitivity of integrins? Minimal number needed for degranulation?
- Speculate on particular molecules or signaling axes
- How do integrin focal adhesions signal to fusion machinery? How do integrins speak to the centrosome?
- Are there local lipid domains at regions of integrin mechanosensitivity? <https://rupress.org/jcb/article/221/1/e202112057/212925/Thank-ORP9-for-FFAT-With-endosomal-ORP10-it-s>

## **4.2 On CTL force dynamics**

It would be interesting to investigate dynamics of synaptic force exertion in a single CTL against a target cell. In particular, one wonders if the CTL at first pass deploys a standard range of force exertion and protrusion-type or cellular structure (in a "probing phase"), and then must dynamically change its range of force exertion or arsenal of structures for force exertion according to local bistructural architecture (i.e. what is the lifetime force action of a standard CTL encounter?). Certainly these events are correspondingly influenced by the signaling molecules present at the synapse, each of which live their own biophysical lives by mere virtue of their presence. Answering such questions would require direct interrogation of a live CTL-target cell synapse. Previous

technologies for measuring membrane tension include atomic force microscopy or an optical trap - but both remain insufficiently precise to monitor real-time *in vitro* or *in vivo* synapse dynamics. Certain fluorescence-based technologies have been recently been developed in order to measure synapse dynamics that ignore restrictive planar geometries [31]. Combined with fluorescent probes, the use of these microparticles could elucidate "phases" of the T cell physical response as it (putatively) probes, adheres, degranulates, kills, and releases, the target cell.

Thinking outside the context of single-T cell force exertions, it would be fascinating to investigate the host CTL-ome at large, if certain "battalions" or "legions" of CTLs exist, organized according to their physical strengths and effector capabilities. Certainly a reasonable first-pass method of organization is expression levels of certain effector genes and molecules (e.g. *Prf*, *Grzb*, *Ifng*), but these measures obviously omit the mechanoregulation of these molecules and thus miss their effects in totality. One would require experimental techniques capable of not only measuring single-cell T cell force exertion *en masse*, but also the possible swarm behavior of responding T cells in which an initial "less capable" group of T cells is replaced by stronger effector cells (or weaker, in a "clean up" phase). Certain molecular perturbation platforms that are designed to measure CRISPR-based perturbations at the protein level [32] come closer to characterizing all of the effects that a molecular perturbation truly encompasses. Other platforms for monitoring infiltrating immune cells into locally perturbed regions of the tumor microenvironment also exist [33]. One could imagine choosing a tumor system that has been spatially perturbed heterogeneously for known cytoskeletal/cell stiffness molecules and investigate how T cells of well-characterized strengths segregate (and presumably kill). Characterizing T

cell swarm or group behavior would be a massive undertaking that would take many years to perform.

Many of the experiments conducted in order to complete this doctoral thesis were performed using *in vitro* systems. These systems were designed to interrogate force activity by holding the force threshold constant (e.g. micropillars, DNA membrane tension probes), while observing the cell's force activity in time. While these arrangements are useful for ease of investigation, holding constant a variable as broad as the force threshold creates major scientific blind spots even in real-time studies (much less bulk studies via co-culture assays). This is true particularly in studies focused on the effector cell, in which the arrangement ignores half of the cellular conversation: the target cell [34]. The target cell is capable of dynamically responding to the effector cell's efforts to kill (presumably in a cooperative or antagonistic manner), which is entirely neglected in these experimental systems.

### **4.3 On the mechanical licensing of cellular activities**

- Importance of mechanobiology in developmental biology
- Other speculative integrins
- Other speculative functions that mechanical activity can contribute to

## **4.4 On mechanical signaling of T cell subsets and engineered T cells**

Given how energy intensive

- Exhausted T cells
- Speculation on the role of mechanobiology in engineered T cells
- Other immune cell types

## **4.5 On the limitations of *in vitro*-based investigations**

Of course, many of these experiments were also performed using the OT-I transgene system.

Ideas:

- Compare to neuronal firing

- "Many immune receptors are mechanosensitive"

Formats:

- Based on this paper, it seems plausible that...

- It remains unknown

## BIBLIOGRAPHY

- [1] Martin Heidegger. *Sein und Zeit*. pages 114–129, 1927.
- [2] Uzma Alam. Immunity: The Immune Response to Infectious and Inflammatory Disease. *The Yale Journal of Biology and Medicine*, 80(3):137–137, 2007.
- [3] Ed Palmer. Negative selection - Clearing out the bad apples from the T-cell repertoire. *Nature Reviews Immunology*, 3(5):383–391, 2003.
- [4] Rebecca J. Brownlie and Rose Zamoyska. T cell receptor signalling networks: branched, diversified and bounded. *Nature Reviews Immunology* 2013 13:4, 13(4):257–269, mar 2013.
- [5] E J Quann, E Merino, T Furuta, and M Huse. Localized diacylglycerol drives the polarization of the microtubule-organizing center in T cells. *Nat Immunol*, 10(6):627–635, 2009.
- [6] Jane C. Stinchcombe, Endre Majorovits, Giovanna Bossi, Stephen Fuller, and Gillian M. Griffiths. Centrosome polarization delivers secretory granules to the immunological synapse. *Nature*, 443(7110):462–465, 2006.
- [7] Andrea Maul-Pavicic, Samuel C.C. Chiang, Anne Rensing-Ehl, Birthe Jessen, Cyril Fauriat, Stephanie M. Wood, Sebastian Sjöqvist, Markus Hufnagel, Ilka Schulze, Thilo Bass, Wolfgang W. Schamel, Sebastian Fuchs, Hanspeter Pircher, Christie Ann McCarl, Katsuhiko Mikoshiba, Klaus Schwarz, Stefan Feske, Yenan T. Bryceson, and Stephan Ehl. ORAI1-mediated calcium influx is required for human cytotoxic lymphocyte degranulation and target cell lysis. *Proceedings of the National Academy of Sciences of the United States of America*, 108(8):3324–3329, 2011.
- [8] Alex T. Ritter, Yukako Asano, Jane C. Stinchcombe, N. M G Dieckmann, Bi Chang Chen, C. Gawden-Bone, Schuyler van Engelenburg, Wesley Legant, Liang Gao, Michael W. Davidson, Eric Betzig, Jennifer Lippincott-Schwartz, and Gillian M. Griffiths. Actin Depletion Initiates Events Leading to Granule Secretion at the Immunological Synapse. *Immunity*, 42(5):864–876, 2015.
- [9] Yan Yu, Alexander A. Smoligovets, and Jay T. Groves. Modulation of t cell signaling by the actin cytoskeleton. *Journal of Cell Science*, 126(5):1049–1058, 2013.

- [10] Audrey Le Floc'h, Yoshihiko Tanaka, Niels S Bantilan, Guillaume Voisinne, Grégoire Altan-Bonnet, Yoshinori Fukui, and Morgan Huse. Annular PIP3 accumulation controls actin architecture and modulates cytotoxicity at the immunological synapse. *The Journal of experimental medicine*, 210(12):2721–37, 2013.
- [11] Emmanuel Derivery and Alexis Gautreau. Generation of branched actin networks: Assembly and regulation of the N-WASP and WAVE molecular machines. *BioEssays*, 32(2):119–131, 2010.
- [12] Karon Abe, Kent L. Rossman, Betty Liu, Kimberly D. Ritola, Derek Chiang, Sharon L. Campbell, Keith Burridge, and Channing J. Der. Vav2 is an activator of Cdc42, Rac1, and RhoA. *Journal of Biological Chemistry*, 275(14):10141–10149, 2000.
- [13] Wendell A. Lim Kenneth E. Prehoda, Jessica A. Scott, R. Dyche Mullins. Integration of Multiple Signals Through Cooperative Regulation of the N-WASP-Arp2/3 Complex. *Integration of Multiple Signals Through Cooperative Regulation of the N-WASP-Arp2/3 Complex*, 45(October), 2000.
- [14] Louise Weston, Amanda S. Coutts, and Nicholas B. La Thangué. Actin nucleators in the nucleus: An emerging theme. *Journal of Cell Science*, 125(15):3519–3527, 2012.
- [15] Michael L. Dustin and Eric O. Long. Cytotoxic immunological synapses. *Immunological Reviews*, 235(1):24–34, 2010.
- [16] Jane C. Stinchcombe and Gillian M. Griffiths. Secretory Mechanisms in Cell-Mediated Cytotoxicity. <http://dx.doi.org/10.1146/annurev.cellbio.23.090506.123521>, 23:495–517, oct 2007.
- [17] Ruby H P Law, Natalya Lukyanova, Ilia Voskoboinik, Tom T Caradoc-Davies, Katherine Baran, Michelle a Dunstone, Michael E D'Angelo, Elena V Orlova, Fasséli Coulibaly, Sandra Verschoor, Kylie a Browne, Annette Ciccone, Michael J Kuiper, Phillip I Bird, Joseph a Trapani, Helen R Saibil, and James C Whisstock. The structural basis for membrane binding and pore formation by lymphocyte perforin. *Nature*, 468(7322):447–51, 2010.
- [18] Adam N R Cartwright, Jeremy Griggs, and Daniel M Davis. The immune synapse clears and excludes molecules above a size threshold. *Nature Communications*, 5:5479, 2014.

- [19] Dennis Keefe, Lianfa Shi, Stefan Feske, Ramiro Massol, Francisco Navarro, Tomas Kirchhausen, and Judy Lieberman. Perforin triggers a plasma membrane-repair response that facilitates CTL induction of apoptosis. *Immunity*, 23(3):249–262, 2005.
- [20] Yovan Sanchez-Ruiz, Salvatore Valitutti, and Loic Dupre. Stepwise Maturation of Lytic Granules during Differentiation and Activation of Human CD8+ T Lymphocytes. *PLOS ONE*, 6(11):e27057, nov 2011.
- [21] Jerome Thiery and Judy Lieberman. Perforin: A Key Pore-Forming Protein for Immune Control of Viruses and Cancer. *Sub-Cellular Biochemistry*, 80:197–220, may 2014.
- [22] Dennis Keefe, Lianfa Shi, Stefan Feske, Ramiro Massol, Francisco Navarro, Tomas Kirchhausen, and Judy Lieberman. Perforin triggers a plasma membrane-repair response that facilitates CTL induction of apoptosis. *Immunity*, 23(3):249–262, 2005.
- [23] Gregory D. Rak, Emily M. Mace, Pinaki P. Banerjee, Tatyana Svitkina, and Jordan S. Orange. Natural Killer cell lytic granule secretion occurs through a pervasive actin network at the immune synapse. *PLoS Biology*, 9(9), 2011.
- [24] Fella Tamzalit, Mitchell S Wang, Weiyang Jin, Vitaly Boyko, John M Heddleston, Charles T Black, Lance C Kam, and Morgan Huse. Interfacial actin protrusions mechanically potentiate killing by cytotoxic T cells. *Science Immunology*, 5445(March):443309, 2018.
- [25] Roshni Basu, Benjamin M. Whitlock, Julien Husson, Audrey Le Floc'h, Weiyang Jin, Alon Oyler-Yaniv, Farokh Dotiwala, Gregory Giannone, Claire Hivroz, Nicolas Biais, Judy Lieberman, Lance C. Kam, and Morgan Huse. Cytotoxic T Cells Use Mechanical Force to Potentiate Target Cell Killing. *Cell*, 165(1):100–110, 2016.
- [26] Baoyu Liu, Wei Chen, Brian D. Evavold, and Cheng Zhu. Accumulation of dynamic catch bonds between TCR and agonist peptide-MHC triggers T cell signaling. *Cell*, 157(2):357–368, 2014.
- [27] Facundo D. Batista and Michael L. Dustin. Cell: Cell interactions in the immune system. *Immunological Reviews*, 251(1):7–12, jan 2013.
- [28] Katarzyna I. Jankowska, Edward K. Williamson, Nathan H. Roy, Daniel Blumenthal, Vidhi Chandra, Tobias Baumgart, and Janis K. Burkhardt. Inte-

- grins modulate T cell receptor signaling by constraining actin flow at the immunological synapse. *Frontiers in Immunology*, 9(JAN):1–19, 2018.
- [29] Yang Wang, Dan Li, Roza Nurieva, Justin Yang, Mehmet Sen, Roberto Carreño, Sijie Lu, Bradley W. McIntyre, Jeffrey J. Molldrem, Glen B. Legge, and Qing Ma. LFA-1 affinity regulation is necessary for the activation and proliferation of naive T cells. *Journal of Biological Chemistry*, 284(19):12645–12653, 2009.
  - [30] Quentin Verron, Elin Forslund, Ludwig Brandt, Mattias Leino, Thomas W. Frisk, Per E. Olofsson, and Björn Önfelt. NK cells integrate signals over large areas when building immune synapses but require local stimuli for degranulation. *Science Signaling*, 14(684), 2021.
  - [31] Daan Vorselen, Yifan Wang, Miguel M. de Jesus, Pavak K. Shah, Matthew J. Footer, Morgan Huse, Wei Cai, and Julie A. Theriot. Microparticle traction force microscopy reveals subcellular force exertion patterns in immune cell–target interactions. *Nature Communications*, 11(1), 2020.
  - [32] Aleksandra Wroblewska, Maxime Dhainaut, Benjamin Ben-Zvi, Samuel A. Rose, Eun Sook Park, El Ad David Amir, Anela Bektsevic, Alessia Baccarini, Miriam Merad, Adeeb H. Rahman, and Brian D. Brown. Protein Barcodes Enable High-Dimensional Single-Cell CRISPR Screens. *Cell*, 175(4):1141–1155.e16, 2018.
  - [33] Maxime Dhainaut. Perturb-map enables CRISPR genomics with spatial resolution and identifies regulators of tumor immune composition. 2021.
  - [34] Maria Tello-lafoz, Katja Srpan, Elisa E Sanchez, and Joan Massague. Cytotoxic lymphocytes target characteristic biophysical vulnerabilities in cancer. pages 1–18, 2021.